An Investigation on the Effect of Aluminum Particle Size on Detonation, Metal Acceleration, and Airblast

A DISSERTATION
SUBMITTED TO THE FACULTY OF THE
UNIVERSITY OF MINNESOTA
BY

Chad G. Rumchik

IN PARTIAL FULFILLMENT OF THE REQUIREMENTS
FOR THE DEGREE OF
DOCTOR OF PHILOSOPHY

Professor Paul J. Strykowski
Professor Joachim Heberlein (In Memoriam)

December 2015

Acknowledgements

I am grateful to my advisors, Professor Paul Strykowski and Professor Joachim Heberlein, for taking me on as a Ph.D. student and for the support and encouragement they have given me over the years. I would also like to thank Dr. Jim Kennedy for taking me under his wing and spending countless hours reviewing this work as well as serving on my examination committee. Thank you to Professors Terry Simon and Graham Candler for their help over the years and for serving on my examination committee as well.

Thank you to my other friends and colleagues who have helped and encouraged me over the years.

Dedication

This work is dedicated first and foremost to my parents for their support and encouragement through this whole process beginning when I was a little kid - I have told the story many times of my Mom getting Ficket and Davis' *Detonation Theory and Experiment* through inter-library loan when I was about 10 years old for me to attempt to read - well I made it to Dr. and I now understand that work, most of it anyway.

I suspect I inherited skills from my grandfathers - one a machinist and the other a chemistry professor - John Rumchik and Aubrey Wood.

And this work is dedicated to Cleo and Katie for their never ending and unquestioning support through it all.

Contents

List of Tables

List of Figures

List of Terms and Acronyms

ρ_0	The initial density.
ρ_{CJ}	The density at the CJ point.
$\sqrt{2E}$	Gurney velocity.
D	The steady state detonation velocity.
E or E_G	Gurney energy.
P_{CJ}	The CJ pressure.
u_0	The initial particle velocity - zero if the explosive is at rest before detonation.
u_{CJ}	The particle velocity at the CJ point.
v	The specific volume - $1/\rho$.
Al-HPE	Aluminized Hot Pressed Explosive.
Cast-cure	A binder system that makes use of a resin, such as HTPB, that chemically cures/crosslinks and hardens after mixing and casting.
CJ point	The sonic plane is the rear border of the reaction zone. Mathematically the CJ point is where the Rayleigh line is tangential to the product Hugoniot.
CR series	A composite high explosive based on RDX with an HTPB binder system that is pressed then cured.
Cylex	Cylinder expansion test - a copper tube is filled with the explosive to be tested and the wall velocity is measured during expansion and is used to compute the Gurney velocity.
H-5	A spherical aluminum powder approximately 5 µm in diameter.
HMX	Cyclotetramethylene Tetranitramine - a high explosive molecule.
MDX-81	A spherical aluminum powder with a diameter of approximately 30 µm.
Melt-cast	A system that makes use of a meltable binder such as TNT that hardens when cooled back to room temperature.
PBX	Plastic Bonded Explosive.

PBXN-109	Plastic Bonded Explosive utilizing HTPB as the binder and containing MDX-81 aluminum.
PBXN-109n	Plastic Bonded Explosive utilizing HTBP as the binder and containing nano scale aluminum - based off PBXN-109.
PETN	Pentaeythritol Tetranitrate - a high explosive molecule.
RDX	cyclo-1,3,5-trimethylene-2,4,6-trinitramine - a high explosive molecule.
TNT	2,4,6-trinitrotoluene - a high explosive molecule.
Tritonal	TNT containing aluminum powder.

1 Introduction

The purpose of this study is to examine how aluminum powder particle size impacts the detonation velocity, metal accelerating ability, and airblast pressure of small scale, pressed RDX based charges. New techniques were developed to measure metal acceleration and blast fireball temperature, and were published in the course of this work, to allow the capture of the data necessary to explore the behavior as a function of the aluminum particle size. Sub-micron aluminum powder, also termed Ultra-fine-grain (UFG), or "nano", has the potential to alter the detonation and/or blast performance of solid high explosives due to the increase in combustion efficiency, and hence, energy coupling it *may* provide. The possibility of prompt release and coupling of that energy in the detonation wave is increased by the very large surface area of the nanometer-scale aluminum powder resulting in enhanced rates of combustion compared to standard micrometer-scale powders as shown in Figure 1 [1–5]. However, thorough and comprehensive experimental data on the effect of aluminum particle size on a detonation have been quite lacking.

There has been research on pyrotechnic formulations for primer replacements such as aluminum/metal-oxide systems that do not burn promptly enough when micrometer-scale materials are used [6]. There has also been work on gun and rocket propellants that have shown substantial improvements in combustion efficiency and impulse when using Alex[1] aluminum with the aluminum particle size being predominately 50 nm - 200 nm [7–10], but the majority of the experiments conducted with high explosives have been a single-shot or a duplicate examining a particular formulation and one aspect of performance or behavior such as critical diameter or blast. Australia's Defence Science and Technology Organization (DSTO) and De-

[1]Alex aluminum is made by the exploding wire method, and the technique produces a very broad particle size distribution - Alex was one of the first nanoscale aluminum powders commercially available.

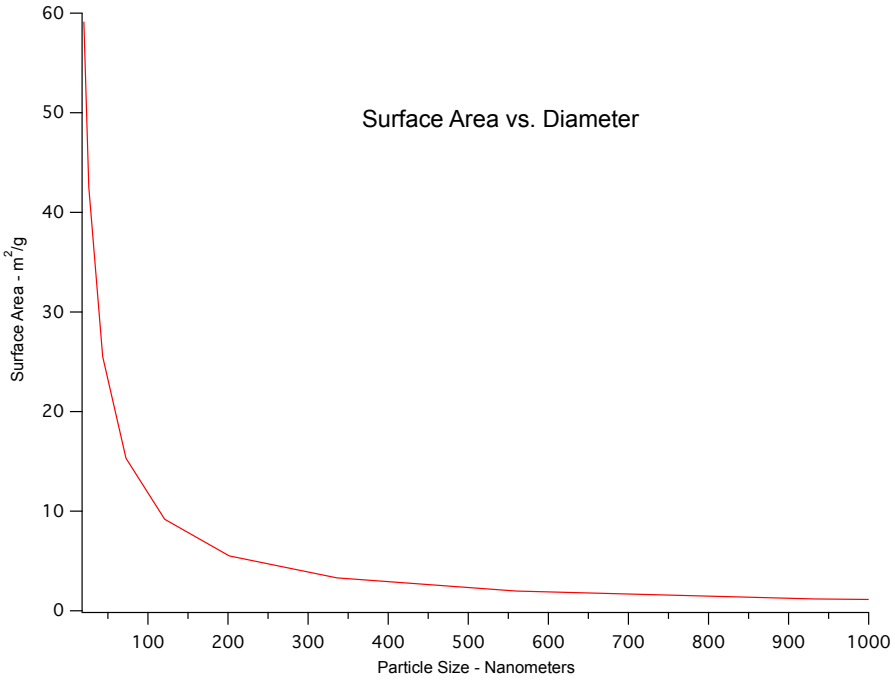

Figure 1: The effect of particle diameter on surface area given uniform spherical particles.

fence Research & Development Canada - Valcartier have performed more in-depth studies with high explosives and have observed a decrease in the critical diameter of Tritonal when formulated with Alex aluminum [11, 12]. The reduction in critical diameter means Tritonal formulated with nanometer-scale aluminum will propagate a detonation in a charge with a smaller diameter than in the case of standard Tritonal formulated with micrometer-scale aluminum powder, and this implies that the detonation reaction zone is shorter. Early modeling work also suggests nanometer-scale aluminum can potentially increase the acoustic energy[2] in the reaction zone leading to an increase in detonation energy [13, 14].

Further methodical research was deemed necessary to determine what affect aluminum grain size has on the performance of high explosives. This work focuses on

[2]Acoustic energy is the energy available to drive the detonation shock wave in the explosive, thus the energy that is released ahead of the sonic plane in the detonation reaction zone.

a series of RDX-based formulations pressed to a high density with various particle sizes of aluminum powder. RDX was chosen as it is a readily available explosive compound that lends itself well to formulation as it is not overly sensitive to impact and friction. Pressing allows more control over the density than cast-cure or melt-cast systems and greater ease in formulation adjustments such as particle-size variation.

The tests were performed in replicate with charges of sufficient quality to enable us to obtain repeatable results. The main areas of interest in this work are the effects on airblast performance [15–17] and Gurney energy (metal acceleration) compared to standard aluminized formulations. This work also examined the effect of inert particle loading and partial inert particle loading to determine the impact the aluminum oxide content of various aluminum powders has on explosive performance. Note that in this work, the term "nanometer-scale" shall mean 50 nm - 100 nm and "micrometer-scale" shall mean all larger powders with the smallest in the group being approximately 5 µm.

2 Background on Explosives and Performance Tests

Explosives are divided into two major categories: Low Explosives and High Explosives [18, 19]. Low explosives function by deflagration - rapid combustion - and produce a pressure wave with a measurable rise time. High explosives function by detonation and produce a chemically supported shock wave which has a step change in the pressure at the shock front. Conceptually one can think of low explosives providing a push to their surroundings and high explosives providing a slap followed by a push. Figure 2 shows qualitative pressure traces of a detonation and of a deflagration. Note the peak pressure of the deflagration is much much lower than that of the detonation and the time the pressure takes to reach its peak is also greater than for the detonation.

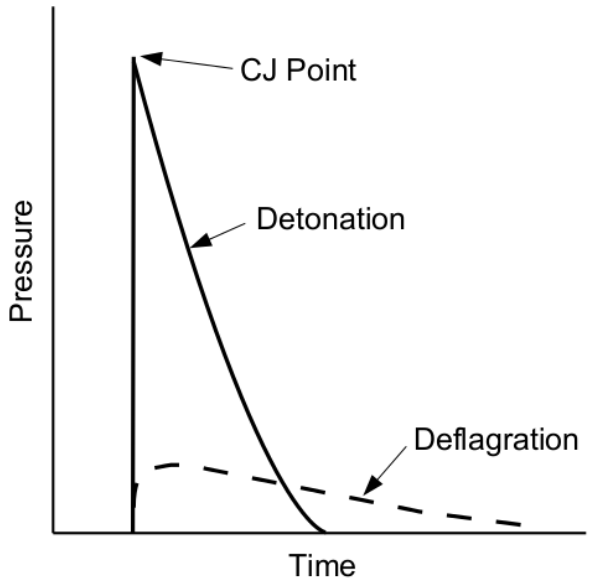

Figure 2: The expansion-wave behavior of detonation vs. deflagration. The detonation reaction zone is not shown in this figure because it is much shorter than the product gas expansion waves for both the detonation and deflagration cases depicted.

Detonations in condensed matter - solids and liquids - obey the same jump conditions that describe detonations in gases [20–23]. Figure 3 shows the control volume

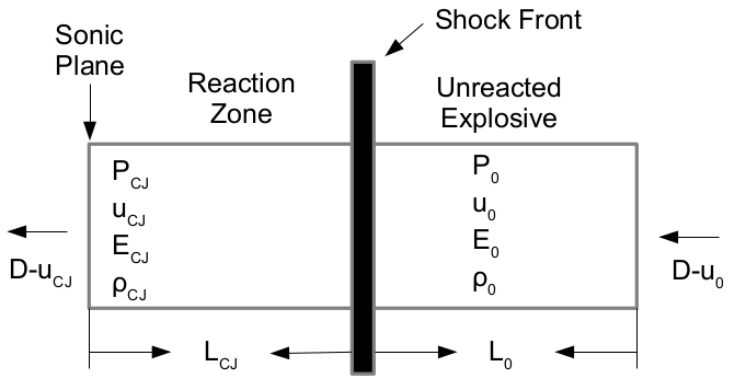

Figure 3: Control volume in 1-D detonation modeled after Cooper. The frame of reference is that the detonation front is taken to be stationary.

used for a plane 1-D flow system, where ρ_0 and ρ_{CJ} are, respectively, the initial density of the explosive and the density of the gas at the CJ point; v_0 and v_{CJ} are the equivalent specific volumes; u_{CJ} is the particle velocity at the CJ point; D is the detonation velocity; P_{CJ} is the CJ pressure; and E_0 and E_{CJ} are the specific internal energies at the initial and CJ states. The standard conservation requirements apply; that is mass, momentum, and energy must be conserved.[3] Let the area be represented by A and the mass by m. The volume is the product of A and the length L. The mass is then found to be $m = \rho AL$, and since $L = t(D - u)$, we can now write the mass balance as Equation 1 for the case of the explosive being at rest, $u_0 = 0$.

$$\frac{\rho_{CJ}}{\rho_0} = \frac{D}{D - u_{CJ}} \tag{1}$$

To develop the momentum balance we make use of the fact that force is equal to the time rate of change of momentum and that the momentum is mu. The force, F, can be written as $F = (P_{CJ} - P_0)A$. We can then write $(P_{CJ} - P_0) = \rho_{CJ}u_{CJ}(D - u_{CJ}) - \rho_0 u_0(D - u_0)$. After simplifying with the mass equation and letting $u_0 = 0$,

[3]These equations apply only for a supported shock as found, for example, in a flyer plate impact, or an infinitesimal distance from the shock front in a detonation - in an unsupported shock, such as detonations, an equation of state (EOS) must be experimentally determined to describe the state after the passage of the shock wave.

we get Equation 2.

$$P_{CJ} - P_0 = \rho_0 u_{CJ} D \tag{2}$$

The rate at which the energy changes in the control volume is equal to the rate at which work is done on or by the control volume. The rate at which work is done can be expressed as $\frac{\triangle W}{\triangle t} = P_{CJ} A u_{CJ} - P_0 A u_0$. The changes in energy are due to a change in internal energy as well as the change in kinetic energy. We can write the change in internal energy as $\frac{\triangle E}{\triangle t} = (\rho_{CJ} A L_{CJ} e_{CJ} - \rho_0 A L_0 e_0)/t$ and the change in kinetic energy as $\frac{\triangle KE}{\triangle t} = \left(\frac{1}{2}\rho_{CJ} A L_{CJ} u_{CJ}^2 - \rho_0 A L_0 u_0^2\right)/t$. Now $\frac{\triangle W}{\triangle t} = \frac{\triangle E}{\triangle t} + \frac{\triangle KE}{\triangle t}$ which simplifies to Equation 3 where specific volume $v = 1/\rho$ and $u_0 = 0$.

$$E_{CJ} - E_0 = \frac{1}{2}\left(P_{CJ} + P_0\right)\left(v_0 - v_{CJ}\right) \tag{3}$$

A typical pressure-specific volume plot for Chapman-Jouget model of detonation is shown in Figure 4 [20, 22, 24–27]. In a CJ detonation, the chemical reaction and subsequent heat release are instantaneous, resulting in a reaction zone of zero thickness. In real explosives, the reaction zone thickness is on the order of a few microns for what are known as ideal explosives, like pure RDX that was used in this study.

The Hugoniot is simply a material-dependent empirical relation which describes the locus of the shock states of the material in a plane such as $P - v$ as used in Figure 4 [22, 28]. As with gaseous detonations, the Rayleigh line is a mathematical construct that connects the initial state (P_0, v_0) to the jump state on the unreacted Hugoniot. The point of tangency of the Rayleigh line to the detonation product Hugoniot is the Chapman-Jouget (CJ) point.

The shape and position of the reacted products Hugoniot is dependent upon the energy and properties of the chemical species in the reaction zone. For most organic explosives, the reaction zone contains water, carbon dioxide, carbon monoxide, ni-

trogen, and soot (carbon). If aluminum is present in the undetonated explosive, and reacts in the reaction zone, aluminum oxide will also be present in the reaction zone. In the case of a more energetic reaction, such as aluminum combustion, the product Hugoniot will shift upwards and to the right in the $P - v$ plane. This shift will increase the slope of the Rayleigh line which means a higher velocity of detonation, D.

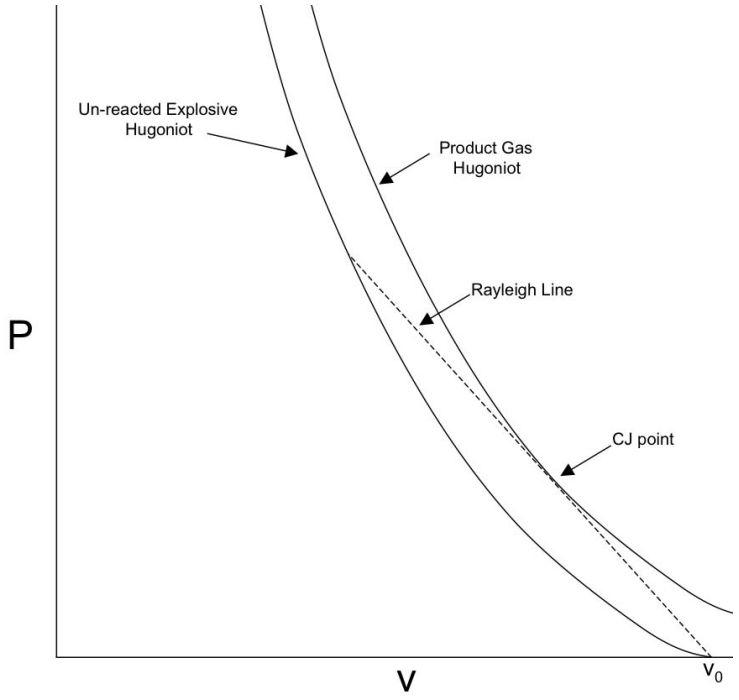

Figure 4: The detonation jump condition in the $P - v$ (pressure specific-volume) plane.

It is intuitive to think about the detonation as occurring in three phases. The first is the undetonated explosive; the second is the reaction zone, and the third is the afterburn or expansion zone as shown in Figure 5. The leading edge of the reaction zone is the shock front, which we call the Von Neumann spike, and this is the highest pressure that occurs during the detonation process. Following the Von Neumann spike is the area of chemical reaction which is bounded at the rear by the

sonic plane. In the case of a Chapman-Jouguet (CJ) detonation, the CJ plane is the sonic plane. Any release of chemical energy after the sonic plane will not couple energy to the reaction zone nor will it influence the detonation velocity, just as a man traveling at sonic speed or greater will not hear someone yell behind him [29].

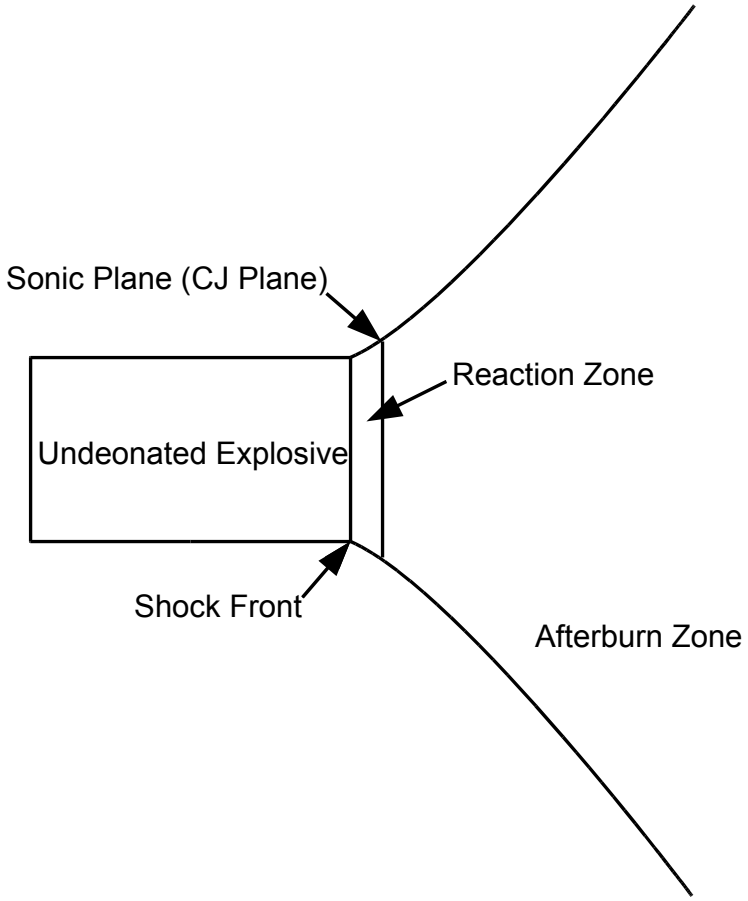

Figure 5: Detonation schematic.

Explosive performance behavior can be broken down into three distinct time regimes, and each has distinct chemical and dynamic characteristics associated with it. The first is the "early time" which occurs on the order of 0.1 µs and affects the detonation velocity of the explosive. This regime affects the detonation pressure of the explosive and is responsible for the explosive's brisance (i.e. its shattering

power). The second is the "mid-time" gas expansion occurring on the 0.1 µs to 10 µs timescale[4] and predominately impacts the metal-accelerating ability of the explosive; this is described by the Gurney energy. The third regime is late-time release, which occurs well after the reaction zone and adds energy to the airblast usually due to combustion of material, such as aluminum, with the detonation products and the surrounding air. The duration will vary from a few hundred microseconds for the small charges in this study to many milliseconds for very large and/or heavily confined charges. As such, late-time energy release will also increase the heaving ability of an explosive. Heaving is the explosive's ability to move heavy material such as a large rock mass encountered in commercial rock blasting.

The focus of this research is on the effects aluminum powder particle size has on the performance of detonating high explosives as a result of the particle surface area and the resultant energy release rates of the aluminum combustion. An understanding of the various time scales involved in a detonation is crucial. While low explosive propellants, such as solid rockets, generally have reactions zones tens of milliseconds in duration, a high explosive's reaction zone is on the order of 0.1 µs [29–31]. If aluminum is to contribute energy to the detonation wavefront, the aluminum must react to a substantial degree within ≈ 0.1 µs time frame after being hit (heated) by the shock front. The various micrometer-scale aluminum powders currently used in explosives do not react quickly enough after being hit by the leading shock wave to contribute energy to the reaction zone and boost the detonation velocity [32]. In fact the aluminum acts as a heat sink and has been shown to lower the detonation velocity in comparison with neat formulation values [33].[5]

Due to the very slow reaction of micrometer-scale aluminum powders, such powders are commonly used in explosives used for rock blasting as time for the rock mass

[4]For the case of our small scale experiments, longer times will apply for larger charges.

[5]"Neat formulation" shall mean a formulation containing no aluminum or talc.

to move is several milliseconds [23]. The aluminum is therefore able to burn in the afterburn zone, add heat to the detonation product gases so as to sustain the gas pressure longer, and increase the amount of Pdv work the gases can perform on their surroundings - the rock mass in this example.

2.1 Detonation Rate and Pressure

The detonation pressure determines how brisant an explosive will be to materials in contact or very close proximity to it. For the purposes of cutting or throwing metal, one desires a very high detonation pressure. Using the conservation of momentum equation from above (Equation 2) and the relation of shock velocity to particle velocity in a gas shown in Equation 4, the CJ pressure can be found with Equation 5. Since γ is approximately 3 at the CJ point [18], the CJ pressure, P_{CJ}, can be estimated by Equation 6.

$$u_{CJ} = \frac{D}{\gamma + 1} \tag{4}$$

$$P_{CJ} = \frac{\rho_0 D^2}{\gamma + 1} \tag{5}$$

$$P_{CJ} = \frac{\rho_0 D^2}{4} \tag{6}$$

The density, ρ_0, is limited by the density of the components in the formulation. It is not possible to increase the density of an RDX (a common unimolecular explosive used in military and commercial formulations) or other existing explosive crystal itself. Nor is it possible to increase the crystal density of aluminum or the other additives in an explosive formulation. Therefore, without developing new explosive compounds with higher crystal densities, the only way to increase the detonation pressure is to increase the detonation velocity. The velocity varies for neat explosives such as RDX, HMX, TNT, etc. according to their energy content, molecular

structure, chemical kinetics, the amount of gas generated, and their initial density, ρ_0.

It is important to point out that the heat of combustion for molecular explosives is on the order of 4-6 kJ/g and aluminum is 16.26 kJ/g [18]. The nanometer-scale aluminum has the same crystal density as micrometer-scale aluminum. While aluminum is more dense than RDX (or other explosives), aluminum only serves as a fuel and cannot react and release energy without an oxidizer. The aluminum therefore must be able to scavenge oxygen contained in the explosive formulation, such as that in the explosive molecule itself or that which is provided by a separate oxidizer such as ammonium perchlorate or ammonium nitrate. Alternatively, the aluminum can react with oxygen in the air in the afterburn regime. The steady state detonation rate therefore is the result of an energy balance between the release of chemical energy in the reaction zone, the dynamics of oxygen scavenging, and the energy required to drive the shock front through the explosive.

If, due to the greatly increased surface area, nanometer-scale aluminum alters the net energy and amount of gas released into the reaction zone, it will alter the detonation velocity, and thus, the detonation pressure and the brisance of the explosive. Indeed, theoretical modeling work by Gonthier [13, 14, 29, 33] suggests nanometer-scale aluminum on the order of 100 nm has the potential to show an increase in detonation velocity over micrometer-scale aluminum. The steady detonation velocity, therefore, might serve as an indirect probe of the aluminum dynamics in the reaction zone. Detonation velocities of all of the formulations used for this study were measured with an experiment known as a rate stick. In addition to being able to estimate the detonation pressure with Eq. 6, the rate of detonation was also needed to allow synchronization of dynamic diagnostics in further experiments.

2.2 Gurney Energy

The Gurney energy is a measure of the energy available to drive a solid in contact with the explosive and was derived by Gurney circa 1940 [34, 35]. The expanding gases from the detonation are assumed to have a linear velocity profile with the radial velocity being zero at the axis and maximum at the gas/metal interface. The density of the gas is also assumed to be constant as a function of radial position at any given time.

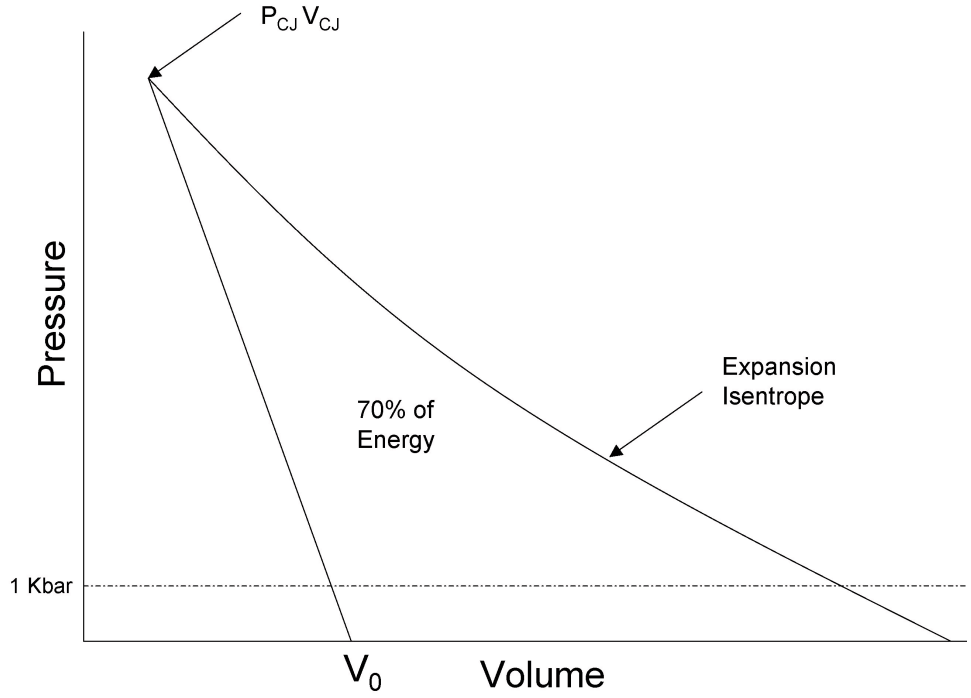

Figure 6: The Fickett-Jacobs cycle.

If one considers the Fickett-Jacobs cycle for the detonation shown in Figure 6, it is apparent that the majority of the expansion work is delivered as the expansion isentrope drops from a typical CJ value of 200-300 kbar to a pressure of one killobar [20]. Due to acoustic decoupling or fracture of the metal walls, not all of the chemical energy in the explosive imparts kinetic energy to the gas and metal wall. Thus

an effective specific energy E_g, called the Gurney energy, is used to quantify the energy available to perform work on the metal wall. The total kinetic energy E_k is partitioned between the kinetic energy of the gas $E_{k(gas)}$ and the kinetic energy of the metal wall $E_{k(metal)}$. Thus $CE_g = E_{k(metal)} + E_{k(gas)}$ where C is the mass of the explosive. Gurney assumed that the acceleration of the gas and the metal wall was instantaneous, so the initial configuration of the system could be used in performance calculations. In addition, the velocity profile is assumed to be linear and vary only with the distance from the center with $V = 0$ at $r = 0$ yielding the expression for gas velocity as rV/r_e. The derivation shown below is for a cylindrical tube (cylinder) loaded with an explosive as shown in Figure 7 where M is the metal mass, and ρ_0 is the initial density of the undetonated explosive. [23, 34].

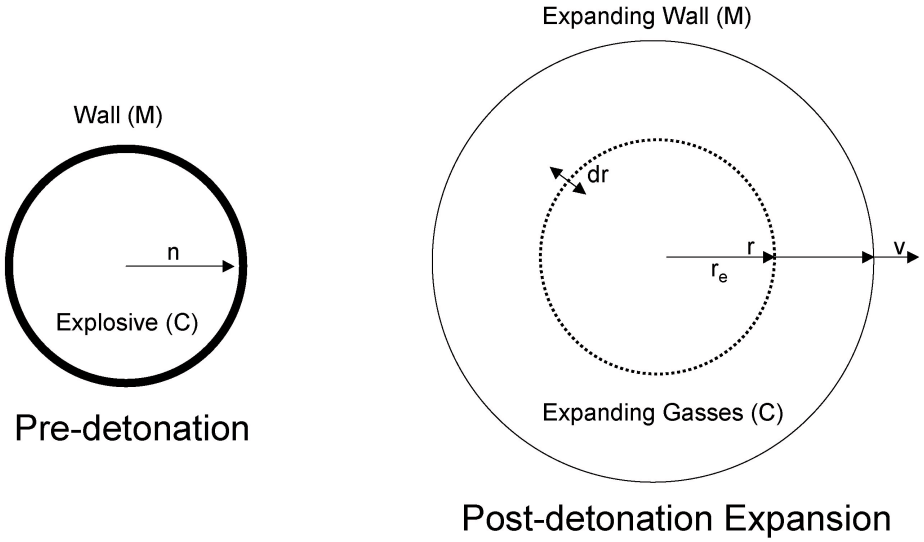

Figure 7: Cylinder loaded with explosive.

The kinetic energy of the detonation is now balanced in Equation 8 and integrated over the volume to yield Equation 9.

$$\rho_0 = \frac{C}{\pi r_e^2} \tag{7}$$

$$CE_g = \frac{1}{2}MV^2 + \frac{1}{2}\int_0^{r_e}\left(\frac{rV}{r_e}\right)^2 \frac{C}{\pi r_e^2} 2\pi r dr \tag{8}$$

$$= \frac{1}{2}MV^2 + \frac{1}{4}CV^2 \tag{9}$$

The values of Gurney energy are usually tabulated as the Gurney velocity $\sqrt{2E_g}$ which gives the standard form of Equation 10 below.

$$\frac{V}{\sqrt{2E_g}} = \left(\frac{M}{C} + \frac{1}{2}\right)^{-1/2} \tag{10}$$

The Gurney energy has traditionally been measured with a cylinder expansion test, commonly referred to as a cylex test. Details of the standard cylex tests and other tests to measure the Gurney energy are described in Section 6 of this paper. This work employed miniaturized tests to allow more tests to be fired and to reduce cost and damage to the test facility.

The Gurney energy was measured for the main formulations used for this test series and baselined with a non-metalized RDX-based formulation. Since the baseline was established, the performance of formulations employing micrometer-scale aluminum powder and those employing nanometer-scale aluminum powder could be compared. In addition, a formulation in which inert talc has been substituted for the aluminum was tested to determine the effect of RDX mass dilution on the Gurney energy.

It is known that micrometer-scale aluminum powder *decreases* the explosive's metal accelerating ability as the aluminum does not combust with sufficient promptness to add energy in the critical time period - up to 10 µs or so after the passage of the shock wave [32].[6] If the nanometer-scale aluminum powder can react in less than 10 µs and provide a net increase in the energy of the expanding gases, the Pdv work can be increased leading to an increased value of Gurney velocity. Another

[6]for the 1/2 inch diameter tests used for this work

important point to emphasize is that the aluminum is heated by the passing of the shock wave. This process is endothermic due to the sensible heat and latent heats of melting and vaporization of aluminum. For the aluminum to increase the Pdv work on the metal tube, the prompt combustion fraction, the fraction of the aluminum that combusts in under 10 µs, must also be sufficient to overcome the above losses. Work by Gonthier [13] suggests the break-even point for the detonation velocity is approximately 20%-25% of the aluminum in the formulation that must undergo prompt combustion depending on the grain size of the aluminum powder.

The calculation is not as simple as it first appears as both solid-phase and gas-phase reactions can occur, changing the losses due to latent heats of melting and vaporization. Gonthier's modeling effort also suggests that it is possible to see an increase in the detonation velocity when using nanometer-scale aluminum vs. micrometer-scale sized aluminum. As the metal acceleration occurs on a longer time scale than the detonation reaction zone, it is reasonable to expect to see a difference between nanometer-scale aluminum and micrometer-scale aluminum when comparing the Gurney energies of a formulation with a given composition.

2.3 Airblast

The airblast from an explosion is considered to be a late-time event. Airblast energy, and the "bubble energy" associated with underwater explosions, are often enhanced by adding aluminum powder to the formulation [12, 18, 22, 23]. An example of this is the explosive Tritonal, which is simply aluminized TNT (by mass 70% TNT/30% Al or 80% TNT/20% Al), and is a common fill for general purpose bombs used by the US military. The aluminum releases its energy in the afterburn zone and the gases expand rapidly as shown in Figure 5. The energy released by the aluminum in the afterburn zone is not acoustically coupled to the shock front to help drive the

detonation, as the energy is released behind the sonic plane [24, 29, 36, 37].

The reaction dynamics of the airblast can be measured in the free field (which would truly be a charge well above ground to avoid any surface reflections) or in enclosed environments by using high speed pressure gauges. The key to a free-field measurement is placing the gauges in such a way that the shock wave arrives at the gauge before it is influenced by any surface or confinement [38–41]. The airblast experiments for this work were conduced in a quonset (half-cylindrical) test chamber 22 feet x 30 feet x 14 feet in height. The charges are small in relation to the chamber and were suspended above the floor, away from all other surfaces in the chamber. Therefore, the measurements taken between the charge and the walls are considered to be free field as the shock wave hits the gauge before being altered by the constraints of the chamber [36].

3 Initial Modeling of Aluminum Combustion Potential

The objective of this modeling effort is to bound the ignition delay, τ, of the aluminum particles as a function of particle diameter. The ignition delay is a critical parameter, as the aluminum must ignite and become exothermic with sufficient promptness if it is to contribute energy to the detonation event or to the expanding fireball. The three time regimes of interest concerning output from the detonation event considered for this work are detonation velocity ($\tau < 0.1$µs), Gurney velocity ($\tau < 10$µs), and airblast ($\tau < 3$ ms).

3.1 The System

An idealized simple system is used for the model where the aluminum particles are assumed to be perfectly spherical and the shock is planar and one-dimensional. To keep the problem tractable, a dilute limit will also be assumed, meaning the aluminum particles do not interact with one another nor do the aluminum particles change the temperature of the gas, as the mass of the surrounding gas is much much greater than that of the aluminum particles. Thus, the model consists of a single aluminum particle in an infinite gas bath as shown in Figure 8.

For combustion of the aluminum particle to take place, oxygen (pure or displaced from H_2O, CO or CO_2) must reach the aluminum after the aluminum is heated sufficiently by a combination of the passing shock wave (adiabatic compression) and the surrounding hot gases. In addition, the passivating oxide layer on the surface of each aluminum particle must be broken or melted to expose nascent aluminum. While research has been conducted on the failure/fracture of the aluminum-oxide layer on aluminum particles, it has been for the cases of low-pressure combustion/deflagration and does not cover the pressures encountered in a solid phase detonation [42–45].

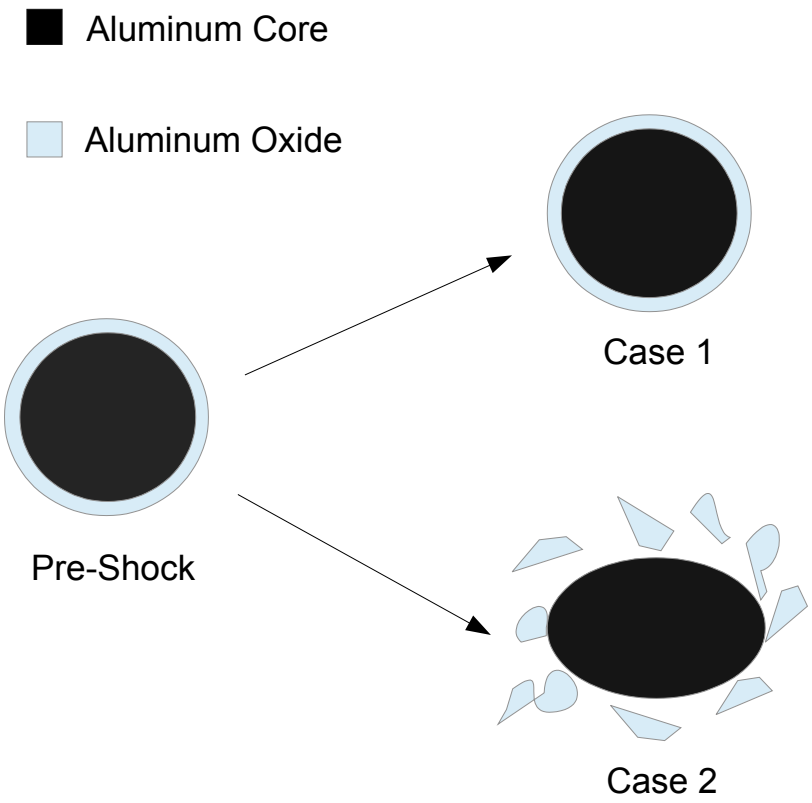

Figure 8: An aluminum particle in a gas bath pre and post-shock. Case 1: the particle has an intact oxide layer, and case 2: the oxide layer has been shattered by the passing shock wave.

For this work, the RDX-based formulation containing 20% aluminum powder has an estimated CJ state of $P = 22.6$ GPa, $\rho = 2.26$g/cc, $T = 3000$ K, $D = 7.49$ mm/µs, and $u = 1.74$ mm/µs, where D is the shock wave velocity (detonation wave velocity), and u is the particle velocity behind the shock.

With the above parameters assumed, the relation for an estimated reactive Hugoniot given in Cooper [22] is used to generate Equation 11 for the $P - u$ Hugoniot.

$$P_{CR} = 54.5 - 22.5u + 2.38u^2 \tag{11}$$

The $P-u$ Hugoniot of aluminum is also given in Cooper for aluminum as Equation 12.

$$P_{Al} = 14.84u + 3.73u^2 \tag{12}$$

At the interface of the reacting explosive and the aluminum, the pressures must be equal, thus $P_{CR} = P_{Al}$. The resulting equation is solved to find $u = 1.39$ mm/µs and $P = 27.8$GPa. The aluminum oxide passivation layer on an aluminum particle is quite thin, $\approx$ 2-5 nm, so it is not considered in this calculation.

The ultimate strength for the aluminum oxide is approximately 2.9 GPa. Thus, it is improbable the oxide layer will survive the shock passage intact as the pressure is not applied to the particle isostatically and exceeds the ultimate strength by an order of magnitude. As case 2 is expected, the model will focus on the heating and ignition of the aluminum particle and assume that the aluminum surface is exposed to oxidizer.

3.2 Heating of the Particle

Passage of the shock will heat the aluminum by adiabatic compression and the change in the specific volume, ν, can be found using Equation 13 [22]

$$P = \frac{C_0^2 (\nu_0 - \nu)}{[\nu_0 - S(\nu_0 - \nu)]^2}, \tag{13}$$

where $U = C_0 + Su$. Equation 14 can then be used to determine the change in internal energy of the aluminum particle as a result of the shock compression,

$$\triangle E = \frac{1}{2} P (\nu_0 - \nu) \tag{14}$$

and the temperature jump can then be calculated using Equation 15

$$\triangle T = \frac{\triangle E}{C_v}. \tag{15}$$

One finds the temperature jump to be 1077 K for the explosive described above. The aluminum will cool as the pressure is released after the CJ state if it does not begin to burn. Cooper states that incipient melting of aluminum will occur with shocks

of 60 GPa. Given that this system is below that value by a factor of two, it will be assumed that phase change does not occur in the initial shock heating.

After passage of the shock, convection will continue to heat the particle. Equation 16 is the 1D governing transient heat transfer equation in spherical coordinates, with temperature treated as a function of radius and time.

$$\frac{\partial T}{\partial t} = \alpha \left[\frac{\partial^2 T}{\partial r^2} + \frac{2}{r} \frac{\partial T}{\partial r} \right] \tag{16}$$

As the aluminum will generate heat upon combustion, Equation 16 becomes Equation 17,

$$\frac{\partial T}{\partial t} = \alpha \left[\frac{\partial^2 T}{\partial r^2} + \frac{2}{r} \frac{\partial T}{\partial r} \right] + q \frac{\partial \lambda}{\partial t} \tag{17}$$

where q is the heat of combustion of aluminum, and λ is the extent of the reaction(mass fraction of aluminum which has burned). The extent of reaction is based on an Arrhenius rate law given by Equation 18

$$\frac{\partial \lambda}{\partial t} = k \left(1 - \lambda\right) e^{\frac{-E}{RT}} \tag{18}$$

where k is the exponential pre-factor, and E is the activation energy. The value of the convective heat transfer coefficient, h, is given by Equation 19

$$h = Nu_D \frac{k}{D} \tag{19}$$

where D is the particle diameter, k is the thermal conductivity of the aluminum, and Nu_D is the dimensionless Nusselt number, which is taken as 2 in the limit of a small particle [46].

3.3 Numerical Solution

To determine τ, Equations 17 and 18 were discretized to give a form that could be solved numerically. Central differencing was used resulting in Equations 20 and 21,

$$\frac{\partial T_i}{\partial t} = \alpha \left[\frac{T_{i+1} - 2T_i + T_{i-1}}{\triangle r^2} + \frac{2}{r_i} \left[\frac{T_{i+1} - T_{i-1}}{2 \triangle r} \right] \right] + q \frac{\partial \lambda_i}{\partial t}, \tag{20}$$

$$\frac{\partial \lambda_i}{\partial t} = k\,(1-\lambda_i)\,e^{\frac{-E}{RT_i}}. \tag{21}$$

To evaluate this system of equations, an explicit code was written in Fortran 90 making use of DLSODE as the equation solver, as DLSODE will handle a stiff system [47]. The boundary condition at the interface with the gas was convective with $Flux = h(T_{gas} - T_{surface})$. The value of T_{gas} was specified as either a constant value or as a function that varied with time. The value of $T_{surface}$ was set to an initial value of 1,350 K based on the results from the shock heating calculation. A constant mesh spacing was used with a reflected boundary condition at the center, $Flux = 0$. It was found that 200 spatial nodes were adequate based on the verification with an analytical solution. The analytical solution was in the form of an infinite series obtained with the separation of variables technique as described in Kakaç [48] for a 1D sphere having a constant value of h. The verification is shown for multiple times as a function of radial position in Figure 9.

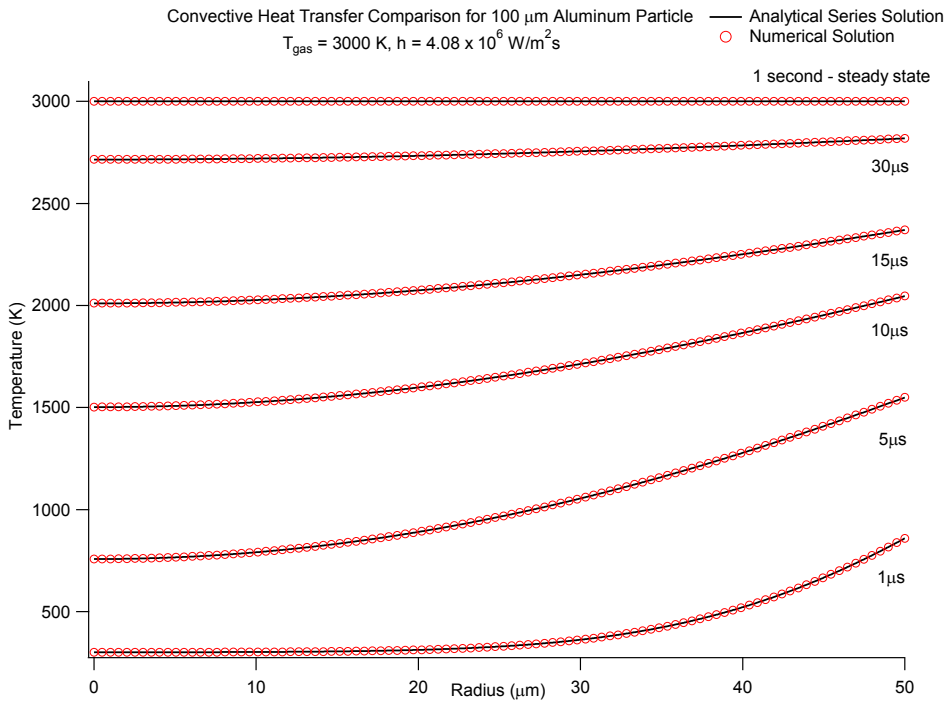

Figure 9: Verification of the numerical solution with established analytical solution. Note neither the analytical solution nor this model account for phase change of the particle; therefore, the aluminum does not melt.

To determine τ, the flux was monitored and the code stopped when the flux was exothermic. To make certain that the sign change in the flux was not due to numerical oscillations, the code was run for each case with the value of q set to 0 which will not allow the flux to become exothermic. The flux stop criterion was then set such that the code would not exit until the flux was indeed physically exothermic due to combustion. The results are shown in Figure 10 as a function of particle diameter with three different conditions for T_{gas} and two different conditions of k and E.

The values for k and E were taken from Park [49]. As there is variability in the parameters, limiting cases were run for each of the T_{gas} conditions. Two constant condition probing cases were run for T_{gas}, 3000 K and 3500 K, as well as a more realistic variable temperature case where $T_{gas} = -153t + 3500$ for $0 \leqslant t \leqslant 15\mu s$ and

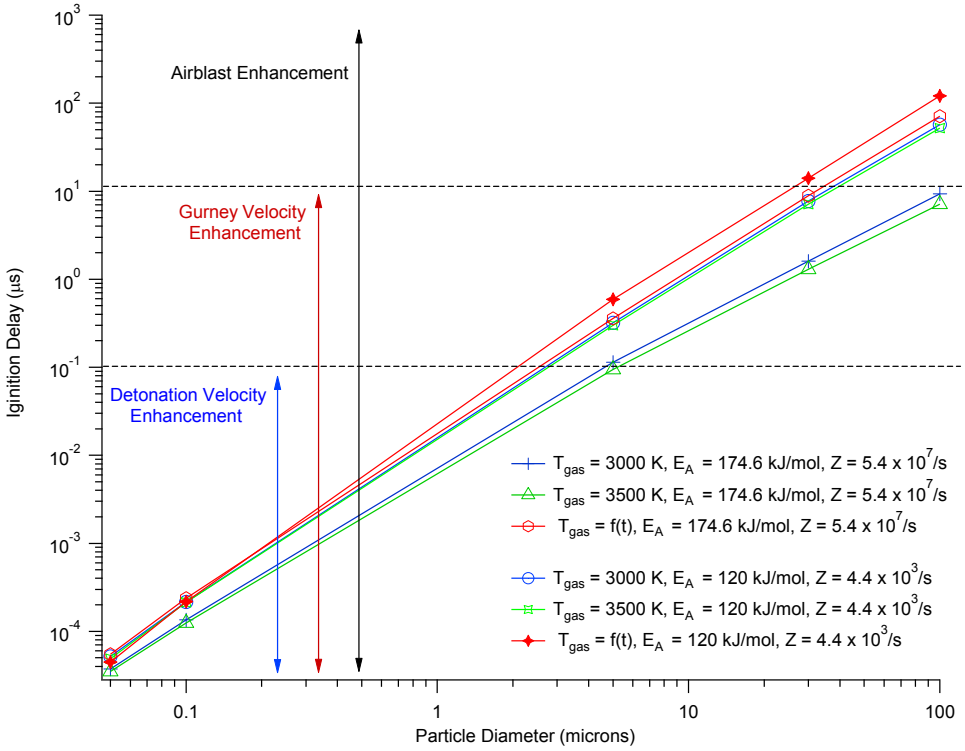

Figure 10: The ignition delay, τ, as a function of particle diameter and boundary conditions.

$T_{gas} = 1200$ K for $t \geqslant 15$µs. The fit for the variable temperature was based on data from a CTH hydrocode[7] simulation of a cylinder expansion test.

The variations in temperature and fit parameters do affect the slope of the ignition delay line, but not enough to change the regimes in which the particles can react in the detonation event, except for the 3500 K case, as 3500 K represents an unrealistically high later time temperature. The 50 nm and 100 nm particles can become exothermic with sufficient promptness to increase the detonation velocity. The 5 µm particles are able to become exothermic in the sub-10 µs time band to enhance metal acceleration with the 30 µm particles being right on the border with a τ value of 9-13 µs. The 100 µm particles are relegated to being exothermic after 10 µs as the varying T_{gas} case is the most realistic environment. Therefore, they will contribute only to airblast.

[7]CTH is a commonly used hydrocode to simulate explosive systems.

This simplified analysis shows the heat transfer and kinetics of ignition are not the rate limiting steps for the participation of small diameter aluminum particles becoming exothermic and thereby increasing detonation velocity, metal acceleration, and airblast. This simple model does not take into account the diffusion limitations which will be present in a real system, as such a model is well beyond the scope of this effort.

4 Development of the Formulations

PBXN-109n was one of the first nanometer-scale, aluminum-containing explosives formulated at the Air Force Research Laboratory, Energetic Materials Branch. It was intended to serve as a test explosive to evaluate the potential performance and safety enhancements offered by adding nanometer-scale aluminum to conventional explosive formulations.

PBXN-109n is based on PBXN-109 with all the mass percentages held to the original PBXN-109 formulation. The MDX-81 aluminum which has a mean particle size of $\approx$ 30 µm, however, was replaced in whole or in part with nanometer-scale aluminum.

Alex aluminum, produced by the exploding-wire method and having a size range of 100-200 nm, has been the most prevalent nanometer-scale aluminum used in both explosives and propellants. It was decided that the PBXN-109n study would begin by utilizing nanometer-scale aluminums from Technanogy, specifically their material with an advertised mean particle size of 100 nm. The Technanogy product is produced by a different method which yields a tighter particle-size distribution. The size was chosen as it was felt it would be small enough to produce an observable difference when compared to MDX-81 micrometer-scale aluminum, yet large enough to not be spontaneously reactive with air when handled outside of an inert atmosphere glove box.

Due to the extremely high surface area of $\approx$ 25 m^2/g of the nanometer-scale aluminum (compared to $\lesssim$ 1 m^2/g for MDX-81), it was impossible to mix and load PBXN-109n in the same way as its standard PBXN-109 counterpart. PBXN-109n had a viscosity that prevented loading charges by vacuum casting as would be done with a standard PBXN-109. The viscosity was beyond the range of any viscometer

available, and the consistency of PBXN-109n is best described as stiff cookie dough, which allowed the use of a Baker-Perkins type mixer to prepare samples.

A standard mix cycle for PBXN-109 was used while mixing samples of PBXN-109n in a one pint Baker-Perkins mixer. Vacuum of approximately 28" Hg was maintained during all cycles. The mix quality was considered to be good as the binder was evenly distributed over all particles when examined with a scanning electron microscope.

Even though a homogeneous mix was repeatedly obtained, "research quality charges" with consistent and uniform ρ_0 were never obtained. Several loading methods were explored including vacuum casting while tamping and vibrating. The mixture was simply too viscous to allow proper degassing during loading even though the explosive was mixed under vacuum. When loaded into a 1 inch x 6 inch mold the charge had a very "spongy" feel by all loading techniques tried. When the charge was incrementally loaded by placing golf ball size pieces of mixed explosive into the tube and carefully tamping each increment, radiography revealed very discrete interfaces and repetitive density bands throughout the charge. Producing a wet molding powder was also tried by pushing the uncured explosive through a 20-mesh sieve by hand. The radiographs revealed the same density banding due to tamping.

An attempt was also made to granulate the explosive with the sieve and allow it to cure in the granulated state. The explosive was then loaded into a die and pressed at room temperature at a pressure of 25,000 psi. As expected, the granules remained discrete, preventing the production of a usable pressing powder with this formulation.

A substantial amount of time was spent investigating the possibility of extrusion as a loading technique. It is believed extrusion would be successful if careful attention is paid to degassing and material interface control during the process. Due

to the expense and time required to obtain such equipment and certify it to process explosives, this effort was placed on hold in favor of a new formulation that alleviates the viscosity problem induced by the nanometer-scale aluminum.

4.1 Initial Formulation - Al-HPE

In order to perform repeatable and reliable detonation experiments to determine the effect of the addition of nanometer-scale aluminum to an explosive, it was necessary to develop a formulation that overcame the viscosity problem induced by the high surface area of nanometer-scale aluminum. Since a pressing powder can be made with excess solvent during the mixing phase it was decided to pursue a pressed formulation.

Consistency, rather than absolute best performance, was also required at this phase of the study. While it is believed that fluoropolymer binders such as Viton and PVDF can serve as oxidizers for the aluminum, such polymers are soluble in polar solvents such as acetone and THF that are also solvents for the explosives of interest. Because of the difficulty presented by mutually soluble constituents, it was decided to use an inexpensive and readily available hydrocarbon binder, which was soluble in a nonpolar solvent such as hexane or octane. Elvax, produced by Dupont with a vinyl acetate content of approximately 30%, was chosen as the binder.

PBXN-202 was developed several years ago and is composed of 91% class I RDX[8] and 9% Elvax, which is a rubber-like polymer. Since it is already a fully qualified explosive, and can be loaded either by pressing or extrusion, it was chosen as the baseline and parent explosive Al-HPE.

Since AFRL/RWME does not have an operational Holston slurry kettle, PBXN-202 was prepared by producing a lacquer of Elvax in hexane then adding the RDX

[8]The class refers to the powder grain size, and class I is similar to table sugar.

and mixing in a one-pint Baker-Perkins mixer while slowly stripping the hexane with a gentle airflow. As the solvent is removed, the mixture thickens and eventually forms a stiff dough. As the remainder of the solvent is removed, the dough crumbles to form a molding powder that will pass through a 10-mesh sieve.

Three variants of aluminized PBXN-202 called Al-HPE for "Aluminized Hot-Pressed Explosive" were formulated, whose compositions are listed in Table 1. The size of the aluminum is not specified in the table as a thorough study was being made of the effect of aluminum size on detonation parameters. The mod I variant was chosen for initial rate stick and dent experiments and has been produced with Alcan MDX-81, Valimet H-2, Technanogy 103 nm, Technanogy 50 nm, and Nano Technologies 50 nm.

Table 1: Al-HPE formulations.

Formulation	**Class I RDX**	**Aluminum**	**Elvax**
Al-HPE	80%	11%	9%
Al-HPE mod I	66%	25%	9%
Al-HPE mod II	41%	50%	9%

The Al-HPE series was mixed in the same way as the PBXN-202 described above. The bowl of the mixer was frequently lowered and the mix inspected during the mix cycle. The nanometer-scale aluminums require careful attention to the rate of solvent extraction as rapid extractions produce a very stiff lump that does not break down into free-flowing molding powder as easily as the PBXN-202 or micrometer-scale variant of Al-HPE.

All the variants of Al-HPE were successfully pressed to high densities (95%+ TMD) in 1 inch right circular cylinders by utilizing a die with an internal temperature maintained at 60 °C by a hot fluid jacket, and by preheating the samples at 60 °C in an oven. The sample was pressed at 22,000 psi with a dwell time of 18 seconds.

Utilizing a very light coating of an aerosol spray of zinc stearate mold release on the face of both the anvil and punch was found to be extremely effective in allowing the pellets to be separated from the anvil and punch without any damage to the pellets. Removal required only a gentle twist while simultaneously applying slight pressure with the hand. It was found unnecessary to use any mold release agent on the side walls of the die as they are highly polished, and no difficulty was experienced in ejecting the pellets from the die body.

4.2 Final Formulation and Charges - CR Series

As 1 inch diameter rate sticks of Al-HPE did not show any effect on the detonation velocity as a function of aluminum particle size, it was desirable to explore smaller charge diameters. The hot pressing requirement of Al-HPE and the lack of the required extrusion equipment to load PBXN-109n limited the ability to make small diameter pellets with either formulation. Therefore, a cold-pressed, oven-cured HTPB isocyanate-cured formulation was developed to allow a variety of charge diameters to be produced without large difficulty in-house.

This new process, denoted as the CR series, was developed to extend and improve the work that has been done with Al-HPE. While high-quality charges were prepared with the Al-HPE series, hot pressing is more time consuming than room temperature pressing. Handling the dies at 60 °C also required gloves, which makes working with small pellets very difficult. Therefore, the CR series utilized uncured HTPB gumstock as the binder system, and the formulation can be pressed at room temperature. Eliminating the need for temperature control allowed more repeatable samples to be produced with greater ease.

The CR series formulations were produced by a slurry process. The RDX of chosen size was placed into a container. The correct amount of premixed and uncured

gum stock binder was then added to the container. Then sufficient hexane (mixed hexanes) was added to form a very wet slurry. Aluminum powder or talc was then added if called for in the formulation. The slurry was mixed by hand or with a high-shear mixer as the hexane was stripped. The hexane dissolved the gum stock and allowed an even film to coat the particles in the mixture. It is especially important that the RDX crystals be coated to reduce sensitivity for safe handling. As the solvent was removed, the mixture resembled fresh brown sugar - a relatively free-flowing powder with a slightly wet feel.

Once the hexane was stripped to yield the brown-sugar-like powder, the mixture was put in a vacuum chamber for a few hours to remove any residual hexane. It should be noted that there was no need to sieve the resulting powder as there had been with Al-HPE, as the HTPB system does not thicken until it begins to cure - a very slow process at room temperature. The mixture was then pressed at room temperature at 25,000 psi with a dwell of 18 seconds. A very slight amount of binder exuded from the formulation while under pressure. This formed a film on the surfaces of the die barrel and anvils, which provided for an extremely smooth ejection from the die. No mold release was necessary. The pellets showed no signs of banding or streaking as a result of the pressing process.

The pressed pellets were carefully wiped with a rag to remove any binder film. The pellets were then numbered with a Sharpie and placed in a 60 °C oven and allowed to cure for 3 to 4 days. The cured pellets have shown very good dimensional stability and surface planarity, which allowed the production of a high-quality stacked-pellet charge.

CR-1 is the neat RDX formulation used as a baseline. While keeping the binder concentration constant at 6% by mass, formulations containing 10%, 20%, and 30%

additive[9] were made and are reported as the size and concentration of additive in this report. Table 2 lists the specific CR variants used in the rate stick, Gurney, and airblast experiments.

Table 2: CR series formulations - all concentrations by mass.

	Neat	10% Al	20% Al	30% Al	10% Blend	20% Blend	30% Blend	10% Talc	20% Talc	30% Talc
RDX Class I	94	84	74	64	84	74	64	84	74	64
Aluminum		10	20	30	7	14	21			
Talc					3	6	9	10	20	30
Gumstock	6	6	6	6	6	6	6	6	6	6

Talc was used as an inert additive instead of Al_2O_3 as talc is very soft and does not increase the friction sensitivity of the formulation. Talc also has a density nearly that of aluminum, which allows the density of the talc-containing formulations to be comparable to that of aluminum-containing formulations.

To quantify the quality of the CR-series mixtures, scanning electron microscope (SEM) micrographs were taken with the assistance of Dr. Sam Emery. Electron dispersion spectroscopy (EDS) was also run to show a mapping of the nanometer-scale aluminum as it is dispersed in the mixture. It is important to have an even distribution of RDX and aluminum throughout the mixture to provide a consistent chemical environment for reaction during detonation experiments.

Samples were prepared by breaking a pressed pellet of the given formulation and taking a few milligrams from the heart of the pellet with the tip of a knife. Sampling in this way captures material which has been exposed to the average processing conditions. The sample was then placed on an aluminum SEM stud which had a small piece of conductive tape affixed to the top to hold the sample. The samples were run without any conductive coating, such as sputtered gold.

[9]Additive shall mean aluminum (any size) or talc.

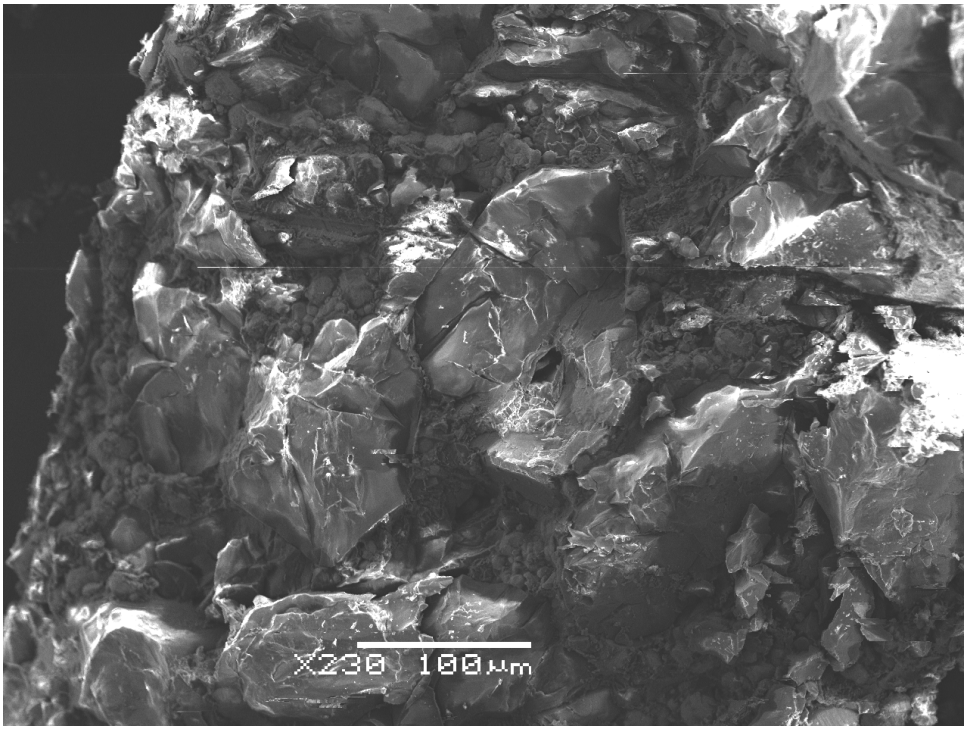

Figure 11: SEM of micrometer-scale aluminum in CR formulation.

Qualitatively, Figure 11 shows an even distribution of aluminum powder in the mixture without having any large areas that are aluminum-rich or lean (i.e. an even mixture). The larger particles in Figure 11 are the RDX crystals, and the smaller aluminum particles can be seen scattered throughout the field.

Figures 12 and 13 below also show a good distribution of nanometer-scale aluminum in the mixture. In Figure 12, the RDX and nanometer-scale aluminum can be seen as small regions of RDX with concentrated areas of nanometer-scale aluminum interspersed between the RDX crystals. Figure 13 shows the resultant map of the EDS superimposed on Figure 12 with the aluminum as red dots, and one can see that the aluminum is well distributed throughout the field as it was with the micrometer-scale aluminum.

The available SEM does not have the capability to resolve the individual nano particles, but it does show the aluminum exhibits nano or sub-micron features even when

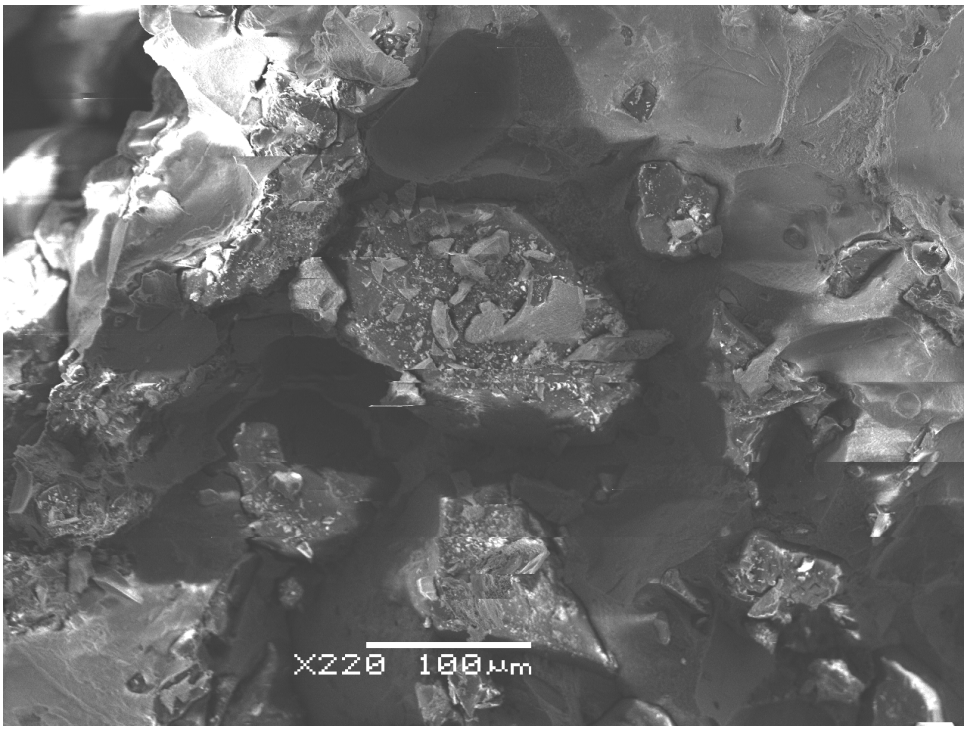

Figure 12: SEM of nanometer-scale aluminum in CR formulation.

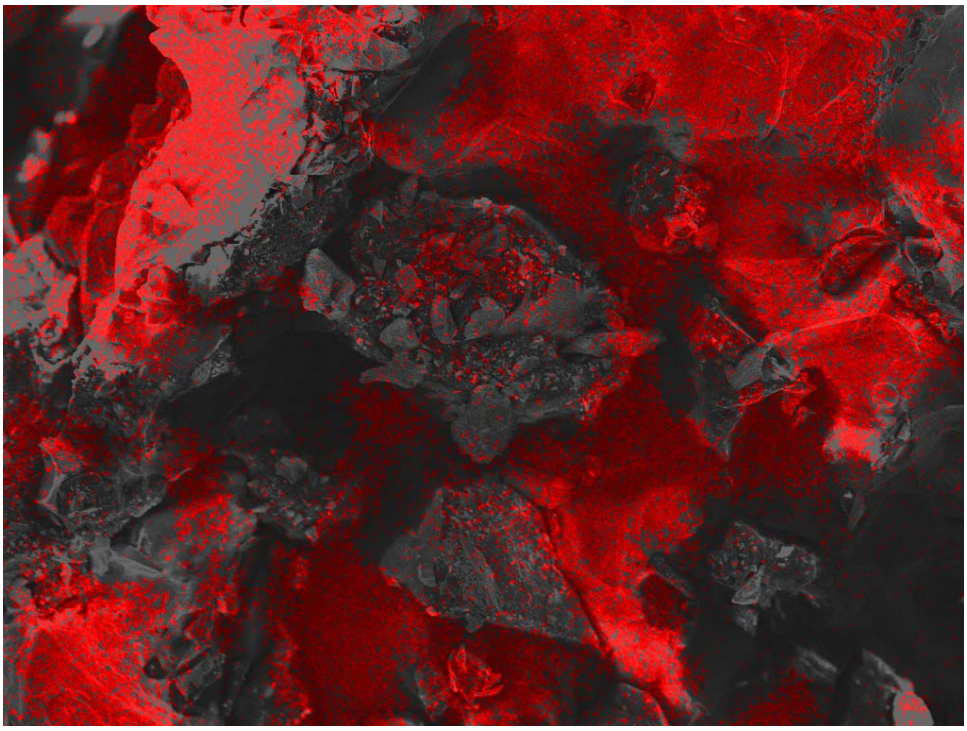

Figure 13: EDS mapping (red) of nanometer-scale aluminum in CR formulation in Figure 12.

a specific treatment, such as sonication, has not been employed to de-agglomerate the nanometer-scale material. Thus, it is reasonable to expect that the nanometer-scale aluminum is sufficiently distributed to behave differently than the micrometer-scale aluminum due to the much greater surface area that is available for chemical reaction, even if the nanometer-scale aluminum is agglomerated, which will provide a reduced surface area than would be obtained from discrete particles.

5 Detonation Velocity - Early-Time Energy Release

The two-dimensional, steady-state detonation velocity of an explosive is the result of a balance among the energy needed to drive the shock wave[10], "acoustic energy" released by the chemical reaction in the detonation reaction zone, and rarefaction losses rearward and to the sides. The reaction zone for a nearly ideal explosive, such as RDX, is on the order of 0.01-0.1 mm in thickness [50]. The front of the reaction zone consists of the Von Neumann Spike - the initial high pressure shock starts the chemistry. The rear boundary of the reaction zone is the sonic plane. Any energy released by the chemical reaction behind the sonic plane will have no influence on the detonation as impulse produced by the acoustic energy - pressure wave energy - will not be able to catch up to the detonation.

The detonation wave is traveling at approximately 8,000 m/s and the thickness of the reaction zone allows one to calculate the residence time in the reaction zone. Therefore, the time-scale necessary for addition of acoustic energy to the reaction zone can be estimated to be on the order of 0.1 µs for an RDX or similar explosive with a reaction zone thickness on the order of 1 mm and a detonation velocity of 8,000 m/s. Any net energy release by nanometer-scale aluminum in under $\approx$ 0.1 µs will contribute acoustic energy to the reaction zone, and the detonation energy will increase over that of an explosive containing traditional aluminum powder.

5.1 Rate Stick Experiments

A rate stick is used to determine the detonation velocity of an explosive. The experiments are straightforward and are relatively inexpensive to perform. In the case of this work six (6) pellets were glued on top of one another to form a stick of explosive

[10] A shock must be driven through the explosive as the shock will otherwise decay into a pressure wave.

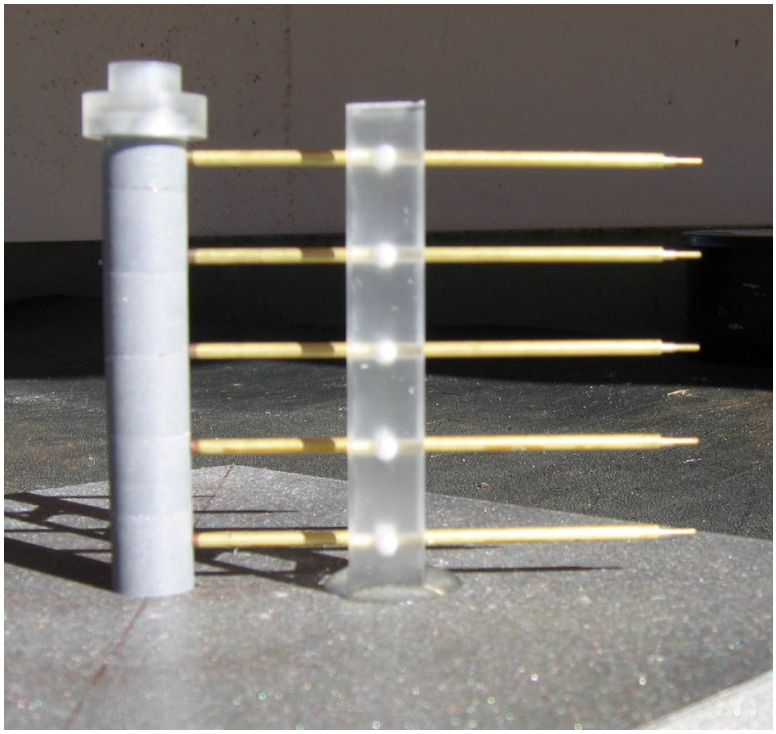

Figure 14: A rate stick set up with 1/2 inch diameter pellets.

3" long. The stick was then instrumented with piezo pins as shown in Figure 14. The pins are activated when the shock front sweeps past them as shown in Figure 15. Each pin produces a voltage spike that is recorded on an oscilloscope. Since the spacing of the pins as well as the time of arrival of the shock front is known, the detonation velocity can be calculated with Eq. 22, where D is the detonation velocity; d_{pins} is the distance between the pins, and t_{pins} is the time it takes the shock wave to travel the distance, d_{pins}.

$$D = \frac{d_{pins}}{t_{pins}} \tag{22}$$

Rate stick experiments have been conducted for the CR series, and the detonation velocity, D, as a function of particle size and charge density, ρ_0, was examined. All of the CR series rate sticks were 1/2 inch diameter and contained 20% by mass additive. Since the particle size impacts the ρ_0 achieved when pressing the pellets, two sets of

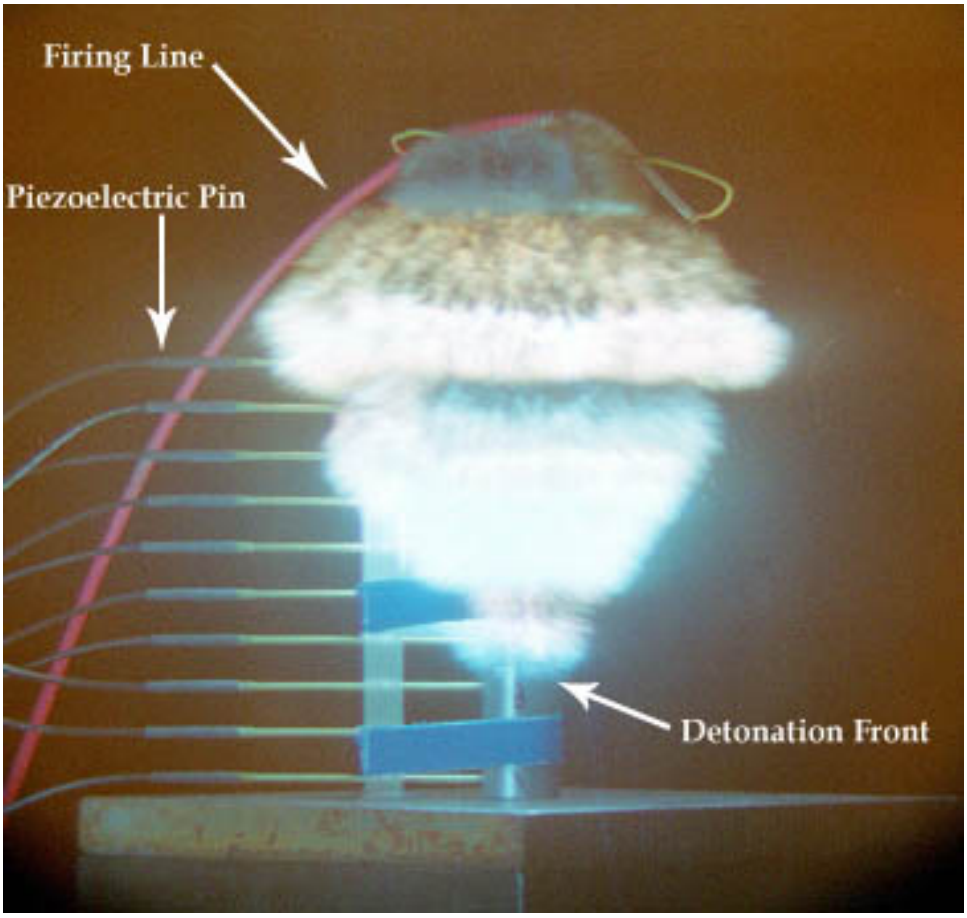

Figure 15: Framing camera image of 1 inch diameter rate stick detonation.

experiments were carried out by varying ρ_0. The first case consisted of pressing the pellet with a pressure of approximately 25,000 psi. A second set was then carried out at a ρ_0 approximately 15% lower than the ρ_0 obtained with a pressure of 25,000 psi to explore the effect of particle size on $dD/d\rho_0$. Once $dD/d\rho_0$ is known, all of the rate stick data can be adjusted to allow rate comparisons to be made at the same ρ_0 as D is a function of ρ_0.[11]

[11]This assumes that the extent of reaction of the aluminum does not vary with ρ_0, but detonation front temperature does vary with ρ_0, so the rate of aluminum reaction may vary.

5.2 Rate-Stick Results

The initial testing of a first attempt formulation Al-HPE consisted of a series of simple rate-stick shots. The charges were composed of six (6) 1 inch x 1 inch pellets prepared by hot pressing at 22,000 psi. The pellets were glued together with a very thin layer of 5-minute epoxy utilizing a BF_3 cure that, unlike traditional amine cures, is compatible with the explosive. The charge was then placed on a steel witness plate and held in firm contact with a piezo pin bar. The pins had a nominal spacing of 15 mm over the length of the charge. The resulting 1 inch x 6 inch charges were primed with a single 1 inch x 1 inch pellet of A5, an-easy-to detonate explosive, and were fired with a Reynolds RP-501 detonator.

The velocities were averaged over the three (3) pins covering the last 45 mm of the charges and are shown in Table 3. A standard uncertainty analysis was performed for

Table 3: Al-HPE based rate sticks with 25% aluminum powder by mass.

Formulation	D	2σ
PBXN-202	8000 m/s	25 m/s
Al-HPE with tritonal aluminum	7822 m/s	25 m/s
Al-HPE with 30 µm aluminum	7820 m/s	25 m/s
Al-HPE with 100 nm aluminum	7855 m/s	25 m/s
Al-HPE with 50 nm aluminum	7825 m/s	25 m/s

the data acquisition system used for this series. The level of uncertainty in the detonation velocity was approximately 25 m/s based upon a standard error propagation technique. The results do not show any statistically significant differences among the aluminum powders of various sizes in the formulations. It is clear, however, that the addition of 25% aluminum powder has reduced the detonation velocity quite noticeably from the neat RDX formulation, presumably due to the reduction of RDX and the endothermic heating of the aluminum. A talc or aluminum oxide formulation was not tested for the Al-HPE series. With an uncertainty of this magnitude, it is not

possible to differentiate the detonation velocities of the explosives using 100 nm and 50 nm sizes of nanometer-scale aluminum powder or to differentiate the detonation velocities of nanometer-scale aluminum formulations vs. micrometer-scale aluminum formulations.

The results of the rate-stick experiments conducted using the CR series formulation with 20% additive to include micron aluminum, nanometer-scale aluminum, and talc are shown in Table 4. The values of ρ_0 and the associated detonation velocities, D, values are shown. The value for $dD/d\rho_0$ was determined for each formulation. D for a $\rho_0 = 1.65$ g/cc was calculated based on that value and is listed as the last column in the table. The standard deviation, σ, of D for each ρ_0 was calculated and the value of 2σ is shown in the table as well.

Given the small variations in D for each formulation and the value of 2σ, the D values calculated for $\rho_0 = 1.65$ g/cc are statistically identical for the formulations with additives at 20% by mass. The neat formulation has the fastest D by approximately 1,000 m/s; this was expected, based on the behavior of standard aluminized explosives.

Future work exploring the effect of explosive mass dilution on the neat charges might prove to be complementary to this study. Given that the aluminum and inert talc produced approximately the same values for D, one would like to be able to separate out the dilution effect from that of inert mass heat and momentum sink. Producing charges with a low enough *uniform* density is challenging, and they tend to be very difficult to handle due to their inherent fragility.

Table 4: Measured detonation velocities of formulations tested at both high(+) and low(-) ρ_0. The predicted D value at $\rho_0 =$ 1.65 g/cc is based on the experimentally obtained values for $\frac{\triangle D}{\triangle \rho_0}$.

Additive	ρ_0 g/cc	D km/s	2σ km/s	Slope (km/s)/(g/cc)	y intercept	D @$\rho_0 = 1.65$ g/cc km/s
50 nm						
$\rho_0 +$	1.70	7.52	0.04			
$\rho_0 -$	1.58	6.77	0.08			
$dD/d\rho_0$				6.32	-3.27	7.15
Aldrich						
$\rho_0 +$	1.75	7.73	0.02			
$\rho_0 -$	1.63	7.15	0.05			
$dD/d\rho_0$				4.84	-0.73	7.25
GD						
$\rho_0 +$	1.73	7.67	0.03			
$\rho_0 -$	1.56	6.62	0.03			
$dD/d\rho_0$				6.09	-2.91	7.14
X-81						
$\rho_0 +$	1.76	7.83	0.02			
$\rho_0 -$	1.65	6.98	0.03			
$dD/d\rho_0$				7.25	-4.95	7.02
talc						
$\rho_0 +$	1.75	7.50	0.03			
$\rho_0 -$	1.61	6.97	0.10			
$dD/d\rho_0$				3.7143	0.99	7.12
H-5						
$\rho_0 +$	1.76	7.85	0.01			
$\rho_0 -$	1.63	6.90	0.02			
$dD/d\rho_0$				7.09	-4.65	7.05
neat						
$\rho_0 +$	1.58	7.83	0.05			
$\rho_0 -$	1.41	7.04				
$dD/d\rho_0$				4.51	0.69	8.14

6 Gurney Energy and Plate Dent - Mid-Time Energy Release

If the nanometer-scale aluminum combusts with a net exothermic energy on a time scale on the order of 0.1 µs, the energy released will be ahead of the sonic plane and will help drive the detonation wave and increase detonation velocity and detonation pressure. Such an enhancement will also increase the Gurney energy over that of a standard aluminized formulation. The rate-stick experiments showed that nanometer-scale aluminum had the same effect as micrometer-scale aluminum on D in that the value of D was decreased, but energy released within approximately 10 µs will also contribute energy that will couple to the metal acceleration and enhance the Gurney energy for a 1/2 inch diameter tube.

Cooper has shown the Gurney velocity for high-density explosives can be estimated by Eq. 23, which is an empirical relation fit to a large data set [22].

$$\sqrt{2E} = \frac{D}{2.97} \tag{23}$$

The Gurney energy of an explosive is independent of the geometry or configuration. Thus, an increase in the detonation velocity, D, will generally increase the Gurney energy for a given initial density, ρ_0. This relation, however, is based upon a data set of standard explosives and does not take into account mid-time energy release from nanometer-scale aluminum or other additive. Such an addition of mid-time energy will require a new model or perhaps empirical fit to describe the metal-acceleration performance.

As the Gurney velocity is associated with Pdv work, energy released by the aluminum a few microseconds after detonation should also help to accelerate metal by adding heat to the working fluid - the explosion product gases. For the case of the test, described in the next subsection, the Gurney velocity is taken at the point of

seven (7) volume expansions of the cylinder. Beyond this point, the copper cylinder begins to fracture and gas escapes without accelerating the metal as efficiently as when the tube is leak-free. Energy released at a later time will be in the afterburn zone and only contributes energy to the airblast.[12] Traditional aluminized explosives have values of $\sqrt{2E}$ that are less than the neat explosives themselves, as a sufficient fraction of the aluminum does not react with the required promptness to accelerate the fragments. When the aluminum does not react during the fragment acceleration time period, it simply becomes an inert mass that is carried along with the detonation product gas flow, and thus is a burden that tends to reduce the value of the Gurney velocity, $\sqrt{2E}$.[13]

6.1 Measuring the Gurney Velocity - Classic Streak Camera Method

The Gurney velocity has traditionally been measured with a cylinder expansion test commonly referred to as a cylex test. The cylex test is typically conducted with a charge diameter of 1 inch for ideal (thin reaction zone) explosives such as RDX, HMX, and PETN-based formulations. The high-purity copper tube typically has a wall thickness of one tenth the charge diameter and is 12 inches long. Therefore, a 1 inch internal diameter cylex tube has a wall thickness of 0.100 inches and a total outside diameter of 1.200 inches.

The charge is placed level and on end upon a table and initiated from the top as shown in Figure 16. The white megaphone-shaped object in the foreground of

[12]This is why, historically, high-brisance and high-blast explosive formulations have been developed as there is a tradeoff in performance.

[13]It is important to remember that C is the mass of the explosive fill to include the aluminum or talc - the RDX has indeed been reduced, but the value of C has only fluctuated slightly with ρ_0 variation due to press-ability of each formulation, and the variation of ρ_0 is accounted for when calculating the value of $\sqrt{2E}$.

Figure 16: A typical cylex test setup.

Figure 16 is an argon candle and is used to back-light the cylex cylinder. The argon gas in the candle is excited by the shock induced upon detonation of the explosive pad on the small end of the candle. When the gas returns to the ground state, a photon is emitted and a very bright flash is produced. The argon-candle technique is very reliable and controllable, and therefore is often preferred to much more expensive discharge tube or flashbulb light sources.

A streak camera is focused on the cylinder approximately 3 inches above the bottom of the charge. The camera continuously records the image seen through a very narrow slit as a function of time as is shown in Figure 17. The right hand side the image in Figure 17 is the dynamic still which is used as a fiducial. This image is taken before the test is fired and without the horizontal slit in place. With the fiducial reference, and knowing the writing rate of the camera in mm/µs (mm of film written per µs), one can transform the data in Figure 17 from $x - y$ space to $x - t$ space. The radial displacement of the cylinder wall is then known as a function of time.

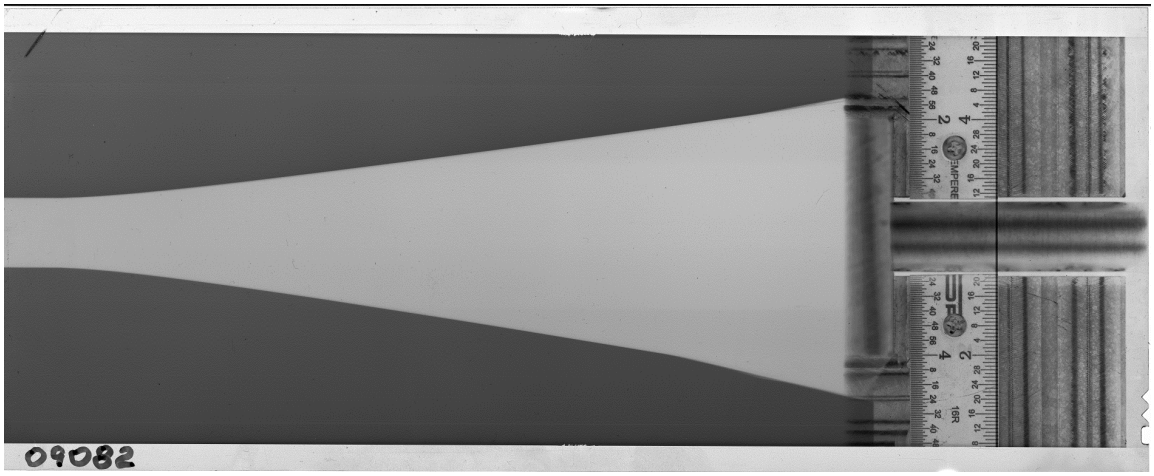

Figure 17: A typical cylex test record taken with a streak camera.

The line between the dark and light areas seen in Figure 17 is the edge of the copper tube. An automated routine has been developed using edge detection algorithms with the software package Igor Pro to find the edge of the tube on a scanned film record [51]. The data are then fit, and the Gurney velocity is calculated.

The streak camera captures the radial velocity component of the cylinder wall as the cylinder expands once the detonation wave has swept past the camera slit view. Figure 18 shows the geometry of the expanding cylex tube. Point P is the initial position of a wall element, and point P' is the position of the same wall element post detonation. The vector V is the metal velocity; V_n is the component normal to the direction of wall travel, and V_r is the radial component we measure with the streak camera and/or VISAR directed normal to the wall prior to the detonation.

To compute the Gurney velocity, the true tube-wall velocity vector V should be used even though people often use V_r and skip the correction. To compute V based on V_r, we refer to Figure 18 and develop the following equations.

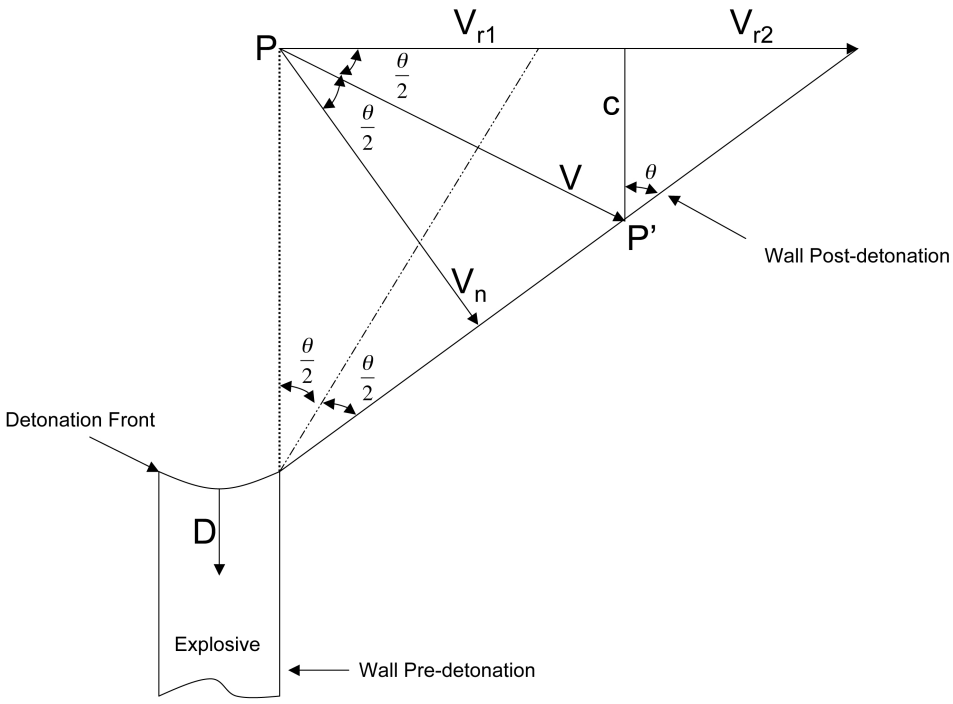

Figure 18: Turning angle correction to evaluate wall velocity, V.

The tube wall is turned through an angle θ as the detonation passes a point P on the wall. The radial velocity is broken down into two parts, V_{r1} and V_{r2} as shown in Figure 18. Therefore,

$$V_r = V_{r1} + V_{r2} \tag{24}$$

then,

$$V_{r1} = V \cos\left(\frac{\theta}{2}\right) \tag{25}$$

$$c = V \sin\left(\frac{\theta}{2}\right) \tag{26}$$

$$V_{r2} = c \tan(\theta) = V \sin\left(\frac{\theta}{2}\right) \tan(\theta) \tag{27}$$

and upon rearrangement,

$$V = \frac{V_r}{\cos\left(\frac{\theta}{2}\right) + \sin\left(\frac{\theta}{2}\right) \tan(\theta)}. \tag{28}$$

The angle θ is measured by examining the expanding cylinder with a framing camera and measuring the angle the post-detonation wall makes with the wall ahead of the shock front. In the case of CR-1, the RDX+binder reference explosive, θ was found to be approximately 12°.

To get an accurate record, one needs to allow the detonation to become steady, which can require a few diameters of run, and not allow the rarefaction wave from either end of the charge to affect the movement of the cylinder wall. The rarefaction wave from the end of the charge will impact the movement of the cylinder wall near the end of the charge before the seven-fold volume expansion is complete. Therefore, the slit view of the camera is located approximately 2/3 of the distance down the length of the tube. To find the value of $\sqrt{2E}$, Eq. 29 is used. The test yields the metal velocity, V, and we know the charge mass, C, and the metal mass, M.

$$\frac{V}{\sqrt{2E}} = \left(\frac{M}{C} + \frac{1}{2}\right)^{-1/2} \tag{29}$$

6.2 Measuring the Gurney Velocity - PDV Method

The main disadvantages of the traditional cylex test are the amount of time required to set the shot up and the expense of the tube, as it is a custom-made item. With the case of nanometer-scale aluminum, or other materials in relatively short supply, the amount of explosive sample material is also an issue. Therefore, the 1/2 inch diameter cylex test was developed in-house and a measurement system analysis (MSA) was conducted to determine its suitability [52]. The 1/2 inch test had an experimental uncertainty in the value of $\sqrt{2E}$ on the order of 2-5% which is similar to that of the 1 inch standard test [52].

To run three traditional cylex tests with streak camera diagnostics for repeatability would require 3 days or so of time at the test facility as well as many hours

in the lab producing the charges. Therefore, a photon doppler velocimetry (PDV) system was built and used to acquire the wall-velocity data of the cylex tubes.

PDV makes use of the Doppler shift of laser light which is reflected off the moving target surface. The supplied light is focused onto the tube by the probes shown in Figure 22. The light reflected off the cylinder wall is also collected by the same probe. The reference light and return light were combined and routed to a detector connected to a 12.5 GHz single-shot bandwidth oscilloscope, which recorded the heterodyne signal [53]. The raw data are analyzed by a sliding FFT algorithm to determine the beat frequency at a given time which corresponds to the velocity of the moving target. The algorithm used was developed in-house using Igor Pro [54].

There was a concern that pellets fit very tightly together so as not to cause jetting at each pellet-to-pellet interface, since the jetting may prematurely puncture the copper tube wall. The pellets also need to fit tightly in the tube as a gap between the pellet and cylinder wall will influence wall velocity [20]. Unfortunately, even with tightly fitting pellets, some disturbance from jetting may occur.

Preliminary tests with stacked pellets were performed and the radiograph of the left loaded tube is shown in Figure 19. As can be seen within the limits of resolution, the pellet interfaces are consistent in appearance, as is the fit within the tube wall. The pellet interfaces are visible, however. To achieve the tightest possible interfaces, a thin film of silicone vacuum grease was applied to the face of each pellet. The top and bottom pellets were glued to the tube with epoxy and a hand screw clamp was used to apply 200-300 pounds of force to the column of pellets as the epoxy cured.

Even with these steps, pellet-to-pellet interfaces caused early jetting in the tube as is shown in Figure 20, which was obtained with a framing camera at 500,000 frames per second. The early release of gas pressure will alter the test, and therefore, this configuration will not work for obtaining the Gurney velocity.

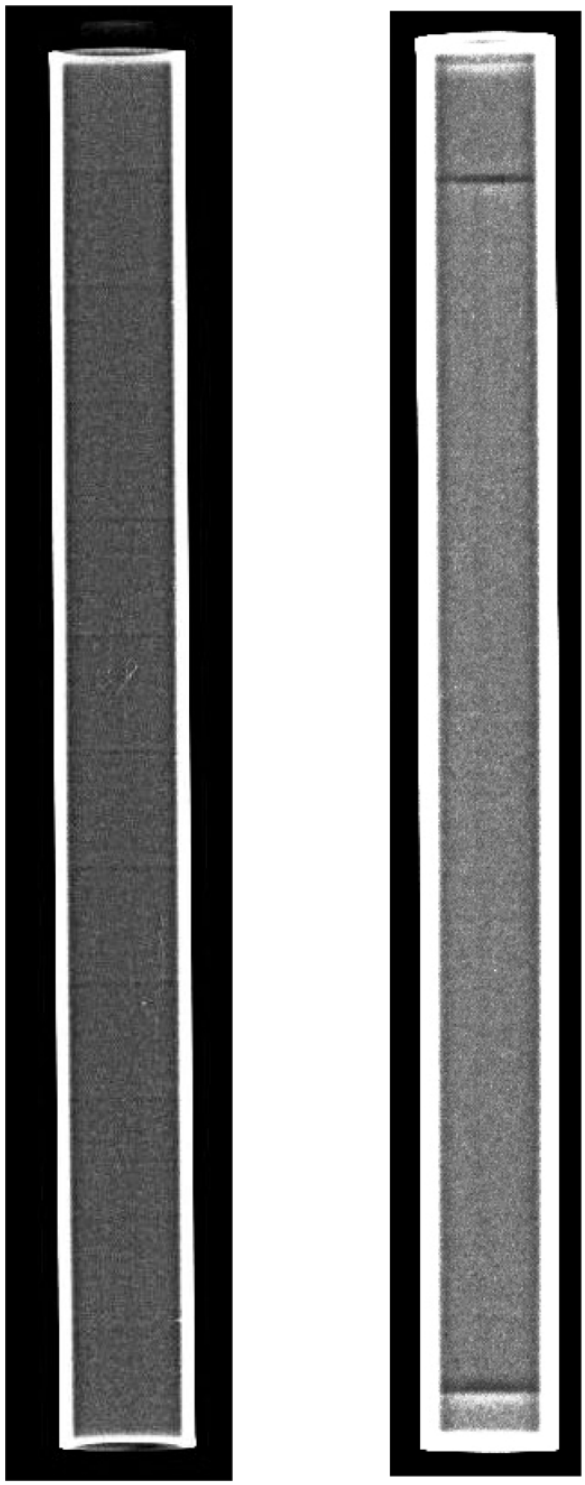

Figure 19: Radiograph of 1/2 inch diameter cylex cylinders loaded with pellets on the left and direct pressing on the right.

Figure 20: Detonation of 1/2 inch diameter cylex cylinder loaded with CR-1 pellets (1 inch major division graph paper as the background).

Custom tooling was produced to directly press the explosive into the cylex tube and eliminate the discrete pellet-to-pellet interfaces as well as eliminate the air gap between the pellets and the tube wall. Figure 21 shows the detonation of a 1/2 inch cylex tube directly loaded with TNT at 25,000 psi. The tube remains intact well past the seven-fold volume expansion diameter. Therefore, the direct loading technique with 1/4 inch thick increments was employed for the cylex testing. The right tube in Figure 19 shows the result of the direct pressing. One can see a booster pellet at the top and an aluminum backing plug at the bottom of the tube. The pressed center column of explosive is very uniform and does not suffer from the pellet-to-pellet interfaces that cause jetting.

The setup with the PDV apparatus is much less cumbersome than the streak

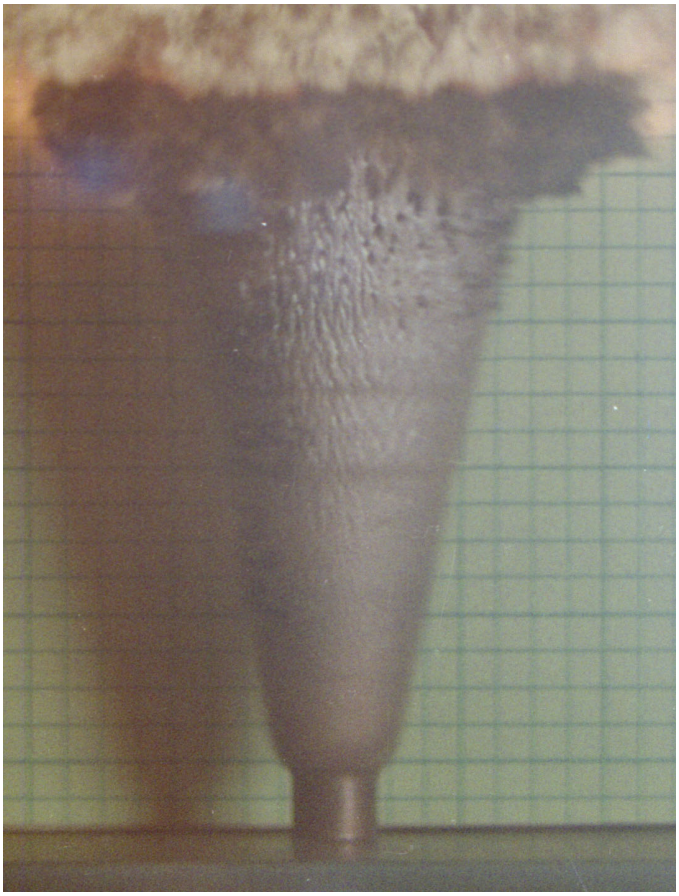

Figure 21: Detonation of direct pressed TNT cylex tube (1/4 inch graph paper as the background).

camera in that the argon candle is not needed nor is precision alignment and leveling with the streak camera. Instead, a simple self-aligning fixture was designed and produced by Infinity Tool of Waukesha, WI, which holds four laser probes perpendicularly to the copper tube at a precise axial spacing of 1 inch. The test item is shown in Figure 22.

The copper tube is securely held in the aluminum fixture. One can see the v-notch with a center relief a the bottom of the aluminum fixture. An identical notch is at the top of the fixture as well. The notches automatically align the tube in a repeatable fashion without requiring any special effort or measurement. Each of the laser probes was held in place with set screws after being aligned to an inert tube

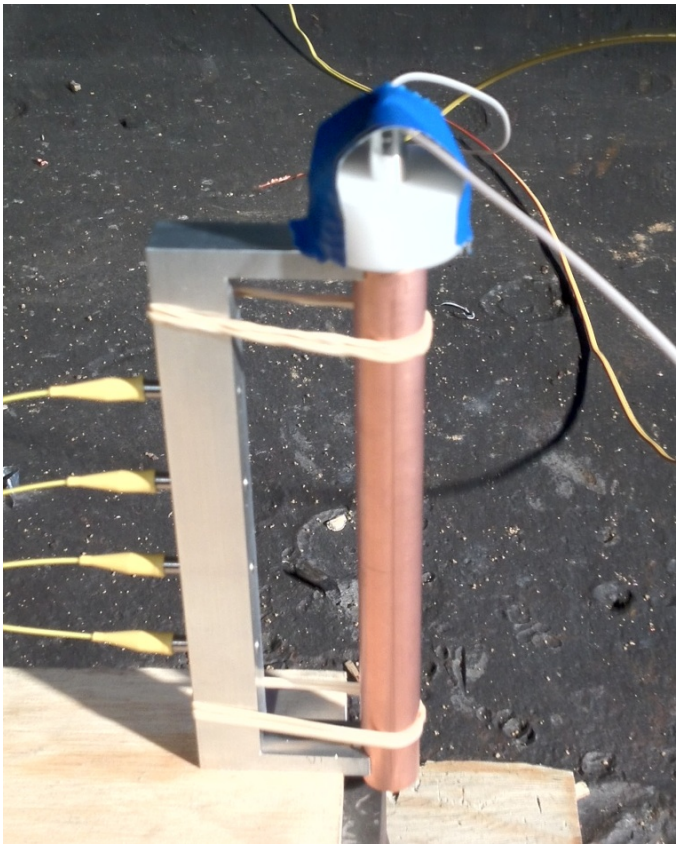

Figure 22: A 1/2 inch cylex test ready to be fired with PDV diagnostics.

with a return loss meter. As the holes that hold the probes are carefully reamed, the probe body is automatically held perpendicular to the tube. The lens is not exactly in perfect axial alignment in the probe body, which requires rotating the probe to achieve the best alignment and, hence, light return to the probe. The detonator is held in place with the plastic fixture that is glued to the top of the copper tube. The tube is held onto the aluminum fixture by rubber bands, which were very effective. The fixture is bolted to a square of plywood to keep the bottom of the tube elevated off the floor to prevent any misalignment induced by contact with the floor.

Data from an example shot containing X-81 aluminum are shown in Figure 23. Each channel is plotted as velocity vs. absolute time. One can use this format to obtain D, as the spacing between probes is known. The laser probes in effect become

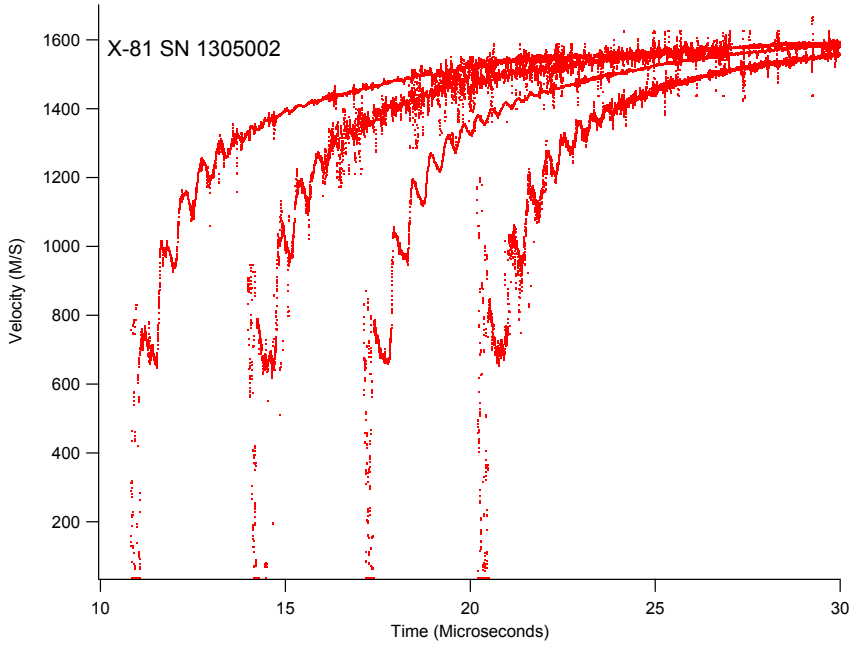

Figure 23: Wall velocity vs. time for 20% by mass X-81 aluminum with PDV diagnostics.

non-contact optical pins. A comparison was performed with a nitromethane shot to determine how sensitive feature selection was for detonation velocity measurement. Figure 24 shows the velocity vs. time data for the nitromethane shot as well as hand circled features used to obtain values for D. One can see that as long as a prominent feature is consistently selected, the value obtained for D is quite insensitive to the feature which is chosen. The data shown in Figure 23 are then integrated to obtain wall-velocity vs. wall-displacement data, which are used to determine the value of the Gurney velocity ($\sqrt{2E}$) with Equation 29 on page 46. Figure 25 shows the integrated data for all four channels of the X-81 shot.

One can see the early-time shock-up[14] of the cylinder. These early-time data

[14]The shock-up is the early time ringing of the cylinder wall as the shock in the copper travels back and forth between the inner surface and outer surface of the cylinder wall.

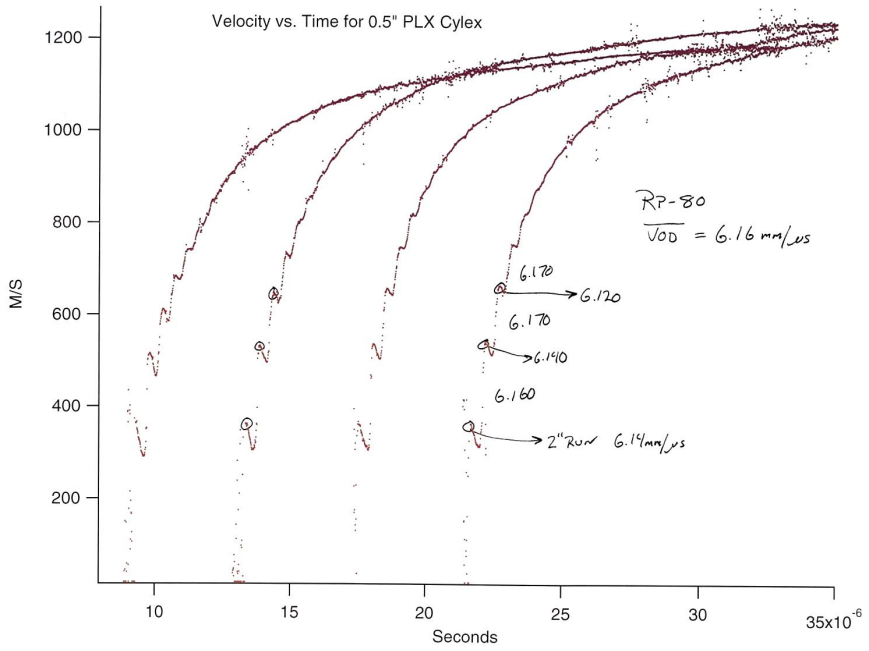

Figure 24: Velocity of detonation of nitromethane with PDV.

are not typically available when using the streak camera for small-diameter shots. Additionally, it is important to note the data are nearly identical for each of the four channels, evidence that the detonation has reached a steady state that is stable over the region in which the data are taken.

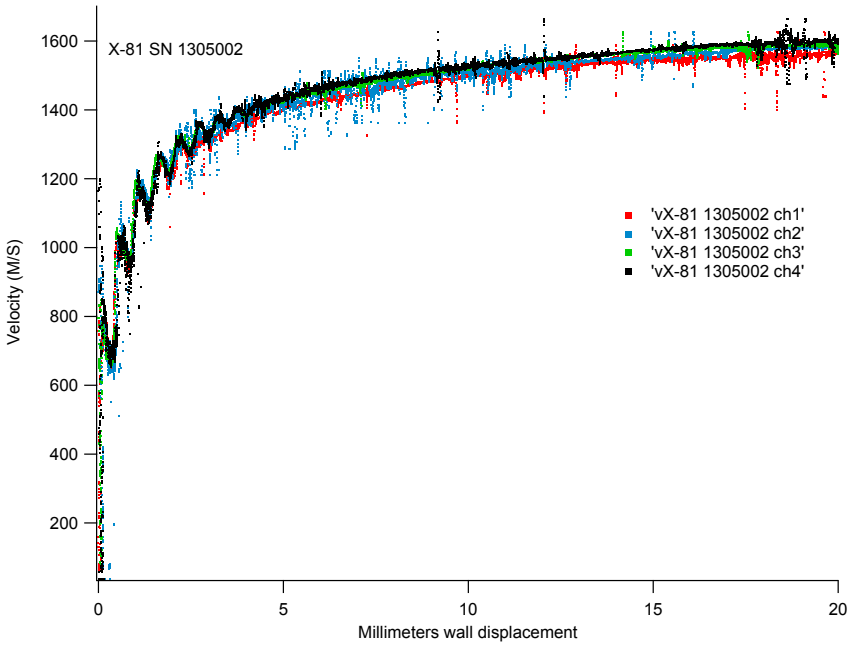

Figure 25: All four channels integrated to show radial component displacement with PDV.

6.3 Gurney Velocity Results

A series of 1/2 inch cylex tests was run with PDV diagnostics as a function of the aluminum particle size. All of the formulations contained 20% by mass additive but for the neat CR-1, of course. The average values of the Gurney velocity are listed in Table 5. The value of the Gurney velocity of the neat explosive CR-1 is

Table 5: Average values of the Gurney velocity for various CR series formulations with an experimental error of $\approx 3\%$.

Formulation	$\sqrt{2E}$
CR-1(neat)	2.86 mm/µs
50 nm	2.65 mm/µs
100 nm	2.66 mm/µs
H-5	2.53 mm/µs
GD	2.60 mm/µs
X-81	2.56 mm/µs
X-81/Talc	2.58 mm/µs
Aldrich	2.48 mm/µs
Talc	2.59 mm/µs

greater than all of the aluminum additive formulations. The two nanometer-scale aluminum formulations provide the largest value of the $\sqrt{2E}$ at 2.65 mm/µs and 2.66 mm/µs of all of the additives. The Aldrich aluminum is a very large flake, much like ground aluminum foil, and provides the lowest average value for the $\sqrt{2E}$ of 2.48 mm/µs, even lower than the inert talc value of 2.59 mm/µs. The values are not statistically different of any of the additive formulations and the main conclusion is that simply adding nanometer-scale aluminum to a formulation does not improve the metal accelerating ability of the explosive significantly over that of micrometer-scale aluminum or even the talc or talc/X-81 blend. The aluminum acts as an inert particle and Kennedy [55] has proposed a modification to the standard Gurney equation to account for an inert mass that is mixed in with the explosive charge

shown in Equation 30,

$$v = \frac{\sqrt{2E(1-x)}}{\sqrt{\frac{M}{C} + \frac{1}{2}}}, \tag{30}$$

where x is the mass fraction of the inert material mixed in with the explosive. When the value the Gurney velocity ($\sqrt{2E}$) measured for the neat CR-1 formulation is used in Equation 30, the value of the wall velocity, v, agrees well with the measured wall velocities for the inert laden cylinder tests lending further credence that the aluminum, and talc, behave as inert particles.

6.4 Plate Dent - Experiment and Modeling

Plate dent-tests were run on three of the additive formulations to investigate the performance in the configuration of end on vs. grazing detonation. In addition, a low density version of the neat CR-1 formulation was also tested to compare the effect of particle loading to air voids. In the plate dent test, a cylinder of explosive is detonated with the end opposite the detonator resting on a flat steel plate. The interaction of the detonation products with the steel plate produces a dent or crater that can be measured and used to compare the effective driving impulse provided by the explosive. The setup is shown in Figure 26 and consisted of a detonator, a booster pellet, four pellets under test, and the steel plate. The piezo pins were used to verify the detonation velocity. The objective of this test was to compare the relative dents of the formulations and not to correlate the depth of the dent to a certain pressure.

Each of the formulations was shot in triplicate on the 3/4 inch thick mild steel witness plate, and an example of the resulting dents are shown in Figure 27.

The initial density, ρ_0, was chosen as the maximum density that was achieved by pressing the 100-nanometer aluminum formulation into the 1/2 inch x 1/2 inch

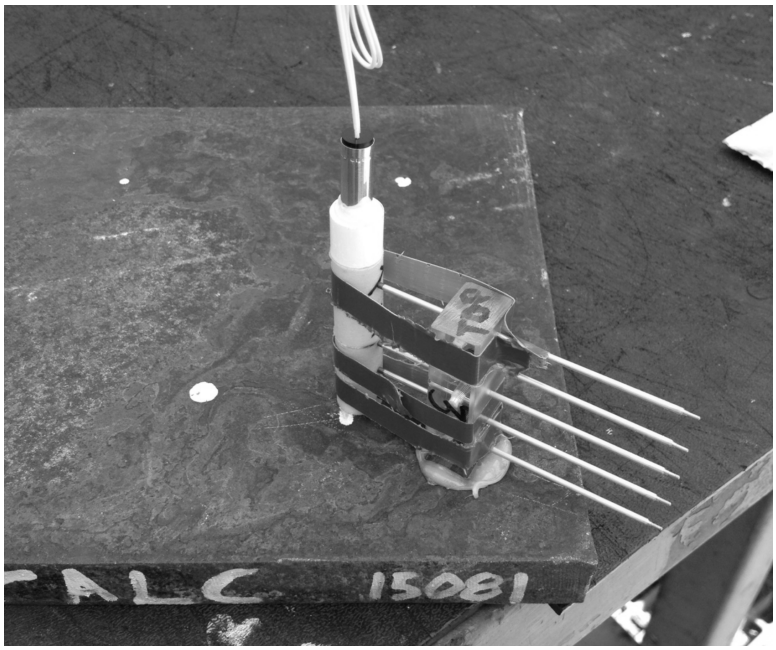

Figure 26: The setup of a 1/2 inch diameter dent test on a 3/4 inch thick steel witness plate.

pellets. The other formulations containing micron aluminum (X-81) and talc were then pressed to the same density of 1.74 g/cc. Since the dent test made use of discrete pellets, the density of each formulation could be specified, unlike direct pressing of the tubes where repeated compaction cycles yield a high density loading. The neat formulation was pressed to a density of 1.38 g/cc as this represents the effective density of the explosive and binder contained in the 20% additive formulations. This offered the opportunity to measure the effect of inert particle loading vs. void on the dent depth.

The resulting dents were measured with a height gauge fitted with a rounded-tip stylus. The base of the gauge was rested on parallel bars, which in turn rest on a large parallel ring positioned on the plate in such a way as to be on the undisturbed areas of the metal. The gauge was set to zero with the stylus in contact with an undisturbed (flat) area of the plate and the dents were measured by moving the

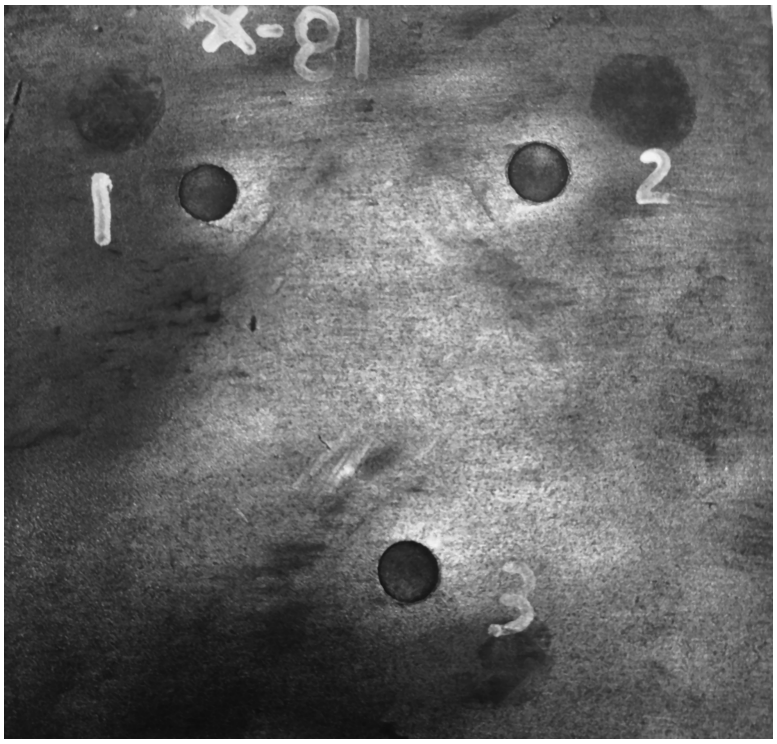

Figure 27: The resulting dents on the steel witness plate.

stylus in the bottom of the crater and feeling for the deepest portion. The deepest value was then recorded.

Based on the results shown in Table 6, the dent depths were effectively the same for all of the formulations. This means that the particles are acting in an inert

Table 6: The average measured dent depths.

Formulation	Average Depth
Neat	0.078 inches
100 nm	0.083 inches
30 µm	0.087 inches
Talc	0.079 inches

fashion on the timescale of the dent production, which is estimated to be on the order of 10-15 µs based on CTH hydrocode simulations. It is also interesting to note that the inert particles are not enhancing or detracting from the formation of the

dent as compared to the neat formulation containing a large volume of air void. In fact, when the low ρ_0 of the neat formulation is corrected using the Kamlet-Finger relation [20] shown in Equation 31, the dent of 0.078 inches has a corrected value of 0.085 inches, with the assumption that dent depth is directly proportional to the value of $\sqrt{2E}$, which lies right in the middle of the aluminized formulations. The term Φ is a fitting parameter allowing for changes in chemistry. As the explosive is unchanged, Φ is assumed to be constant for the two cases and cancels.

$$\sqrt{2E} = 0.887\Phi^{1/2}\rho_0^{4/10} \tag{31}$$

The correction for ρ_0 is made as the air in the void is highly compressible while the aluminum additive is not. These results are consistent with the cylinder test data measured for the same formulations with the exception of the low ρ_0 neat formulation as a low ρ_0 was not possible in the direct press cylinder configuration.

With the assistance of Dr. Chip Butler, the CTH hydrocode was used to model the interaction of an aluminum particle with the detonation shock and product gas flow. Two cases were run. The first case consisted of a single spherical 30 µm aluminum particle located one particle diameter above the surface of the steel plate. The second case had the particle in contact with the steel plate. The model made use of boundary conditions to effectively make the diameter of the explosive infinite. Therefore, edge effects, such as wave curvature, were not accounted for in this model. On the scale of a 1/2 inch-diameter charge, the local wave curvature will appear to be flat with respect to a 30 µm particle. An actual 1/2 inch-diameter charge could not be modeled with the resources available due to the disparate length scales. The resulting number of computational nodes required to resolve a 30 µm particle in a realistic explosive charge would not be a tractable problem.

Figure 28 parts a-d shows the interaction of the shock wave and detonation prod-

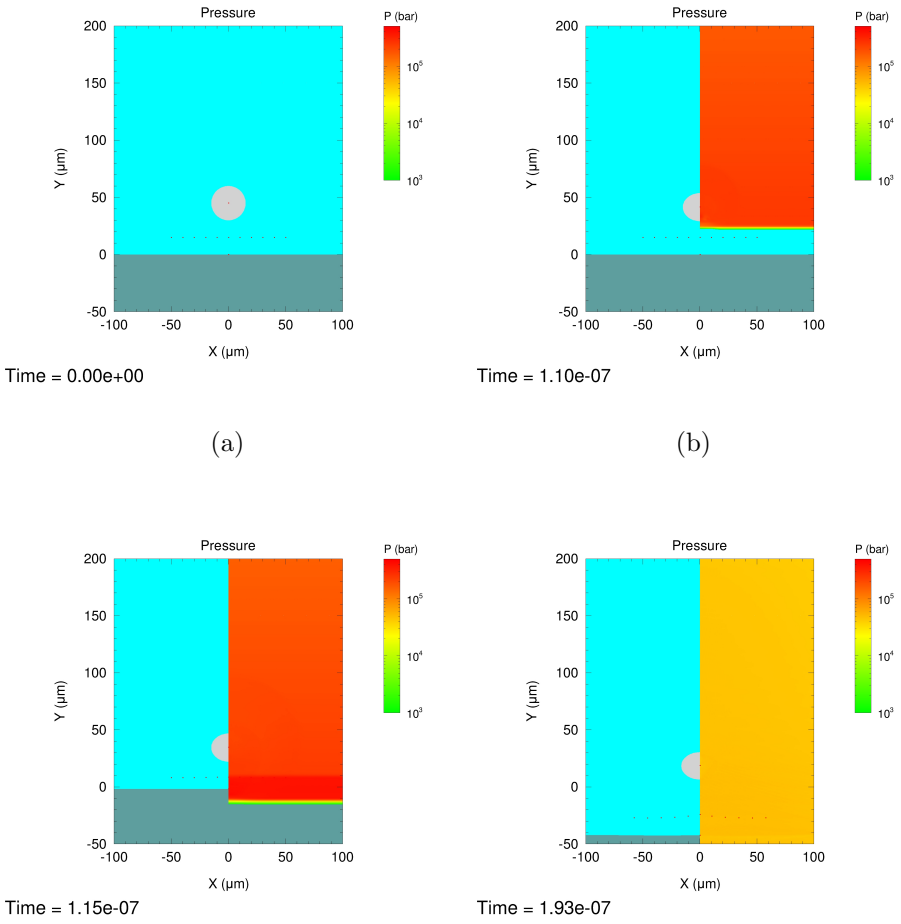

Figure 28: The results of a CTH hydrocode simulation - the aluminum particle is accelerated, but it does *not* make contact with the steel plate.

ucts with a 30 μm spherical aluminum particle with an initial position of one diameter above the surface of the steel witness plate. The passage of the shock does accelerate the aluminum particle towards the plate to a peak velocity of approximately 1,500 m/s, but the particle remains entrained in the detonation product flow and does not come into contact with the plate. Rather, the particle is rapidly decelerated by a reflected shock in the high density product gases, which serves to stagnate the product gas flow. CTH does not capture the turbulence-induced mixing in the flow

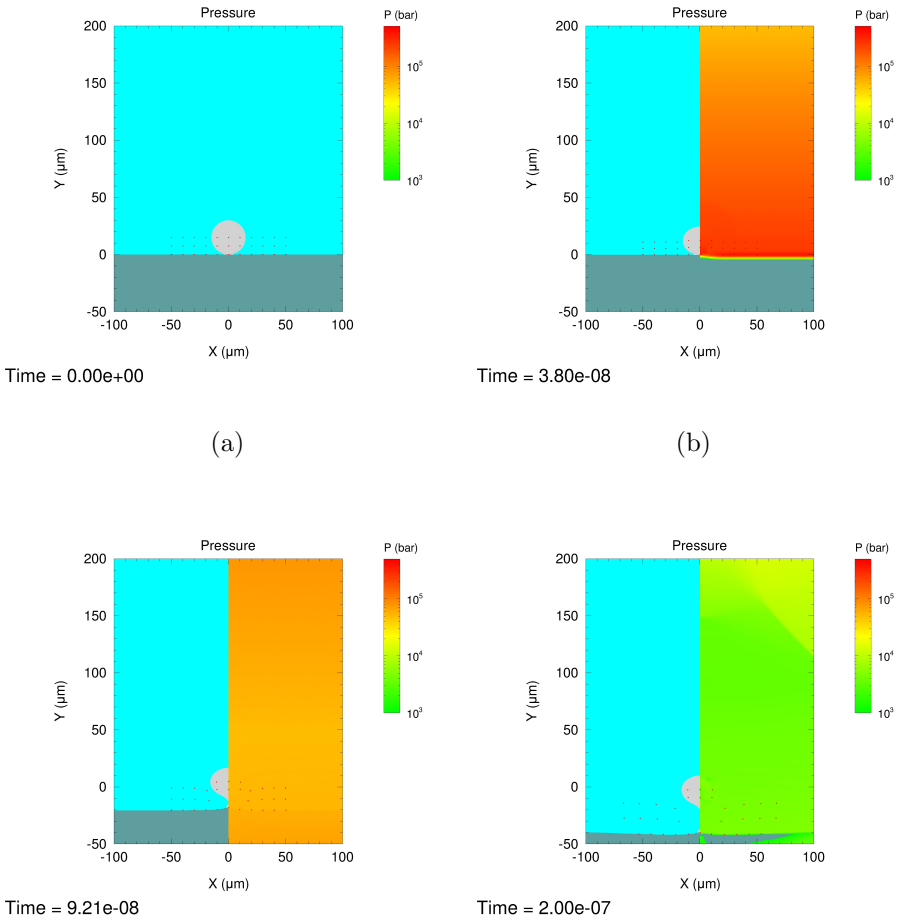

Figure 29: The results of a CTH hydrocode simulation with the aluminum particle in contact with the steel plate - the aluminum particle separates from the plate with the progression of time.

that is undoubtedly present, but it is reasonable to assume a stagnation zone forms which serves as the etaoin shrdlu interface between the detonation products and the plate. The aluminum particle, therefore, does not reach the plate as it is not able to penetrate the stagnation zone as it is well coupled to the gas flow.

Figure 29 parts a-d shows the simulation where the initial position of the aluminum particle was tangential to the steel witness plate.

The aluminum can be seen to deform, but it is not driven into the plate; rather the plate separates from the aluminum particle, and the separation distance increases with time. The aluminum particle does not enhance the plate dent by transferring momentum to the plate. The experimental results that were measured are consistent with the results of this modeling effort.

6.5 Kamlet Analysis

An understanding of the Kamlet equations as told by Dr. Jim Kennedy:

> "I knew Mort Kamlet, but he died before I ever got around to asking him how he had devised the formula for the Kamlet Φ, i.e., $\Phi = NM^{1/2}Q^{1/2}$, as a correlating factor for estimation of explosive performance. So, as I tell my students, I had a séance with Mort and divined this message from him. Two common measures of output of energetic materials are reaction energy and the impulse associated with gas flow. The Q term is the specific energy. The N and M terms provide an estimate of impulse or momentum, which is mass times velocity. N, the number of moles of gas produced per gram of explosive, is a measure of the expansion potential to drive the mass flow, and N may be taken to be proportional to velocity. The mass of the moving material, taken by Kamlet to mean only the gas phase products, is N times M, the molecular weight of the gas. Thus, momentum or impulse corresponds to N^2M. We can take the geometric mean between the two measures, Q and N^2M by multiplying them together and taking their square root, thus $\Phi = NM^{1/2}Q^{1/2}$. Kamlet's papers on this subject dealt only with organic C-H-N-O explosives, and I don't know of any effort to extend them to include aluminized materials. The Kamlet correlations ignore the solid products other than for the energy they may produce. They do not work well for aluminized explosives, which have a high content of solid products, no matter whether the aluminum is reacted or not. Your computations related to particle movement in plate dent-test shots indicate that the fine particles move with the gas flow. So Kamlet's correlation may be recast to reflect these

behaviors in this way, for example. Consider the velocity term in the impulse factor to be represented by N_{gas} and the mass term to be represented by $N_{gas+solid}M_{gas+solid}$. That leads to a modified Φ factor, denoted Φ_R, as $\Phi_R = (N_{gas}N_{gas+solid}M_{gas+solid}Q)^{1/2}$, with chemistry that would effectively provide for aluminum to react first with available oxygen; then hydrogen; then carbon to form CO_2. Since soot would be included in the solid product mass and mole numbers, the quantity $N_{gas+solid}M_{gas+solid}$ may be replaced by ρ_0, since it correspond to the total mass. Then $\Phi_R = (N_{gas}\rho_0 Q)^{1/2}$."

Table 7 shows the various Kamlet values for the CR series of explosives. Unlike the Kamlet analysis performed above where Φ was assumed to be constant, in these comparisons a new Φ was calculated for three specific chemical cases: pure RDX, inert aluminum, and fully reacted aluminum. The binder at 6% by mass in all of the formulations was constant and was not included in the calculations. The results are shown with the various calculated values of Φ and are compared with the experimental values of D and $\sqrt{2E}$. The values of the normalized case using Φ_R agree very well with experimental values for both D and $\sqrt{2E}$ showing that the reduced working fluid resulting from aluminum combustion has a greater impact on the pressure than the increased heat from the aluminum combustion and that the result is a net decrease in pressure, and therefore, a decrease in both D and the $\sqrt{2E}$. This further means that we would expect to see the same values in D and the $\sqrt{2E}$ for the aluminum and talc, which we did.

Table 7: A Kamlet analysis of the CR series of formulations including detonation velocity and Gurney velocity. Once normalized, the values show very good agreement with both rate stick and cylex data. *Kennedy/Rumchik*

Composition wt.%	**Q** cal/g	**N_{gas}** mol/g	**$N_{gas+solid}$** mol/g	**$M_{gas+solid}$** (MW)	**Φ_K**	**Φ_R**	**per Φ_R** √2E, km/s	**norm. Φ_R** √2E, km/s	**K-F*** √2E, km/s	**exp'l#** √2E, km/s	**ρ_0,** tested	**per Φ_R** D, km/s	**norm. Φ_R** D, km/s	**K-J*** D, km/s	**exp'l#** D, km/s	**ρ_0,** tested
RDX, 100	1415	0.0338	0.0405	24.7	6.63	6.92	2.88	2.82	2.82	2.86	1.7	8.12	7.96	7.95	7.83	1.58
RDX/Al, 80/20 (Inert Aluminum/Talc)	1132	0.0297	0.0398	27.3	4.74	6.04	2.76	2.70	2.39	2.58	1.8	8.13	7.97	7.20	7.49	1.75
RDX/Al, 80/20 (Reacted Aluminum)	1217	0.0242	0.0361	30.1	4.24	5.66	2.67	2.61	2.26	2.65	1.8	7.74	7.59	6.70	7.52	1.71

*K-F = Kamlet-Finger correlation, $\sqrt{2}E = 0.887\Phi^{1/2}\rho^{0.4}$ km/s

#K-J = Kamlet-Jacobs correlation, $D = 1.01\ \Phi^{1/2}(1 + 1.30\rho_0)$, km/s

(1) Hypothesize $\Phi_R = [N_{gas}N_{gas+solid}M_{gas+solid}Q]^{1/2}$. This value was used in "per Φ_R" calculations with K-F and K-J correlations.

(2) Normalized calculations were adjusted to match the K-J value for D_{RDX}, that is:

$D = 0.99\ \Phi^{1/2}(1 + 1.30\rho_0)$, km/s, and

$\sqrt{2}E = 0.868\Phi^{1/2}\rho^{0.4}$ km/s

Future work will explore the effect of oxygen balance on the formulation to determine if a more favorable environment could take advantage of the surface area of the nanometer-scale aluminum. Indeed, initial results have shown that, under the certain conditions, nanoenergetic liners can contribute net energy promptly enough to affect the case expansion and/or plate dent depth [56].

The Gurney velocity and plate dent values were not be measured for the initial series of formulations as the current CR formulations provide better charge quality. Therefore, the time and expense of conducting further tests on the initial formulations was not justified.

7 Airblast - Late-Time Energy Release

Only a fraction, on the order of 15%-20%, of the aluminum powder is believed to burn promptly enough to contribute to the blast energy of the explosive [36, 57]. Nanometer-scale aluminum powder has a much greater surface area than standard aluminum powders used in explosive formulations and, therefore, has the potential to burn much more promptly and completely, and thus, contribute more useful energy to the blast output.

Energy is provided to drive the blastwave by two distinct sources. The first is the initial detonation of the explosive. The high pressure gases expand behind the C-J plane in the Taylor wave. The initial detonation will produce water, carbon monoxide, carbon dioxide, nitrogen, and potentially hydrogen. If the aluminum is reacting in the reaction zone, aluminum oxide will also be produced. At this state, the aluminum must compete for oxygen by scavenging any oxygen available or by reacting with water or with carbon dioxide to produce hydrogen or carbon monoxide or by reacting with carbon monoxide to produce aluminum oxide and soot.

The second source is afterburning, which continues to add energy to the expanding gases behind the air shock front as long as the combustible gases blend with atmospheric oxygen and the mixed gases are above the ignition temperature [57]. The shock from the detonation will at first lead the second shock from the afterburn zone. Depending on the conditions behind the first shock, and the pressure of the secondary shock, the secondary shock may catch up to the first shock and increase its pressure. The secondary shock may also remain behind the first shock and result in a two-pulse blast. As the behavior of the secondary shock will depend upon the power density that created it, the behavior should be able to be modified by controlling how the aluminum burns in the afterburn zone of the detonation. Such control

might be accomplished by using a blend of various sizes of aluminum powders.

7.1 Airblast Pressure and Impulse Experiments

A series of airblast tests was conducted with the CR series of explosives in the Dynamics Facility at AFRL/RWME. The charges consisted of right cylinders nominally 2 inch in length with diameters of 1/2 inch, 1 inch, and 2 inches, which correspond to masses of 12 g, 40 g, and 168 g. The end effects of such a cylinder will be less than for a longer aspect ratio. By keeping the length fixed at a nominal 2 inches, the detonation time of all of the charges is ≈ 7 µs. While a sphere with high-precision initiation would achieve nearly symmetric breakout and eliminate end effects, such charges are very time consuming and expensive to produce and, thus, were not practical for this series.

The charges were suspended by a parachute cord in the center of the test chamber and were initiated by a single RP-83 exploding bridgewire detonator positioned in the center of the bottom face of the charge. Static pressures were measured at various distances with standard PCB Piezotronics Model 137A pencil-type probes. The test arena is shown in Figure 30.

All charge sizes were baselined with pressed TNT, and an example of a 1 inch-diameter shot weighing 40 grams is shown in Figure 31. TNT was chosen as a baseline, as it has been commonly used for such purposes in many types of explosive airblast tests and serves as a cross-diameter/mass benchmark. The probes were positioned in the arena to experience similar peak pressures in all of the shots.

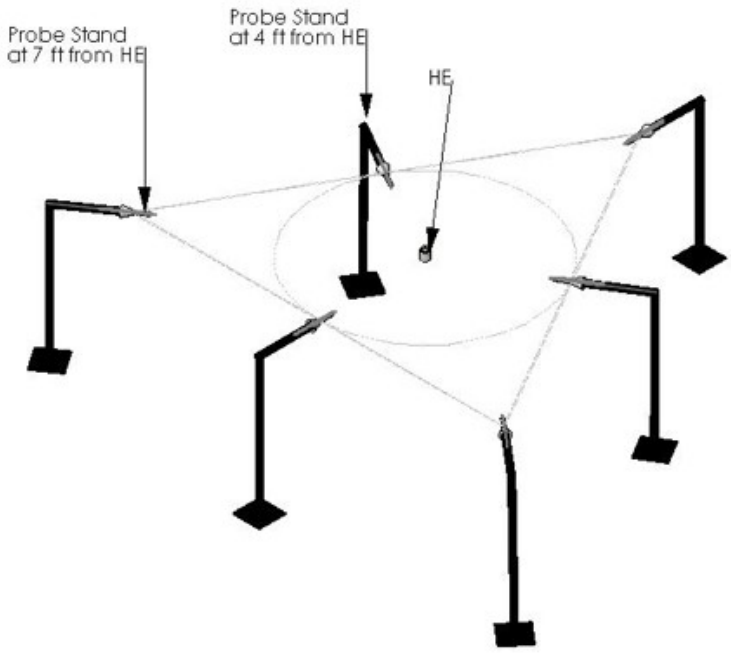

Figure 30: Arena set up for the 168 g blast tests (*Maines*).

7.2 Airblast Pressure and Impulse Results

In the following pages we show the results from the airblast series, which explored 1/2 inch, 1 inch, and 2 inch-diameter charges as described above. The pressure probes were located far enough away from the charge to be outside of the initial fireball volume, in order to be in the far field where blast-wave scaling relations apply. The probes were positioned during each series in such a way as to experience similar pressures - thus, the probes were *not* located at the same radial distance for varying charge sizes.

Beginning with the 1/2 inch charges, the peak pressures at a distance of 1 foot from the charge are shown in Figure 32. The positive impulse is then shown in Figure 33. All of the airblast charts follow the same format. The category marked on the abscissa is the formulation by type of additive (i.e. 50 nm aluminum). The order of the categories on all blast plots is TNT, CR-1, then increasing aluminum particle

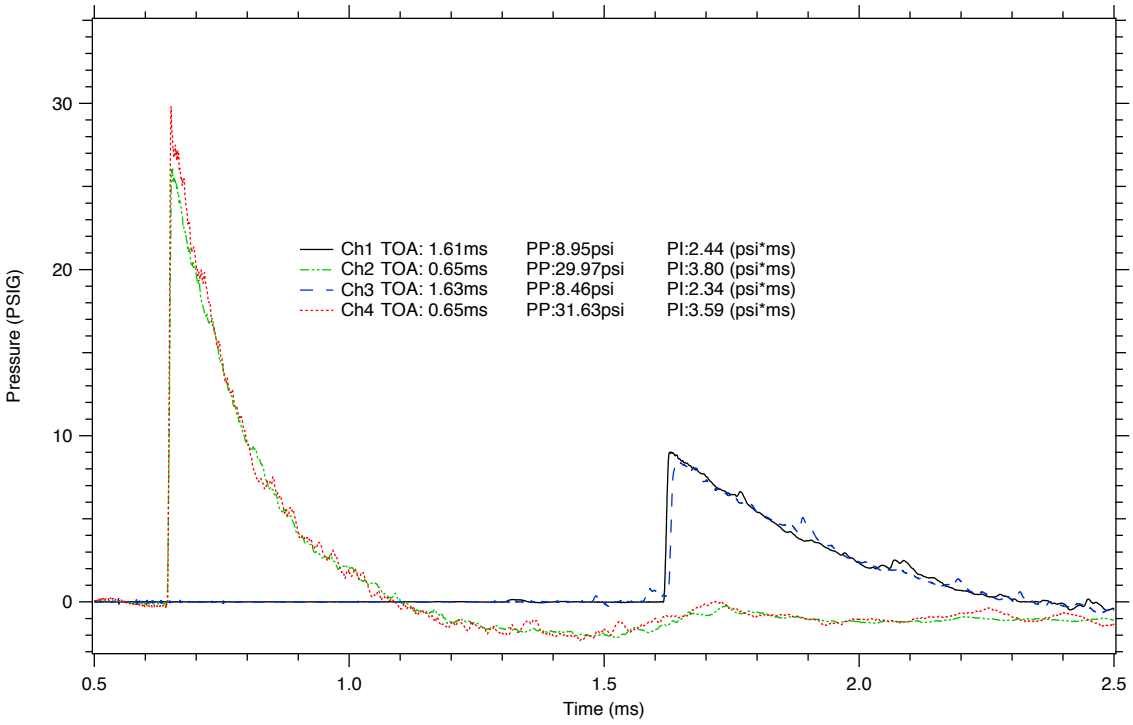

Figure 31: Pressure profiles for a 40 gram TNT blast test.

size starting with 50 nm aluminum, the X-81/talc blend to simulate aluminum oxide content, and then the inert talc. The ordinate is the peak pressure or positive impulse. The open black circles are the individual data points. The data points from all radially symmetrical locations for each of the three tests are shown on the plot.

One will notice some of the formulations have fewer points than others - it is not uncommon to lose a probe signal during the test, and then a data point is missing. Each red square is the mean value, and the blue bar is the experimental value of $+/-2\sigma$ multiplied by the appropriate Student's t-test value for the number of data points in the set. The plots were generated with SigmaPlot, and the calculations of the means and associated uncertainties was done within SigmaPlot using the standard methods [58–60]. The P values of the Student's t-test are reported in the tables associated with each experimental series. If the P value is $\leqslant 0.05$, one can

state with 95% confidence that the samples come from different populations - they are statistically different.

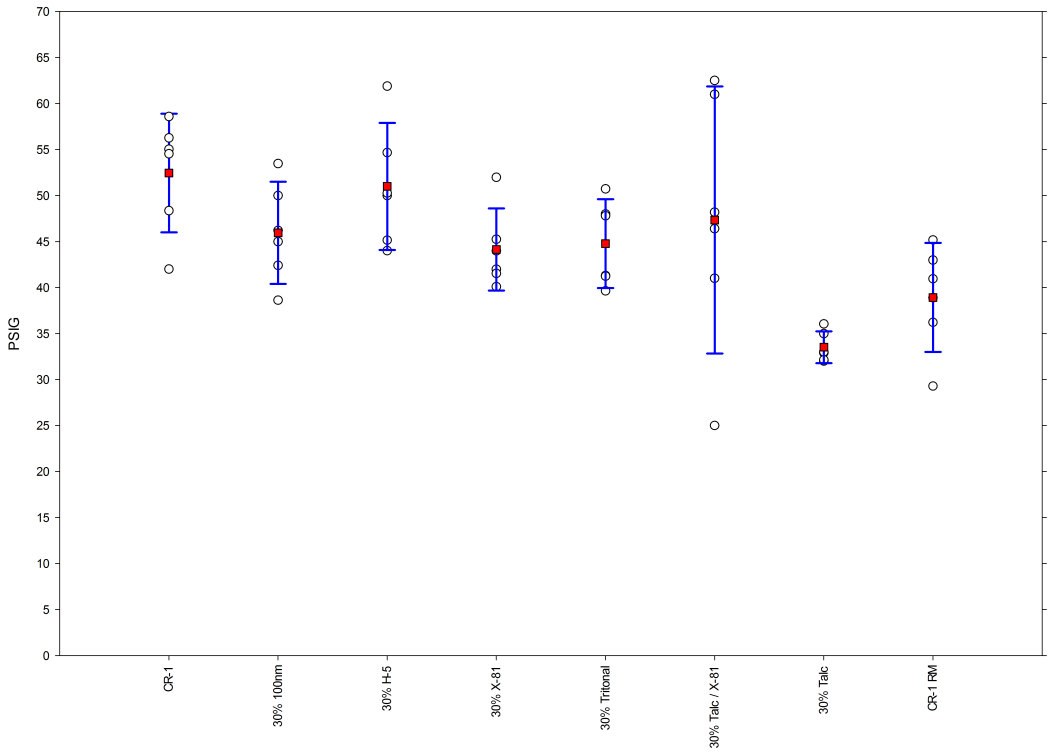

Figure 32: Peak pressure measured at 1 foot for 12 g charges.

Table 8: Student's t-test P values for peak pressure measured at 1 foot.

	CR-1	100 nm	H-5	X-81	Trit	Talc/X-81	Talc	CR-1 RM
CR-1	1.00	0.08	0.70	0.02	0.03	0.43	0.00	0.00
100 nm		1.00	0.17	0.53	0.69	0.82	0.00	0.05
H-5			1.00	0.06	0.09	0.57	0.00	0.01
X-81				1.00	0.81	0.60	0.00	0.10
Trit					1.00	0.68	0.00	0.08
Talc/X-81						1.00	0.04	0.20
Talc							1.00	0.05
CR-1 RM								1.00

The positive impulse as shown for example in Figure 33 is the result of integrating pressure over the time during the positive duration of the blast pressure wave, which

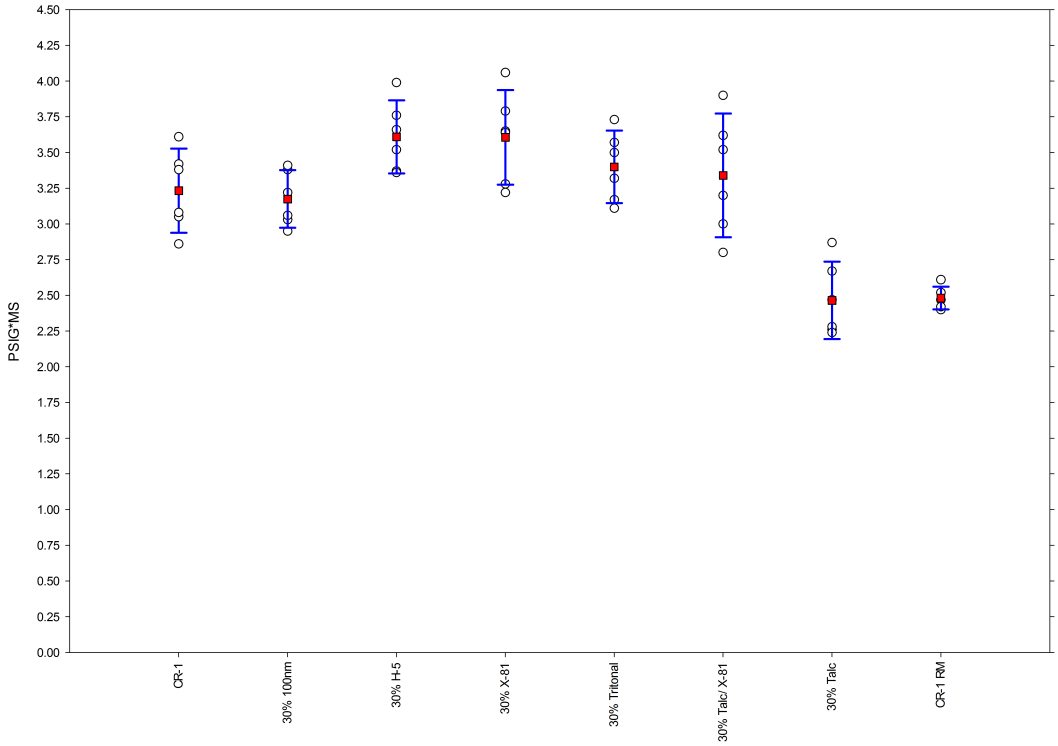

Figure 33: Positive impulse measured at 1 foot for 12 g charges.

is the time from the first positive pressure to that when the pressure crosses the zero baseline. While the data after the zero crossing are real, the small free space in the test facility leads to very early reflections of the pressure waves and, in general, does not allow for clean refection-free measurements to be made throughout the negative phase of the blast wave.

Table 9: Student's t-test P values for positive impulse measured at 1 foot.

	CR-1	100 nm	H-5	X-81	Trit	Talc/X-81	Talc	CR-1 RM
CR-1	1.00	0.00	0.03	0.06	0.30	0.61	0.00	0.00
100 nm		1.00	0.00	0.00	0.00	0.00	0.02	0.00
H-5			1.00	0.98	0.16	0.20	0.00	0.00
X-81				1.00	0.23	0.24	0.00	0.00
Trit					1.00	0.76	0.00	0.00
Talc/X-81						1.00	0.00	0.00
Talc							1.00	0.88
CR-1 RM								1.00

One will notice the range of the uncertainty intervals in relation to the spread of the mean values of each formulation. The differences between formulations are small. Because of the overlapping uncertainty intervals, a Student's t-test was run on each case to determine if the formulations were statistically different from one another.

For instance, looking at Figure 32, one can see that the mean value of the peak pressure produced by the talc charge is below the mean value of the peak pressure of all of the other formulations. If one then looks at Table 8, one can see that the P value for talc vs. all other formulations is < 0.05, therefore, talc indeed produces a lower mean peak pressure than the other formulations. In contrast, if we compare H-5 aluminum to 100 nm aluminum, the P value is 0.17 meaning that H-5 and 100 nm are statistically the same, even though the mean values of the peak pressures differ.

If we then compare 100 nm aluminum and H-5 aluminum values of mean positive impulse in the same case, we see that the P value is 0, thus 100 nm and H-5 are statistically different in impulse in the case of a 12 g charge when measured 1 foot from the charge.

Table 10: Student's t-test P values for peak pressure measured at 2 feet.

	CR-1	100 nm	H-5	X-81	Trit	Talc/X-81	Talc	CR-1 RM
CR-1	1.00	0.14	0.27	0.42	0.08	0.04	0.00	0.00
100 nm		1.00	0.89	0.35	0.72	0.57	0.00	0.01
H-5			1.00	0.53	0.66	0.53	0.00	0.01
X-81				1.00	0.20	0.86	0.00	0.00
Trit					1.00	0.86	0.00	0.01
Talc/X-81						1.00	0.00	0.01
Talc							1.00	0.01
CR-1 RM								1.00

To explore the impact of inert loading, talc was used, as it will not react. It will,

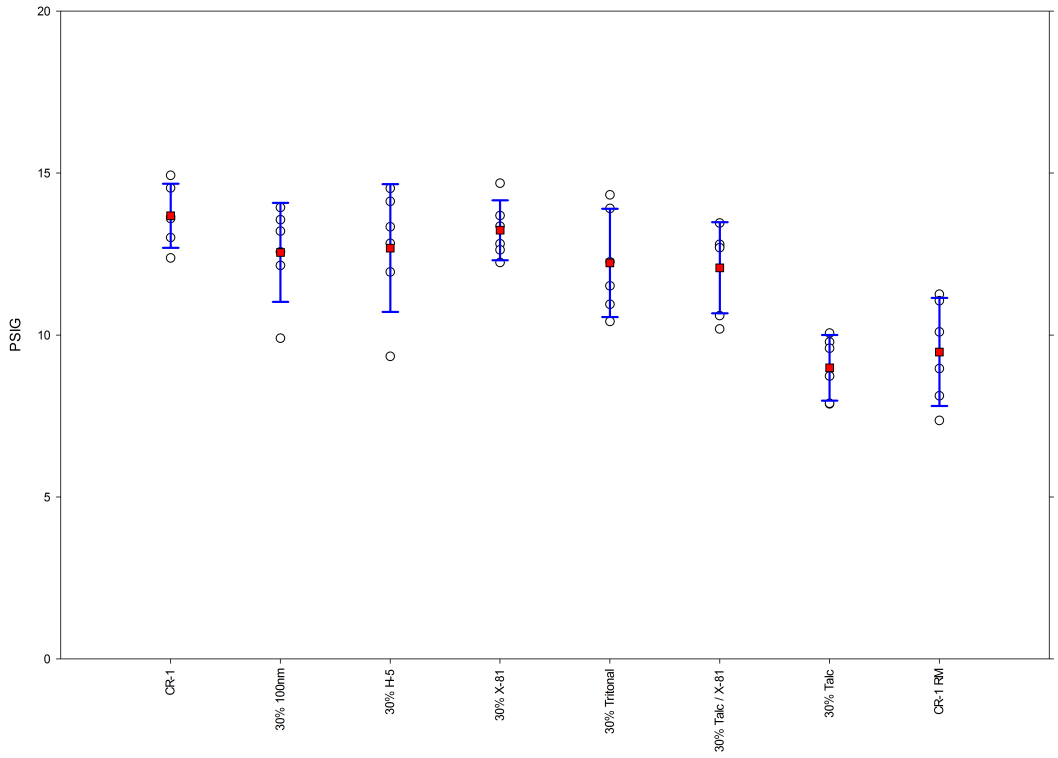

Figure 34: Peak pressure measured at 2 feet for 12 g charges.

however, interact mechanically with the detonation as the wave sweeps through the charge. Therefore, the talc will be heated and put into motion. One anticipates that this will have a negative impact on the blast pressure. We can see that the talc indeed does reduce the mean peak pressure.

The "CR-1 RM" charge consists of the neat formulation but with 30% by mass of the RDX removed. By comparing the mean pressure values of the talc formulation to the reduced mass formulation, we can see that the talc provides a lower value of peak pressure than the reduced mass formulation. By examining the P value, we can see that the mean peak pressure value of the talc is lower, but only a bit lower, than that of the reduced mass charge. The peak pressures at a distance of 2 feet from the charge are shown in Figure 34, and the positive impulse for each formulation is shown in Figure 35.

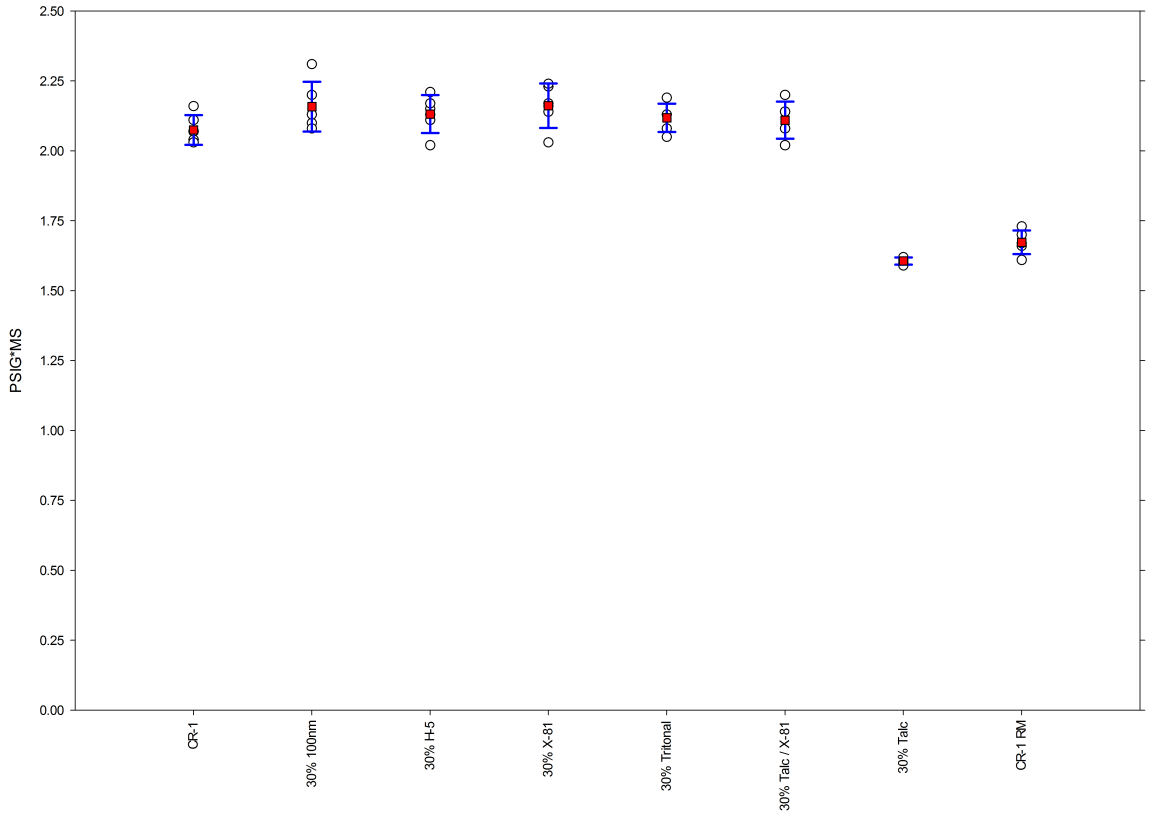

Figure 35: Positive impulse measured at 2 feet for 12 g charges.

Table 11: Student's t-test P values for positive impulse measured at 2 feet.

	CR-1	100 nm	H-5	X-81	Trit	Talc/X-81	Talc	CR-1 RM
CR-1	1.00	0.00	0.12	0.04	0.16	0.31	0.00	0.00
100 nm		1.00	0.00	0.00	0.00	0.00	0.00	0.00
H-5			1.00	0.48	0.69	0.57	0.00	0.00
X-81				1.00	0.26	0.23	0.00	0.00
Trit					1.00	0.80	0.00	0.00
Talc/X-81						1.00	0.00	0.00
Talc							1.00	0.00
CR-1 RM								1.00

To explore the effect of charge diameter on peak pressure and positive impulse as a function of aluminum particle size, a series of blast tests was also run at the two-inch scale. As described above, the length of the charges was held to a nominal 2 inches as the pulse from the detonation wave would have a similar time duration

of $\approx$ 7 µs.

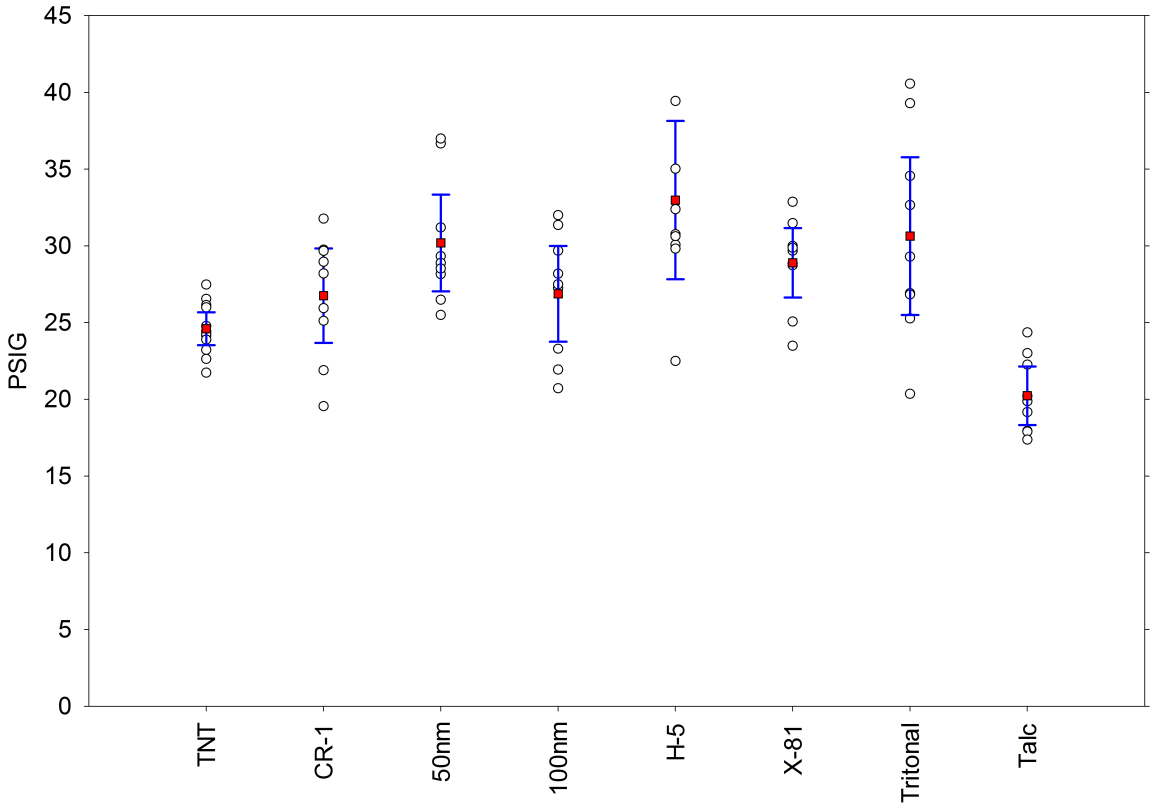

Figure 36: Peak pressure measured at 4 feet for 168 g charges.

Table 12: Student's t-test P values for peak pressure measured at 4 feet.

	TNT	CR-1	50nm	100nm	H5	X-81	Trit	Talc
TNT	1.00	0.11	0.00	0.09	0.00	0.00	0.01	0.00
CR-1		1.00	0.09	0.95	0.03	0.22	0.16	0.00
50nm			1.00	0.10	0.30	0.45	0.87	0.00
100nm				1.00	0.03	0.25	0.17	0.00
H5					1.00	0.11	0.47	0.00
X-81						1.00	0.48	0.00
Trit							1.00	0.00
Talc								1.00

Given the increase in pressure from the larger blast, the probes were moved to 4 feet and 7 feet. As with the 1/2 inch charges, all of the 2 inch charges have 30% by mass additive but for the CR-1 and TNT baseline charges, which have no additives.

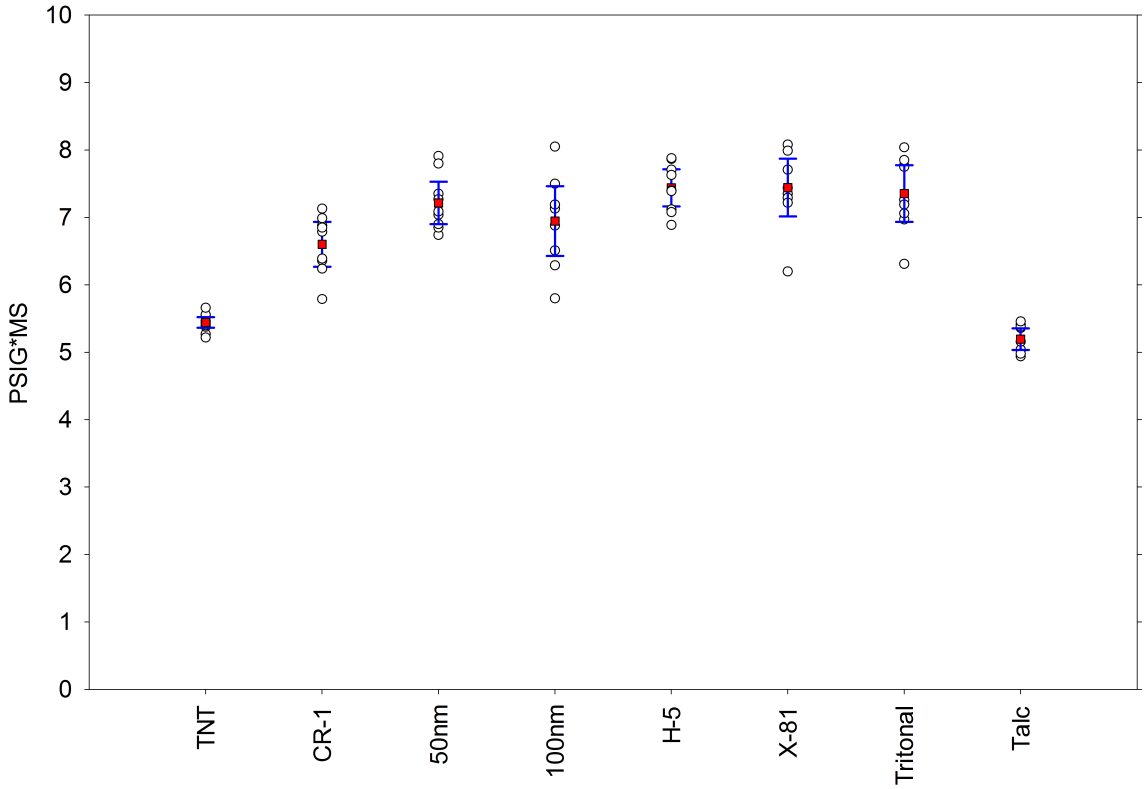

Figure 37: Positive impulse measured at 4 feet for 168 g charges.

Table 13: Student's t-test P values for positive impulse measured at 4 feet.

	TNT	CR-1	50nm	100nm	H5	X-81	Trit	Talc
TNT	1.00	0.00	0.00	0.00	0.00	0.00	0.00	0.00
CR-1		1.00	0.01	0.21	0.00	0.00	0.01	0.00
50nm			1.00	0.32	0.23	0.34	0.55	0.00
100nm				1.00	0.07	0.11	0.18	0.00
H5					1.00	0.99	0.70	0.00
X-81						1.00	0.74	0.00
Trit							1.00	0.00
Talc								1.00

The results of the 2 inch-diameter charges are not much different than those of the 1/2 inch-diameter charges. Neither case displays any strong function of the particle size of aluminum on either the peak pressure or the positive impulse. The inert talc additive was again used in lieu of aluminum to explore the effect of inert

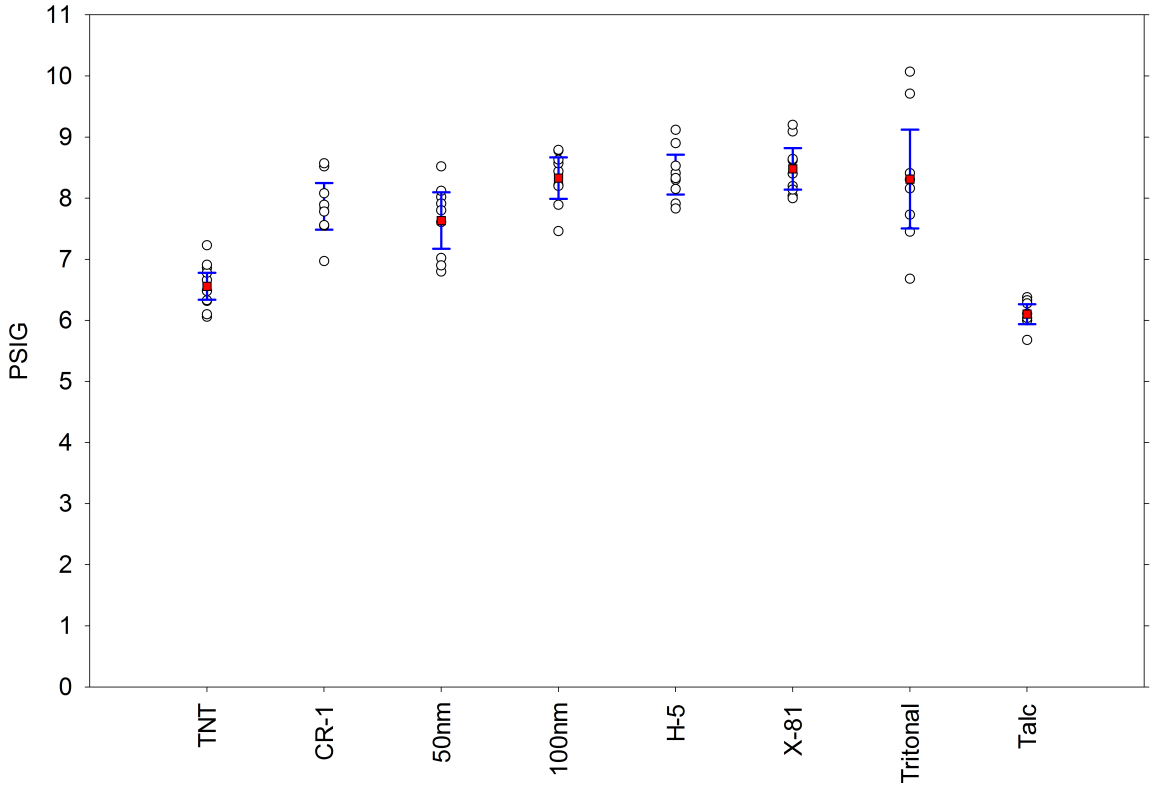

Figure 38: Peak pressure measured at 7 feet for 168 g charges.

Table 14: Student's t-test P values for peak pressure measured at 7 feet.

	TNT	CR-1	50nm	100nm	H5	X-81	Trit	Talc
TNT	1.00	0.00	0.00	0.00	0.00	0.00	0.00	0.00
CR-1		1.00	0.38	0.05	0.03	0.01	0.27	0.00
50nm			1.00	0.01	0.01	0.00	0.11	0.00
100nm				1.00	0.78	0.48	0.97	0.00
H5					1.00	0.65	0.85	0.00
X-81						1.00	0.66	0.00
Trit							1.00	0.00
Talc								1.00

particle loading, and, as with the 1/2 inch-diameter charges, the talc charges showed the lowest performance in both peak pressure and positive impulse. Due to time constraints with the test chamber, a series of reduced-mass charges at the 2 inch scale was not tested.

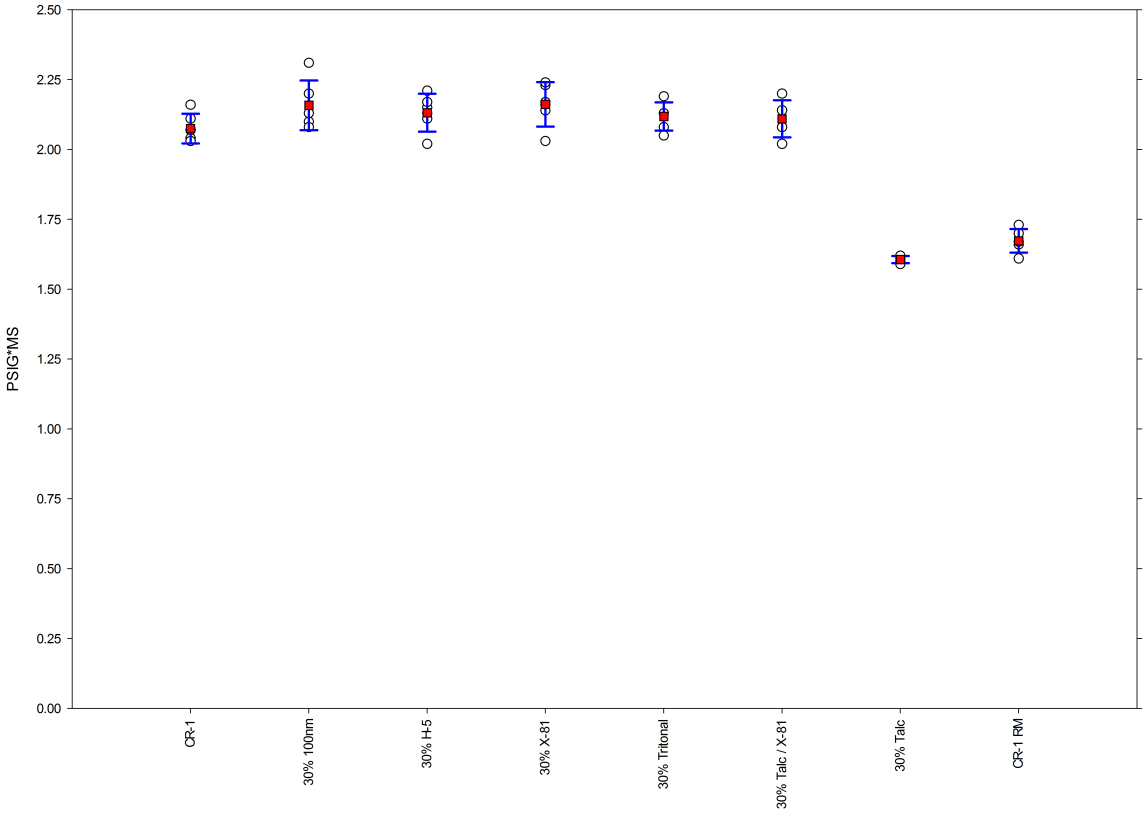

Figure 39: Positive impulse measured at 7 feet for 168 g charges.

Table 15: Student's t-test P values for positive impulse measured at 7 feet.

	TNT	CR-1	50nm	100nm	H5	X-81	Trit	Talc
TNT	1.00	0.90	0.06	0.00	0.00	0.00	0.00	0.00
CR-1		1.00	0.34	0.07	0.05	0.05	0.06	0.00
50nm			1.00	0.24	0.19	0.14	0.19	0.00
100nm				1.00	0.82	0.60	0.79	0.00
H5					1.00	0.76	0.97	0.00
X-81						1.00	0.79	0.00
Trit							1.00	0.00
Talc								1.00

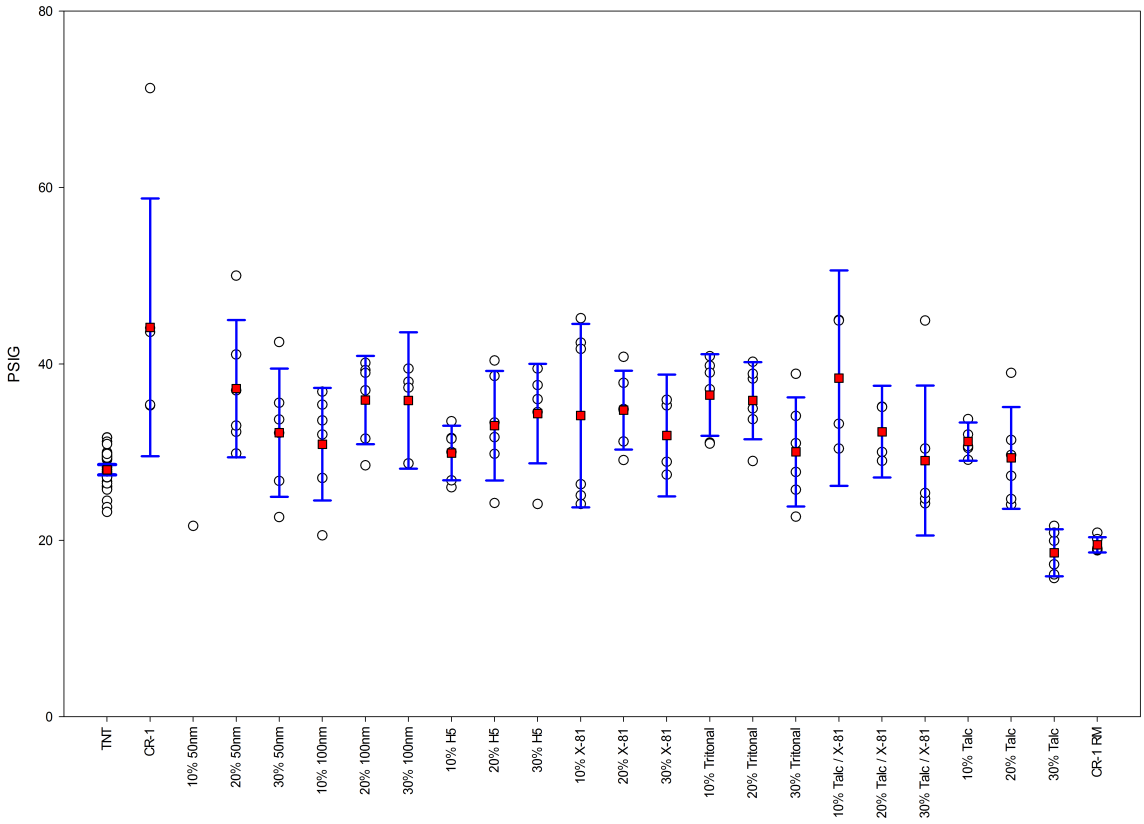

Figure 40: Peak pressure measured at 2.5 feet for 40 g charges.

The most extensive blast-test experiments were carried out using 1 inch-diameter charges with a mass of 40 g. The concentration of the additive was varied, unlike the 1/2 inch and 2 inch charges that all contained 30% by mass of aluminum or talc. The 1 inch charges were prepared with 10%, 20%, and 30% additive. A reduced-mass charge was also fired for the 30% case. The radial probe distance was maintained at 2.5 feet and 4 feet for all of the 1 inch shots. We will look first at the 10%-additive case.

Also, note that there is an extensive set of data for TNT at the 1 inch scale. This was done as an measurement systems analysis (MSA) to get an understanding of the repeatability of the blast data. A total of 28 TNT shots were fired at the 1 inch scale, and due to the large number of data points, one can see that the uncertainty in the

Table 16: Student's t-test P values for peak pressure measured at 2.5 feet with 10% additive.

	TNT	CR-1	50 nm	100 nm	H5	X-81	Trit	X-81/T	Talc
TNT	1.00	0.00	N/A	0.02	0.04	0.00	0.00	0.00	0.00
CR-1		1.00	N/A	0.06	0.03	0.18	0.23	0.48	0.07
50 nm			1.00	N/A	N/A	N/A	N/A	N/A	N/A
100 nm				1.00	0.72	0.51	0.10	0.12	0.92
H5					1.00	0.34	0.01	0.04	0.41
X-81						1.00	0.61	0.49	0.53
Trit							1.00	0.63	0.03
X-81/T								1.00	0.08
Talc									1.00

mean is drastically lower than all of the other data sets due to the large sample size. This may raise the question as to why such a large number of shots were not fired for each and every formulation and configuration. Due to the time and expense involved in making the charges and firing the tests, such repeats are simply not possible, but what the TNT test shows is the setup does allow for repeatable data to be collected. The data are of sufficient quality that any significant differences in the formulations' airblast performance will be discovered.

One will note that in the case of 50 nm aluminum at 10% concentration, only a single data point appears on Figure 40. One shot experienced a trigger problem and no data were captured at all. A cable failure on another shot resulted in lost data as well. Since meaningful statistics can't be obtained from a single data point, "N/A" appears in those positions in Table 16.

Tables 17 and 18 list the P values for 20% and 30% additives, respectively. Unlike the cases of the previous shots at 30% additive, one will note that the talc is not well below the other additives in the 10% case for all of the formulations. As the concentration is increased, the talc is again the clear low performer as in the 30% cases shown in Table 18, where the P values are all 0. The reduced mass also has a P value of 0 in all cases, except for that of the talc, where $P = 0.43$. This means

Table 17: Student's t-test P values for peak pressure measured at 2.5 feet with 20% additive.

	TNT	CR-1	50 nm	100 nm	H5	X-81	Trit	X-81/T	Talc
TNT	1.00	0.00	0.00	0.00	0.00	0.00	0.00	0.00	0.23
CR-1		1.00	0.31	0.20	0.10	0.15	0.19	0.14	0.04
50 nm			1.00	0.73	0.30	0.50	0.70	0.26	0.06
100 nm				1.00	0.37	0.67	0.98	0.23	0.05
H5					1.00	0.57	0.36	0.84	0.29
X-81						1.00	0.67	0.36	0.08
Trit							1.00	0.19	0.04
X-81/T								1.00	0.36
Talc									1.00

Table 18: Student's t-test P values for peak pressure measured at 2.5 feet with 30% additive.

	TNT	CR-1	50 nm	100 nm	H5	X-81	Trit	X-81/T	Talc	RM
TNT	1.00	0.00	0.00	0.00	0.00	0.00	0.08	0.45	0.00	0.00
CR-1		1.00	0.09	0.29	0.14	0.13	0.05	0.04	0.00	0.00
50 nm			1.00	0.39	0.56	0.94	0.57	0.48	0.00	0.00
100 nm				1.00	0.67	0.27	0.14	0.17	0.00	0.00
H5					1.00	0.46	0.21	0.21	0.00	0.00
X-81						1.00	0.60	0.54	0.00	0.00
Trit							1.00	0.82	0.00	0.00
X-81/T								1.00	0.01	0.02
Talc									1.00	0.43
RM										1.00

the talc and reduced mass are giving the same performance in this situation. All of the aluminums are clearly better than talc at the reduced mass meaning they are contributing energy to the blast wave. And while the aluminum is not providing much if any true peak blast pressure enhancement at this small scale, the results do clearly show that RDX can be removed and replaced by less-expensive aluminum to achieve the same or greater peak blast pressure.

The mean positive impulse values are shown in Figure 41 for the 40 g charges as a function of particle size and concentration. Tables 19, 20, and 21 list the P values

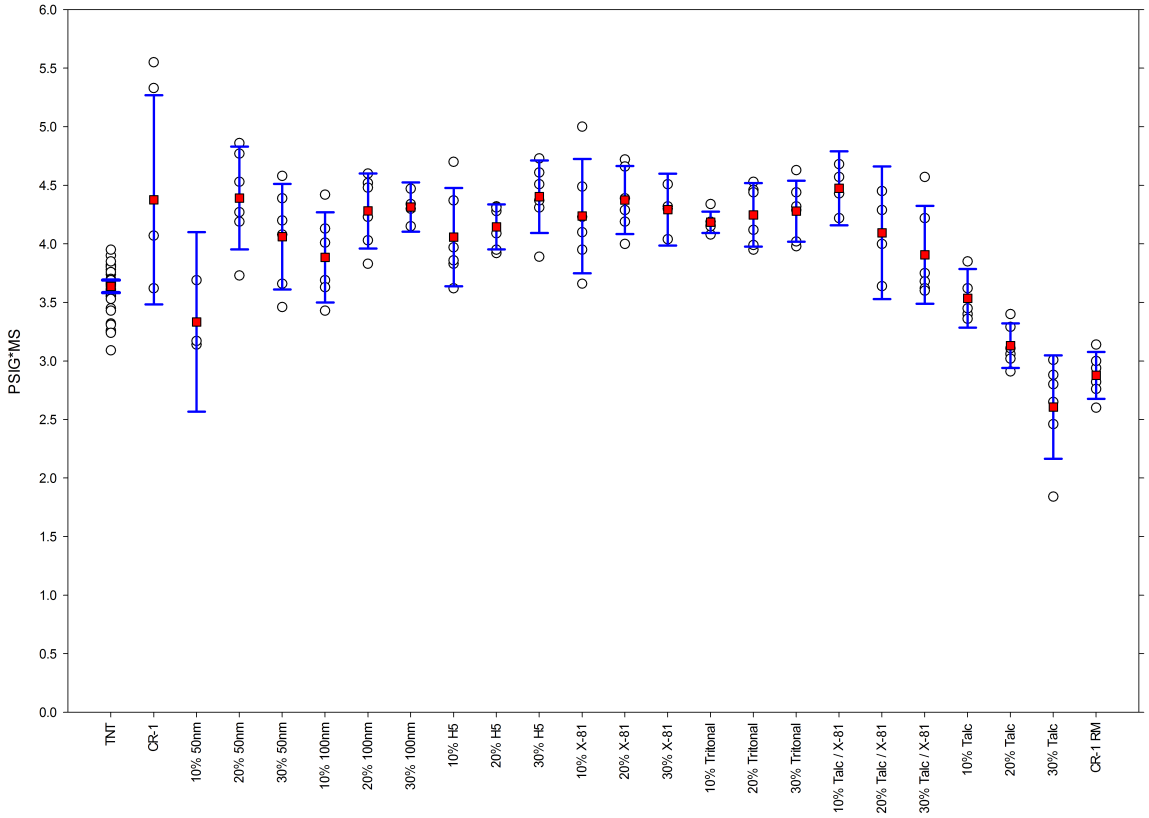

Figure 41: Positive impulse measured at 2.5 feet for 40 g charges.

comparing the mean impulse values for 10%, 20%, and 30% at 2.5 feet respectively.

Table 19: Student's t-test P values for positive impulse measured at 2.5 feet with 10% additive.

	TNT	CR-1	50 nm	100 nm	H5	X-81	Trit	X-81/T	Talc
TNT	1.00	0.00	0.01	0.01	0.00	0.00	0.00	0.00	0.25
CR-1		1.00	0.09	0.22	0.43	0.73	0.60	0.83	0.06
50 nm			1.00	0.06	0.03	0.02	0.00	0.00	0.30
100 nm				1.00	0.45	0.17	0.08	0.02	0.09
H5					1.00	0.49	0.47	0.09	0.09
X-81						1.00	0.79	0.01	0.01
Trit							1.00	0.01	0.00
X-81/T								1.00	0.00
Talc									1.00

Table 20: Student's t-test P values for positive impulse measured at 2.5 feet with 20% additive.

	TNT	CR-1	50 nm	100 nm	H5	X-81	Trit	X-81/T	Talc
TNT	1.00	0.00	0.00	0.00	0.00	0.00	0.00	0.00	0.00
CR-1		1.00	0.97	0.80	0.53	1.00	0.73	0.55	0.01
50 nm			1.00	0.61	0.22	0.94	0.49	0.28	0.00
100 nm				1.00	0.37	0.59	0.84	0.40	0.00
H5					1.00	0.12	0.44	0.77	0.00
X-81						1.00	0.43	0.20	0.00
Trit							1.00	0.45	0.00
X-81/T								1.00	0.00
Talc									1.00

Table 21: Student's t-test P values for positive impulse measured at 2.5 feet with 30% additive.

	TNT	CR-1	50 nm	100 nm	H5	X-81	Trit	X-81/T	Talc	RM
TNT	1.00	0.00	0.00	0.00	0.00	0.00	0.00	0.01	0.00	0.00
CR-1		1.00	0.44	0.89	0.94	0.85	0.79	0.25	0.00	0.00
50 nm			1.00	0.29	0.14	0.35	0.31	0.53	0.00	0.00
100 nm				1.00	0.59	0.85	0.80	0.09	0.00	0.00
H5					1.00	0.53	0.45	0.03	0.00	0.00
X-81						1.00	0.93	0.11	0.00	0.00
Trit							1.00	0.08	0.00	0.00
X-81/T								1.00	0.00	0.00
Talc									1.00	0.18
RM										1.00

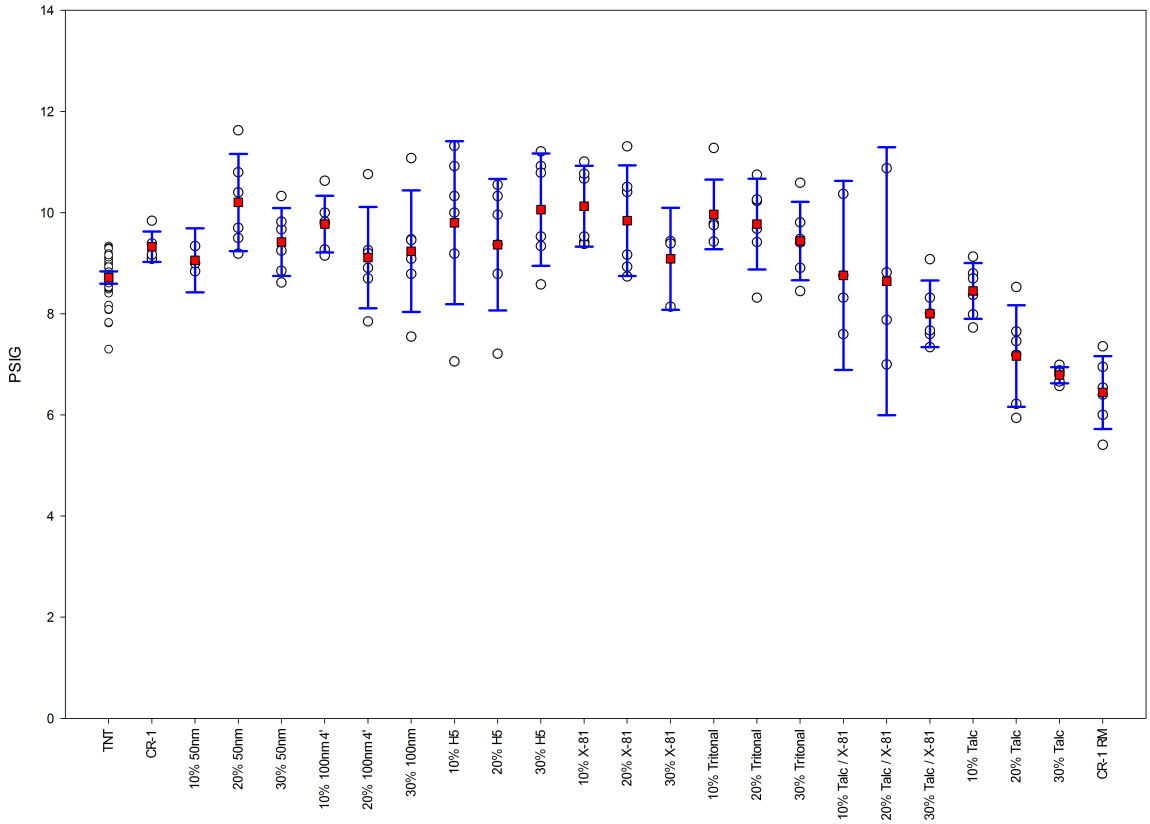

Figure 42: Peak pressure measured at 4 feet for 40 g charges.

As with the peak-pressure values, we see that the talc is the low performer as the concentration increases. There is more of a spread in the impulse data than there is with the peak-pressure data. This is not at all surprising as the impulse is integrating all the positive pulse duration of the blast wave. At the 30% concentration the P value indicates that the reduced mass and talc have the same performance. Both the reduced mass and talc are well below the aluminized formulations in both mean peak pressure and mean positive impulse.

Probes were also placed at 4 feet radially from the charge to explore the pressure and impulse at a later time. Figure 42 shows the mean peak pressures as a function of particle size and concentration at 4 feet for the 40g charges. Tables 22, 23, and 24 show the associated P values.

Table 22: Student's t-test P values for peak pressure measured at 4 feet with 10% additive.

	TNT	CR-1	50 nm	100 nm	H5	X-81	Trit	X-81/T	Talc
TNT	1.00	0.00	0.17	0.00	0.00	0.00	0.00	0.86	0.17
CR-1		1.00	0.21	0.10	0.47	0.04	0.05	0.28	0.01
50 nm			1.00	0.07	0.45	0.06	0.06	0.69	0.11
100 nm				1.00	0.97	0.37	0.59	0.10	0.00
H5					1.00	0.65	0.81	0.29	0.07
X-81						1.00	0.70	0.05	0.00
Trit							1.00	0.07	0.00
X-81/T								1.00	0.58
Talc									1.00

Table 23: Student's t-test P values for peak pressure measured at 4 feet with 20% additive.

	TNT	CR-1	50 nm	100 nm	H5	X-81	Trit	X-81/T	Talc
TNT	1.00	0.00	0.00	0.07	0.01	0.00	0.00	0.81	0.00
CR-1		1.00	0.05	0.61	0.94	0.27	0.25	0.34	0.00
50 nm			1.00	0.07	0.21	0.54	0.42	0.09	0.00
100 nm				1.00	0.70	0.23	0.23	0.58	0.01
H5					1.00	0.49	0.52	0.45	0.01
X-81						1.00	0.90	0.19	0.00
Trit							1.00	0.19	0.00
X-81/T								1.00	0.11
Talc									1.00

Table 24: Student's t-test P values for peak pressure measured at 4 feet with 30% additive.

	TNT	CR-1	50 nm	100 nm	H5	X-81	Trit	X-81/T	Talc	RM
TNT	1.00	0.00	0.00	0.03	0.00	0.11	0.00	0.00	0.00	0.00
CR-1		1.00	0.75	0.86	0.13	0.43	0.73	0.00	0.00	0.00
50 nm			1.00	0.74	0.23	0.44	0.96	0.00	0.00	0.00
100 nm				1.00	0.23	0.82	0.72	0.04	0.00	0.00
H5					1.00	0.14	0.27	0.00	0.00	0.00
X-81						1.00	0.46	0.03	0.00	0.00
Trit							1.00	0.00	0.00	0.00
X-81/T								1.00	0.00	0.00
Talc									1.00	0.26
RM										1.00

We see that TNT and talc are similar when the talc concentration is 10%. The X-81 blend also provides similar results as the talc. The blend is to simulate the chemistry of the nanometer-scale aluminum formulations. The nanometer-scale materials have a higher Al_2O_3 mass fraction due to the larger size of the oxide layer relative to that of the nanometer-scale particle. Similar trends are observed with increasing additive concentrations as were observed at 2.5 feet. The talc is statistically different from all of the other formulations but for the reduced mass case when the additive concentration is 30%.

The mean positive impulse for the 40 g charges as a function of particle size and concentration at 4 feet from the charge is shown in Figure 43.

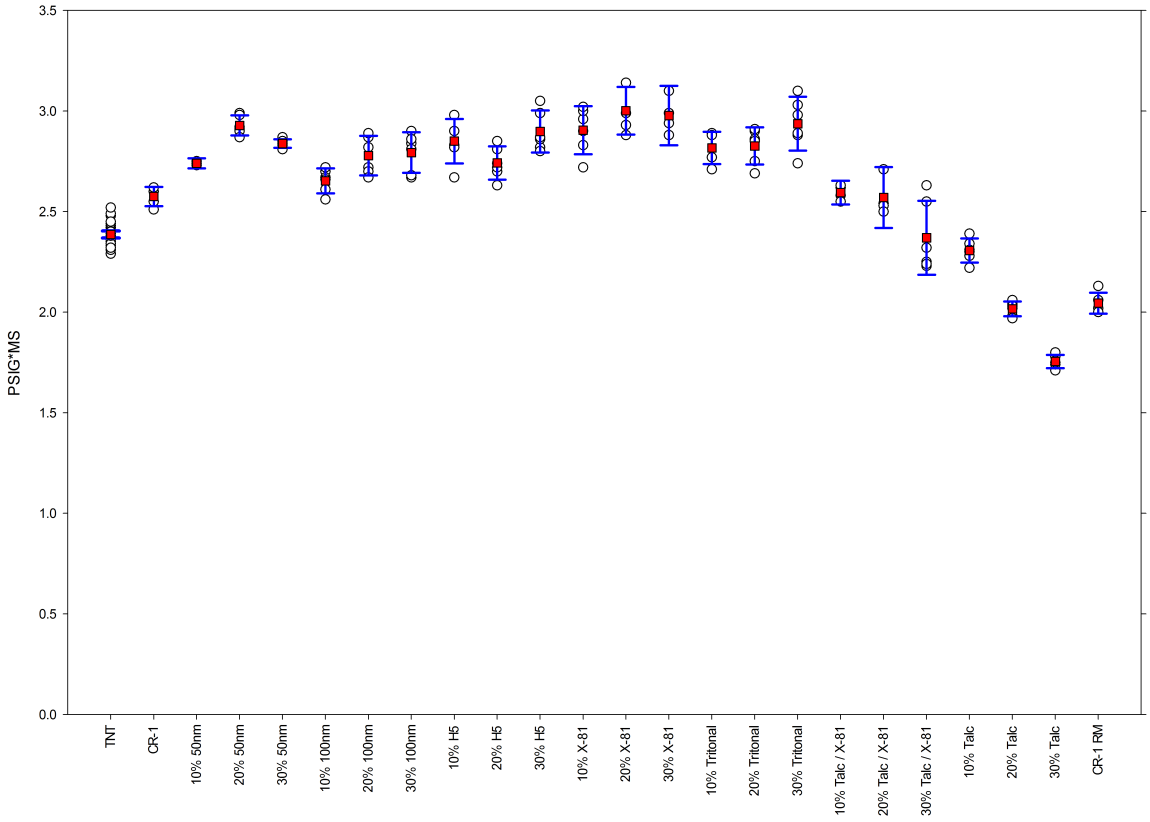

Figure 43: Positive impulse measured at 4 feet for 40 g charges.

The talc is well below all of the formulations for mean positive impulse at a distance of 4 feet and a additive concentration of 30%. The balance of the additives (aluminum) are very similar in performance - none of them significantly outperform the others in either mean peak pressure or mean positive impulse. The P values for peak mean impulse at 4 feet are shown in Tables 25, 26, and 27.

Overall in the blast series, the removal of RDX and replacement with aluminum did maintain or slightly enhance the blast-wave performance in terms of mean peak pressure and mean positive impulse. The P values obtained by using the Student's t-test show which mean values are statistically different from one another. The small

Table 25: Student's t-test P values for positive impulse measured at 4 feet with 10% additive.

	TNT	CR-1	50 nm	100 nm	H5	X-81	Trit	X-81/T	Talc
TNT	1.00	0.00	0.00	0.00	0.00	0.00	0.00	0.00	0.00
CR-1		1.00	0.00	0.03	0.00	0.00	0.00	0.48	0.00
50 nm			1.00	0.05	0.12	0.05	0.14	0.00	0.00
100 nm				1.00	0.00	0.00	0.00	0.12	0.00
H5					1.00	0.41	0.54	0.00	0.00
X-81						1.00	0.00	0.00	0.00
Trit							1.00	0.00	0.00
X-81/T								1.00	0.00
Talc									1.00

Table 26: Student's t-test P values for positive impulse measured at 4 feet with 20% additive.

	TNT	CR-1	50 nm	100 nm	H5	X-81	Trit	X-81/T	Talc
TNT	1.00	0.00	0.00	0.00	0.00	0.00	0.00	0.00	0.00
CR-1		1.00	0.00	0.00	0.00	0.00	0.00	0.91	0.00
50 nm			1.00	0.01	0.00	0.17	0.03	0.00	0.00
100 nm				1.00	0.48	0.00	0.38	0.01	0.00
H5					1.00	0.00	0.11	0.01	0.00
X-81						1.00	0.01	0.00	0.00
Trit							1.00	0.00	0.00
X-81/T								1.00	0.00
Talc									1.00

Table 27: Student's t-test P values for positive impulse measured at 4 feet with 30% additive.

	TNT	CR-1	50 nm	100 nm	H5	X-81	Trit	X-81/T	Talc	RM
TNT	1.00	0.00	0.00	0.00	0.00	0.00	0.00	0.63	0.00	0.00
CR-1		1.00	0.00	0.00	0.00	0.00	0.00	0.02	0.00	0.00
50 nm			1.00	0.29	0.18	0.01	0.09	0.00	0.00	0.00
100 nm				1.00	0.09	0.02	0.05	0.00	0.00	0.00
H5					1.00	0.24	0.57	0.00	0.00	0.00
X-81						1.00	0.60	0.00	0.00	0.00
Trit							1.00	0.00	0.00	0.00
X-81/T								1.00	0.00	0.00
Talc									1.00	0.00
RM										1.00

changes indicated by these tests suggest that using nanometer-scale aluminum to increase blast in small charges with a negative oxygen balance is not worthwhile. There *are* differences between the various aluminums observed both in mean peak pressure and mean positive impulse as shown in the above figures, but these differences are small. Further testing (repeat experiments with more samples etc.) would reduce the uncertainty in the measurements, but such testing is not feasible to split hairs over performance.

7.3 Time Resolved Spectroscopy of Airblast

A technique enabling extensive time-resolved temperature measurements to be made was developed for this work utilizing barium-nitrate-doped charges and emission spectroscopy. This technique serves as a probe of the time scale of the aluminum combustion [61–64]. By using emission spectroscopy, the uncertainty in temperature due to varying emissivities is overcome as the intensities of given emission lines are used to calculate the apparent temperature from the Boltzmann populations using the two-line method, which does not depend on an assumed emissivity contrary to the pyrometry techniques.

The charges were the same CR series formulations used for the rest of this work but contained an additional 1% by mass of barium nitrate, which was finely ground and added to the slurry mix to achieve an even distribution throughout the mixture. Barium nitrate was chosen as it produces very strong emission lines in the visible region at the expected temperatures, and it is chemically compatible with the formulations used.

The experimental set up consisted of a 1 inch x 1 inch 22 g CR series pellet with an RP-80 detonator attached to one end and the opposite end placed through a 1 inch-diameter hole in the center of a 12 inch x 12 inch piece of cardboard. This arrangement shields the fiberoptic pick-up from light generated by the detonator on the opposite side of the cardboard. The assembly was then placed on a table and a stand holding the fiberoptic cable and a collimating lens was placed a few feet in front of the charge. A laser was fed through the fiber optic cable and lens and used to align the lens with the charge maximizing the light that was gathered. All shots were fired in triplicate, and it was shown that nanometer-scale aluminum does burn more promptly, and the fireball does indeed reach higher temperatures, as shown in Figure 44.

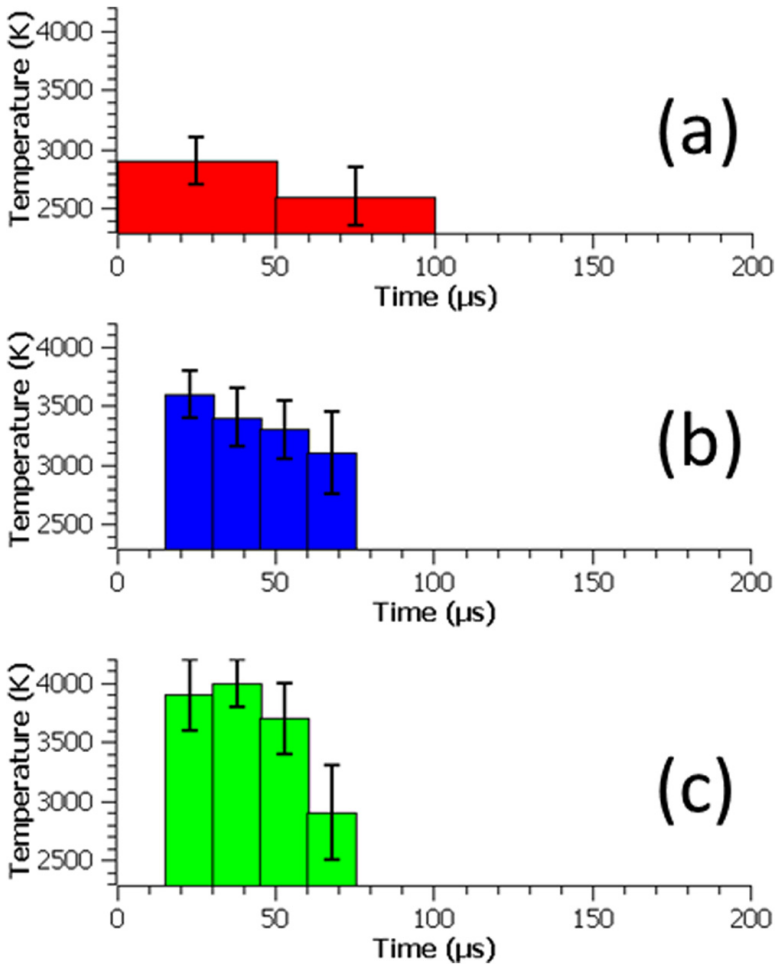

Figure 44: Apparent temperatures obtained from the atomic Ba emissions exhibited by the charges doped with 1 wt. % barium nitrate. (a) neat, (b) with 20% micrometer-scale aluminum particles, and (c) with 20% nanometer-scale aluminum. *Reprinted with permission from the American Institute of Physics* [62]

The broadband emissions are also vastly different for the cases of neat, micrometer-scale aluminum, and nanometer-scale aluminum charges, as shown in Figure 45. While both sizes of aluminum do combust in the afterburn phase, the nanometer-scale aluminum is significantly brighter promptly and then dims quickly, being almost dark after $\approx$ 2.5 ms. The micrometer-scale aluminum is not as bright as the nanometer-scale aluminum and continues to have a substantial broadband emission up to $\approx$ 10 ms.

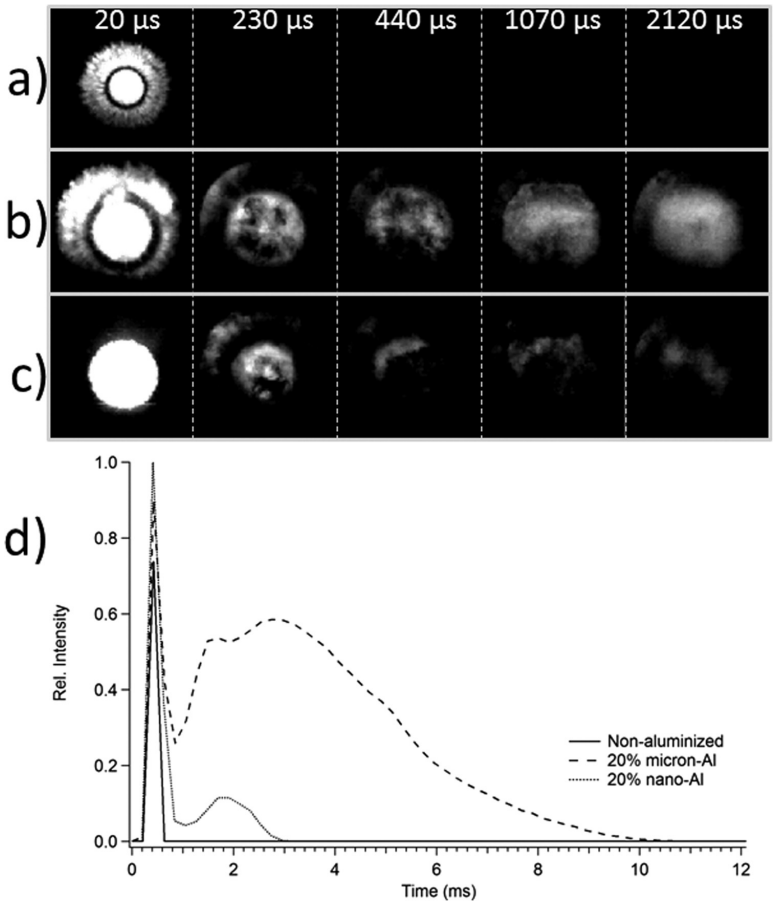

Figure 45: Time dependence on the broadband emissions (a) neat, (b) with 20% micrometer-scale aluminum particles, and (c) with 20% nanometer-scale aluminum, and (d) the relative intensity. *Reprinted with permission from the American Institute of Physics* [62]

In the case of the 1 inch-diameter charges measured, the nanometer-scale aluminum has completed burning at approximately the same time the blast wave reaches the walls of the test chamber while the micrometer-scale aluminum is burning for an additional 6-8 ms. Since no statistical difference was observed in the blast-pressure measurements for the two aluminum classes, the very-late-time combustion of the micrometer-scale aluminum is not prompt enough to couple the heat released to the blast wave in the case of the small charges tested. The luminescent cloud of burning aluminum expands to a volume of $\approx$ 1000-2000 initial volumes and does not con-

tinue to expand further with the shock wave. The burning of the nanometer-scale aluminum exhibits similar behavior and the energy released after $\approx$ 1 ms is not prompt enough to couple the released energy to the blast wave.

The spectroscopic measurements are explored in more detail in the collection of the four journal articles in Appendix B of this document. Further research is warranted to better understand the combustion of aluminum and how it drives the blast wave. This is planned by Lewis and Rumchik. They intend to explore the effect of oxygen balance and determine how the changing chemistry impacts the temperature and blast performance of small-scale charges as a function of aluminum particle size and/or mixtures of aluminum particle sizes.

8 Conclusion

Aluminum powder added to an explosive formulation is known to influence the performance in the areas of detonation velocity, metal acceleration, and airblast. This work served as a careful and diligent probing of three main time regimes of detonation and found that for small-scale charges with a negative oxygen balance, adding nanometer-scale aluminum, in lieu of standard micrometer-scale aluminum, does not enhance performance. The CR series of explosives was developed to facilitate the production of small scale charges with uniform and repeatable densities. The CR formulations proved effective for all of the tests conducted for this research.

Two series of 1/2 inch-diameter rate sticks were run to explore the effect of ρ_0 on the detonation velocity. The velocities measured at low ρ_0 and high ρ_0 allowed $\frac{dD}{d\rho_0}$ to be calculated for each formulation, thus, permitting a direct comparison of D to be made at a common density.

The traditional cylinder expansion test used to measure metal acceleration was scaled down to save material and facilitate testing, and an MSA was conducted to prove the utility of the smaller-size test. Additionally, a method and tooling was developed to directly press load the small copper cylinders used for the test to prevent jetting and early case rupture caused by the interfaces in a tube loaded with discrete pellets. PDV diagnostics were employed to measure the velocity of the cylinder wall to obtain the maximum resolution possible.

Extensive airblast measurements were made with charges 1/2 inch, 1 inch, and 2 inch in diameter at 20% mass concentration of additive with additional tests for the 1 inch charges conducted at 10% and 30% additive. The measurements were quasi-free-field. A spectroscopic technique was developed for this work to measure the fireball temperature as a function of time to track the aluminum combustion.

Additional late-time shots were fired at the 1 inch scale and 20% mass concentrations to make the time-resolved temperature measurements on the formulations.

The key findings are presented in Table 28 in terms of time scale and net exothermic contribution as a function of aluminum powder scale. Both nanometer-scale and micrometer-scale aluminums do contribute energy to the airblast, but the nanometer-scale aluminum burns more promptly and yields a peak temperature of $\approx$ 4000 K compared to $\approx$ 3600 K measured for micrometer-scale aluminum and $\approx$ 2900 K for the neat formulation.

These observations warrant future work to further explore the dynamics of aluminum reaction in the afterburn zone, and a series of spectroscopy experiments are planned utilizing a new digital streak camera as the detector for the spectrometer. This will give two orders of magnitude improvement in the temporal resolution of the spectroscopic data allowing for more insight as to when the nanometer-scale aluminum begins to react and peak.

The nanometer-scale aluminum, micrometer-scale aluminum, and talc yielded similar results in the early-time and mid-time regimes. The neat formulation had the greatest value of detonation velocity and Gurney velocity. Thus, the aluminum served as an inert heat sink as did the talc on these time scales.

Table 28: Reactivity of aluminum as a function of particle size and time.

Timescale	Nano Exothermic	Micron Exothermic	Test
$\leqslant$1 µs	No	No	Detonation Velocity
1-10 µs	No	No	Gurney Energy
10 µs-3 ms	Strong and Prompt	Slow	Spectroscopy and Blast
$\geqslant$3 ms	No (consumed)	Slow	Spectroscopy and Blast

Further experiments are likely to be conducted with a formulation having a favorable oxygen balance as well as the possibility of using fluorine as an oxidizer for

the aluminum. Issues of initiation characteristics were not addressed in this work, and an exploration of those characteristics as a function of nanometer-scale particle loading and chemical composition would be a worthwhile endeavor.

Distribution A. Approved for public release, distribution unlimited (96TW-2015-0226)

Bibliography

[1] Queenie S. M. Kwok, Robert C. Fouchard et al. Characterization of Aluminum Nanopowder Compositions. *Propellants, Explosives, Pyrotechnics*, 2002.

[2] P. J. Miller, C. D. Bedford, and J. J. Davis. Effect of Metal Particle Size on the Detonation Properties of Various Metallized Explosives. In *the Proceedings of the 11th Symposium on Detonation, Snowmass Village Colorado*, 1998.

[3] Christelle Collet, Michael Dervaux, et. al. Influence of Nanoparticules in Energetic Compositions. In *Proceedings of the 13th International Detonation Symposium*, 2006.

[4] Norbert Eisenreich et. al. Burn Rate Models for Gun Propellants. *Propellants, Explosives, Pyrotechnics*, 27, 2002.

[5] Makoto Kohga and Yutaka Hagihara. Burning Behavior of Composite Propellant Containing Fine Porous Ammonium Perchlorate. *Propellants, Explosives, Pyrotechnics*, 23, 1998.

[6] Peter Ostrowski, Magdy Bichay, Todd Allen, V. E. Sanders, and S. F. Son. Recent Accomplishments in MIC Primer Development at NSWC/Indian Head. In *AIAA Paper 2005-3514*, 2005.

[7] J. W. Mordosky, B. Q. Zhang, and K. Kuo. Spray Combustion of Gelled RP-1 Propellants Containing Nano-Sized Aluminum Particles in Rocket Engine Conditions. In *37th AIAA/ASME/SAE/ASEE Joint Propulsion Conference and Exhibit*, 2001.

[8] L. Meda, G. Marra, and L. Galfetti. Nano-composites for Rocket Solid Propellants. *Composites Science and Technology*, 65:769–773, 2005.

[9] Gennady V. Ivanov and Frederick Tepper. Activated Aluminum as a Stored Energy Source for Propellants. In *Fourth International Symposium on Special Topics in Chemical Propulsion, Challenges in Propellants and Combustion 100 Years after Nobel*, Stockholm, Sweden, May 1996.

[10] B. Baschung et. al. Combustion Phenomena of a Solid Propellant Based on Aluminum Powder. In *5th International Symposium on Special Topics in Chemical Propulsion*, Stresa, Italy, June 2000.

[11] Jing Ping Lu, Helen E. Dorsett, Mark Franson, and Matthew Cliff. Near-field Performance Evaluations of Alex Effect in Metallised Explosives. Technical Report DSTO-TR-1542, Australian Government Department of Defence Defence Science and Technology Organisation, 2003.

[12] Patrick Brousseau et. al. Detonation Properties of Explosives Containing Nanometric Aluminum Powder. In *Proceedings of the 12th International Detonation Symposium*, 2002.

[13] Keith Gonthier. AFRL Summer Posting Technical Report. August 2005.

[14] Keith A. Gonthier. Chapman-Jouget (CJ) Analysis of Aluminum-RDX Explosive. Personal communication, October 2003.

[15] David L. Frost, Samuel Goroshin, et. al. Effect of Scale on the Blast Wave from a Metalized Explosive. In *Proceedings of the 13th International Detonation Symposium*, 2006.

[16] V.M. Boiko and S.V. Poplavski. Self-ignition and Ignition of Aluminum Powders in Shock Waves. *Shock Waves*, 11, 2002.

[17] Patrick Brousseau and C. John Anderson. Nanometric Aluminum in Explosives. *Propellants, Explosives, Pyrotechnics*, 2002.

[18] Josef Kohler and Rudolf Meyer. *Explosives*. VCH Verlagsgesellschaft mbH, 1993.

[19] Jacqueline Akhavan. *The Chemisty of Explosives*. The Royal Society of Chemistry, Cambridge, UK, 1998.

[20] Jonas A. Zukas and William P. Walters. *Explosive Effects and Applications*. Springer-Verlag New York, Inc., New York, New York 10010, 1998.

[21] Richard Dick. Rankine-Hugoniot Equations. Unpublished shock physics notes.

[22] Paul Cooper. *Explosives Engineering*. VCH Publishers, Inc., New York, New York 10001, 1996.

[23] Per-Anders Persson, Roger Holmberg, Jaimin Lee. *Rock Blasting and Explosives Engineering*. CRC Press, Boca Raton, FL, 1994.

[24] Wildon Ficket and William C. Davis. *Detonation Theory and Experiment*. Dover, Mineola, NY, 1979;2000.

[25] Ya. B. Zel'dovich and Yu. P. Raizer. *Physics of Shock Waves and High-Temperature Hydrodyanmic Phenomena*. Dover, Mineola, NY, 1966;2002.

[26] Stephen R. Turns. *An Introduction to Combustion: Concepts and Applications*. McGraw-Hill, NYC, NY, 2000.

[27] Roger Cheret. *Detonation of Condensed Explosives*. Springer-Verlag New York, Inc., New York, New York, 1992.

[28] M. A. Meyers. *Dynamic Behavior of Materials*. John Wiley & Sons, Inc., New York, New York, 1994.

[29] Keith A. Gonthier. Multiphase Detonation of Metalized Solid Explosive. AFRL summer posting, April 2006.

[30] D. S. Stewart. Towards the Miniaturization of Explosive Technology. *Shock Waves*, 11, 2002.

[31] Russell E. Duff and Edwin Houston. Measurement of the Chapman-Jouget Pressure and Reaction Zone Length in a Detonating High Explosive. *The Journal of Chemical Physics*, 23(7), July 1955.

[32] Naminosuke Kubota. *Propellants and Explosives*. WILEY-VCH GmbH, Weinheim, Germany, 2002.

[33] Keith A. Gonthier and Chad G. Rumchik. Theory and Analysis of Non-Ideal Detonation for RDX/Dilute Metal Mixtures. In *Proceedings of the 13th International Detonation Symposium*, 2006.

[34] R.W. Gurney. The Initial Velocities of Fragments from Bombs, Shells, and Grenades. *Army Ballistic Research Laboratory Report BRL 405*, 1943.

[35] J. E. Kennedy. Gurney Energy of Explosives: Estimation of the Velocity and Impulse Imparted to Driven Metal. Technical Report SC-RR-70-790, Sandia Laboratories, 1970.

[36] C. G. Rumchik, M. W. Crochet and K. A. Gonthier. The Effect of Aluminum Grain Size and Shape on Airblast Produced by Small RDX-Based Charges. In *JANNAF 41st CS/29th APS/23rd PSHS Joint Meeting*, 2007.

[37] Richard G. Ames, Jason T. Drotar, et. al. Quantitative Distinction Between Detonation and Afterburn Energy Deposition Using Pressure-Time Histories in Enclosed Explosions. In *Proceedings of the 13th International Detonation Symposium*, 2006.

[38] W. E. Baker. *Explosions in Air*. University of Austin Texas Press, Austin and London, 1973.

[39] Gilbert F. Kinney and Kenneth J. Graham. *Explosive Shocks In Air*. Springer-Verlag New York Inc., New York, New York 10001, 1985.

[40] Marcia A. Cooper, Michael J. Kaneshige, et. al. Methods for Evaluating Aluminized RDX Explosives. In *Proceedings of the 13th International Detonation Symposium*, 2006.

[41] Patrick Walter. Personal communication.

[42] V. Rosenband. Thermo-mechanical Aspects of the Hetrogeneous Ignition of Metals. *Combustion and Flame*, 137, 2004.

[43] Valery I. Levitas, Michelle L. Pantoya, and Steven Dean. Melt Dispersion Mechnisim for Fast Reaction of Aluminum Nano and Micron-scale Particles: Flame Propagation and SEM Studies. *Combustion and Flame*, 161, 2014.

[44] Richard Dick. Personal communication.

[45] Yuki Horie. Personal communication.

[46] Keith Gonthier. Personal communicaiton.

[47] Alan C. Hindmarsh. *DLSODE Reference Manual*. Lawrence Livermore National Laboratory, Livermore, CA 94550.

[48] Kakac and Yener. *Heat Conduction - Third Edition*. Taylor & Francis, 1992.

[49] K. Park et al. Size-Resolved Kinetic Masurements of Aluminum Naoparticle Oxidation with Single Particle Mass Spectrometry. *J. Phys. Chem. B*, 2005.

[50] Charles L. Mader. *Numerical Modeling of Explosives and Propellants - Second Edition*. CRC Press, 1998.

[51] C. Michael Lindsay, George C. Butler, Chad G. Rumchik, et al. Increasing the Utility of the Copper Cylinder Expansion Test. *Propellants, Explosives, Pyrotechnics*, 35(5), 2010.

[52] Chad Rumchik, Rachel Nep, and George Butler. The Miniaturization and Reproducibility of the Cylinder Expansion Test. *American Physical Society, 17th Biennial International Conference on Shock Compression of Condensed Matter*, 2011.

[53] O. T. Strand and et al. Compact System for High-Speed Velocimetry Using Heterodyne Techniques. *Rev. Sci. Instr.*, 2006.

[54] C. Michael Lindsay. Unpublished personal communicaiton.

[55] James Kennedy. Personal communicaiton.

[56] C. M. Lindsay et. al. Impact of Liners on the Casing Wall Early-Time Expansion: Reactive Versus Non-Reactive Liner Materials. In *Proceedings of the Joint Army Navy NASA Air Force, 37th Propellant and Explosives Development and Characterization Meeting*, April 2012.

[57] C. E. Needham. *Blast Waves*. Springer-Verlag New York Inc., 2010.

[58] Systat staff. *SigmaPlot 10.0.1 User's Manual*. Systat, 2007.

[59] Daniel Zwillinger, editor. *CRC Standard Mathematical Tables and Formulae 30th Edition*. CRC Press, 1996.

[60] Hugh W. Coleman and W. Glenn Steele. *Experimentation and Uncertainty Analysis for Engineers*. John Wiley & Sons, Inc., 2nd edition, 1999.

[61] W.K. Lewis and C. G. Rumchik. Measurement of Apparent Temperature in Post-Detonation Fireballs Using Atomic Emission Spectroscpy. *Journal of Applied Physics*, 2009.

[62] W. K. Lewis, C. G. Rumchik, and et. al. Time-Resolved Spectroscopic Studies of Aluminized Explosives: Chemical Dynamics and Apparent Temperatures. *Journal of Applied Physics*, 2012.

[63] W. K. Lewis, C. G. Rumchik, and M. J. Smith. Emission Spectroscopy of the Interior of Optically Dense Post-Detonation Fireballs. *Journal of Applied Physics*, 2013.

[64] W. K. Lewis, C. G. Rumchik, and et al. Comparison of Post-Detonation Combustion in Explosives Incorporating Alumnium Nanoparticles: Influence of the Passivation Layer. *Journal of Applied Physics*, 2013.

A

Cylinder Expansion Paper

THE MINIATURIZATION AND REPRODUCIBILITY OF THE CYLINDER EXPANSION TEST

C. G. Rumchik, R. Nep, G.C. Butler, B. Breaux, and C. M. Lindsay

Air Force Research Laboratory, Munitions Directorate, Eglin AFB, FL 32542

Abstract. The cylinder test (aka cylinder expansion or Cylex test) is a standard way to measure the Gurney velocity and determine the JWL coefficients of an explosive and has been utilized by the explosives community for many years. More recently, early time shock information has been found to be useful in examining the early pressure-time history during the expansion of the cylinder. Work in the area of nanoenergetics has prompted Air Force researchers to develop a miniaturized version of the Cylex test, for materials with a sufficiently small critical diameter, to reduce the cost and quantity of material required for the test. This paper discusses the development of a half-inch diameter version of the Cylex test. A measurement systems analysis of the new miniaturized and the standard one-inch test has been performed using the liquid explosive PLX (nitromethane sensitized with ethylene diamine). The resulting velocity and displacement profiles obtained from the streak records were compared to Photo Doppler Velocimetry (PDV) measurements as well as CTH hydrocode simulations. Measurements of the Gurney value for both diameter tests were in agreement and yielded a similar level of variability of 1%-4%.

Keywords: Cylex, Cylinder Expansion Test, Photo Doppler Velocimetry PDV, hydrocode, CTH
PACS: 62.50.Ef, 82.40.Fp

INTRODUCTION

The cylinder test (herein called the Cylex test) is a method that measures an explosive's ability to accelerate metal and is the standard means for determining the Gurney velocity [1-2] and coefficients for the Jones-Wilkins-Lee (JWL) equation of state [3-4] for an explosive. The Gurney equations are a set of mathematical formulas used in explosives engineering to determine the capability of a detonating explosive to accelerate a surrounding layer of inert material. The Gurney velocity can then be used to estimate fragment velocities, for example. The JWL equation of state (EoS) is used extensively to model explosive detonation, and requires a set of material-specific coefficients which can be determined directly from a Cylex test. Tests typically use copper cylinders of either one- or two-inch internal diameter with a length of approximately 10"-12".

The standard one-inch test requires 154 cm^3 of energetic material in order to completely fill the copper cylinder, corresponding to a mass of 250—350 grams for a typical formulation. While a trivial quantity for conventional materials, this required volume can make the test prohibitively expensive to examine new energetic materials. With the rapid discovery of new classes of energetic materials (*e.g.* nanoenergetics, ionic liquids, and other research explosives), it is becoming increasingly important to have a way to quickly evaluate the performance-related properties such as EoS, Gurney velocity, and metal acceleration at a smaller scale to alleviate the expense of scale-up.

With this trend in mind, we have investigated the viability of utilizing a half-inch variant of the

cylinder test. This miniaturized version of the standard test utilizes a half-inch inner diameter copper tube and requires one-eighth the amount of material (19.3 cm^3 or 30-40 grams) of the one-inch test, making it more appropriate for testing new energetic materials. This paper discusses our efforts to validate the miniaturized test by performing a measurement systems analysis on both the half- and one-inch tests using the liquid explosive PLX (nitromethane sensitized with 5% (by wt) ethylene diamine). In addition to analyzing the velocity and displacement profiles obtained from the streak records we examined the results of Photo Doppler Velocimetry (PDV) measurements and CTH hydrocode simulations.

EXPERIMENTAL PROCEDURE

Eight one-inch and fifteen half-inch Cylex tests were conducted using the standard Cylex test configuration [5] in a randomized order over a period of 14 days. The liquid explosive PLX was used in each of the tests and was chosen in order to minimize the effect of voids and irreproducibility associated with filling the narrow cylinders. In addition to the streak record measurements of the cylinder wall expansion, hydrocode simulations of both half- and one-inch tests and PDV measurements on a single half-inch test were performed. The resulting variabilities in velocity at two, seven, and ten volume expansions were extracted for both the left and right hand side of the cylinder and compared to the literature value for the Gurney velocity of nitromethane, 2.41 mm/μsec. [6]

Cylinder Test Details

The standard one-inch test consists of a fully annealed, oxygen-free high-conductivity (OFHC) copper tube with a 1.000 inch inner diameter (ID) and a wall thickness of 0.100 inch. The miniaturized test used tubes made from the same copper material with a 0.500 inch ID and a 0.050 inch wall thickness. Identical setups were used in each test.

To ensure that the test series evaluated the inherent variability of the measurement, great care was taken to fill the cylinders and to construct the set-up reproducibly. Each tube was epoxied to a steel plate to form a liquid tight container, and the PLX was poured into the tube to within approximately 0.25 inch of the top of the tube. A piece of Tygon hosing was used as a riser on the half-inch tests to extend the length of the copper cylinder, allowing for easier placement and alignment of the detonator. Both the half- and one-inch tests were initiated using an RP-80 exploding bridge wire detonator (nominally a 0.295 inch diameter by 0.824 inch cylinder) which was centered on the cylinder and submerged approximately 3/8 inch into the PLX.

The time-dependent displacement of the cylinder wall was measured in the standard fashion by recording the backlit silhouette of a horizontal slice of the cylinder viewed through a slit with a Cordin film streak camera. The backlighting in these experiments was cast by an argon candle located approximately one meter behind the cylinder. Kodax TMAX 400 film was used for all of these measurements and the camera's slit width was approximately 100 μm.

Fig. 1 *(left)* shows a typical Cylex streak record. The top 20% of the record contains the static fiducial, which is exposed before the test and is used for spatial calibration of the image. The bottom 80% of the image shows the expansion of

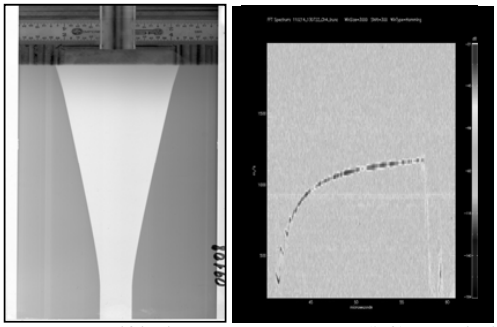

Figure 1. Half-inch test measurements: *(left)* A typical Cylex streak record showing the static fiducial at the top and dynamic cylinder silhouette at the bottom. *(right)* PDV velocity-time trace obtained by taking the Fourier transform of the raw time-intensity.

the cylinder, with time increasing from the bottom to the top of the image.

Given the writing rate of the camera, the image can be converted to a displacement-time representation. Each of the streak records was

digitized, calibrated, processed, and analyzed via an automated procedure written in the IGOR Pro software, the details of which have been described thoroughly elsewhere. [7]

In addition to the standard streak records, a PDV [8] measurement was used on a single half-inch test. This was done to examine the compatibility of the technique to the smaller radius of curvature of the cylinder as well as examine the technique's ability to resolve the shorter ring-up period expected in the thinner wall. Fig. 1 (*right*) shows the velocity-time trace obtained by Fourier transforming the raw PDV signal. In principle, the PDV technique has the advantages of measuring the wall velocity directly (as opposed to the displacement observed in the streak image) and in having a higher resolution, but captures data over a shorter time window (only 15 μsec).

Hydrocode Modeling Details

Both the one- and half-inch diameter Cylex tests were simulated using the CTH hydrocode [9]. The simulations were run in two-dimensional, radially-symmetric cylindrical coordinates, with a mesh size of 0.00787 inches and time increments short enough to resolve the shock ringing in the cylinder walls (<0.05 μsec/step). The explosive was simulated using a JWL EoS and a programmed burn model, and the copper cylinder was simulated by the Mie-Grüneissen EoS and a simple yield-strength model. All dimensions of the simulation were identical to those used experimentally. To obtain analogous information to what is observed on a streak record, tracer points were placed on the outer edge of the wall in the simulation to track its position, velocity, and pressure at each time increment.

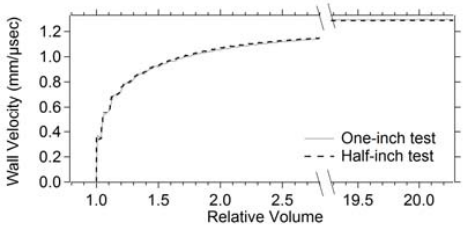

Figure 2. CTH simulations of cylinder wall expansion velocity vs. relative volume expansion for half-inch and one-inch diameter Cylex tests. The results show the theoretical equivalency of the tests across scale.

Fig. 2 shows the simulated cylinder wall velocities for both the half- and one-inch ID models as a function of the relative expansion volume, $v(t)/v(t=0)$, of the explosive. The two velocity profiles are essentially identical out to ten volume expansions, a demonstration of the theoretical equivalency of the one-inch and half-inch tests and simulations across scale.

RESULTS AND DISCUSSION

Fig. 3 shows example CTH and streak record displacement and velocity profiles for both one-inch and half-inch Cylex tests, and PDV data for a half-inch test. The CTH and streak record profiles are in near perfect agreement, aside from a slight deviation in velocity near 3-5 volume expansions (approximately 28 and 30 μs for one- and half-inch tests respectively). The source of the discrepancy has not been identified, but was consistently observed in each of the replicates. Nonetheless, the qualitative agreement indicates the high degree of accuracy in CTH simulations.

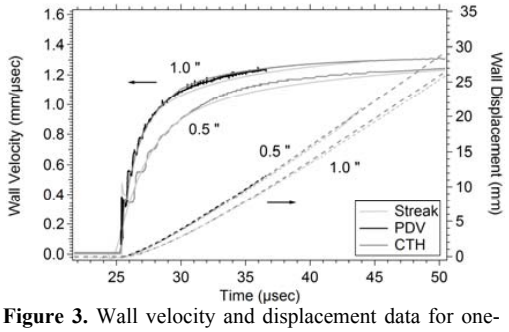

Figure 3. Wall velocity and displacement data for one-inch and half-inch cylex tests, both experimental and CTH hydrocode simulations.

Also in excellent agreement with the streak profiles is the half-inch PDV measurement. In addition to perfectly reproducing the displacement, the reverberations in the copper wall were completely resolved, in contrast to streak data which resolved only the first "pulse." Interestingly, the CTH simulation underestimated the amplitude of these reverberations, a topic that will be investigated further in future tests.

Table 1 summarizes the results of analyzing all of the replicate measurements and comparisons to the CTH and PDV tests, listing the velocities at two, seven, and ten volume expansions as well as the Gurney velocities. The values for the various velocities were statistically indistinguishable. No systematic deviations were observed between the data taken from the right and left side of the streak records, nor were any statistically significant differences observed between the half-inch and one-inch tests. The only notable difference between the two sizes is the approximately four-fold increase in the variability of the half-inch test. However, the uncertainty in velocity is at most 4%, a value which is likely acceptable for most applications.

TABLE 1. Test descriptions, average expansion wall velocities at two, seven, and ten volume expansions, and the calculated Gurney velocity for one- and half-inch Cylex tests. Numbers in parenthesis are the standard deviations of the replicate shot measurements in the last decimal places. Uncertainty in the PDV measurements is due to noise inherent in the single measurement.

Test	# Shots	v_2 (mm/μs)	v_7 (mm/μs)	v_{10} (mm/μs)	v_{Gurney} (mm/μs)
1 inch, right side	8	0.95 (01)	1.19 (01)	1.23 (01)	2.38 (01)
1 inch, left side	8	0.95 (01)	1.19 (01)	1.23 (01)	2.38 (02)
½ inch, right side	15	0.98 (03)	1.19 (05)	1.23 (05)	2.42 (08)
½ inch, left side	15	0.99 (03)	1.21 (04)	1.24 (04)	2.39 (09)
1 inch, CTH	1	0.97	1.21	1.23	2.39
1/2 inch, CTH	1	0.99	1.22	1.25	2.45
½ inch, PDV	1	0.99 (02)	1.21 (05)	(off record)	2.39 (11)

The most important values to compare are the Gurney velocities, which were found to be within the experimental uncertainty of the literature value of (2.41 mm/μsec). Remarkably, both experimental techniques and the CTH simulation agree as well.

CONCLUSIONS

The half-inch Cylex test has been shown to be a viable test for materials with an appropriately small critical diameter. The resulting v_2, v_7, and Gurney velocities were in agreement with the one-inch test within a standard deviation of the average, though the variability in the half-inch test was higher at about ± 4 %. Further, PDV measurements have also been demonstrated to be compatible with the smaller diameter test and have been shown to clearly resolve the early-time, shock-induced features of the cylinder expansion.

DISTRIBUTION A. Approved for public release, distribution unlimited 96ABW-2011-0355.

REFERENCES

1. Gurney, R.W., "The Initial Velocities of Fragments from Bombs, Shells, and Grenades," Army Ballistic Research Laboratory, Report BRL 405, Aberdeen Proving Ground, Maryland , USA, 1943.
2. Souers, P.C., Forbes, J.W., Fried, L.E., Howard, W.M., Anderson, S., Dawson, S., Vitello, P., and Garza, R., " Detonation Energies from the Cylinder Test and CHEETAH V3.0," *Propell., Explos. Pyrot.* Vol. 26, pp. 180-190, 2001
3. Lee, E.L., Hornig, H.C., Kury, J.W., "Adiabatic Expansion of High Explosive Detonation Products," Lawrence Radiation Laboratory Report, UCRL-50422, Livermore, California, USA May 1968.
4. Davis, W.C., "Calibration of a JWL Equation of State," Los Alamos National Laboratory Quarterly Report, M-9-QR-88-1, Los Alamos, New Mexico, USA, Apr 1988.
5. U.S. Military Standard, "Safety and Performance Tests for Qualification of Explosives," MIL-STD-1751, Aug 1982.
6. Meyers, M.A., "Dynamic Behavior of Materials," Wiley-Interscience, New York (1994).
7. Lindsay, C.M., Butler, G.C., Rumchik, C.G., Schulze, B., Gustafson, R., Maines, W.R., "Increasing the Utility of the Copper Cylinder Expansion Test", *Propell., Explos. Pyrot.*, 25(5), 433-439 (2010)
8. Strand, O.T., Goosman, D.R., Martinez, C., Whitworth, T.L., Kuhlow, W.W., "Compact system for high-speed velocimetry using heterodyne techniques," *Rev. Sci. Instr.*, 77(8), 083108 (2006)
9. McGlaun, J.M., Thompson, S.L., Elrick, M.G. "CTH-A Three-Dimensional Shock-Wave Physics Code," *Int. J. Impact Eng.*, Vol. 10, pp. 351-360, (1990),

B

Spectroscopy Papers

Measurement of apparent temperature in post-detonation fireballs using atomic emission spectroscopy

W. K. Lewis[1,a] and C. G. Rumchik[2]
[1]*Sensors Technology Office, University of Dayton Research Institute, Dayton, Ohio 45469, USA*
[2]*U.S. Air Force Research Laboratory, Eglin AFB, Florida 32542, USA*

(Received 22 December 2008; accepted 27 January 2009; published online 9 March 2009)

The energy release dynamics of explosives are of ongoing interest, but the short timescales involved often limit the measurements that can be made during these processes. We have used atomic emission spectroscopy to measure the temperature of fireballs resulting from detonation of charges of Hexahydro-1,3,5-trinitro-1,3,5-triazine doped with barium nitrate. The time-averaged emission spectra indicate an apparent temperature of ~3000 K, in good agreement with theoretical predictions. The technique demonstrated herein should be applicable to time-resolved studies, including those on detonation timescales. © *2009 American Institute of Physics*.
[DOI: 10.1063/1.3089251]

The measurement of energy release and the associated kinetics are of fundamental importance for understanding and controlling exothermic chemical reactions. Although the energy release processes associated with explosives are of ongoing interest, measurements are often made difficult by the fast time scales involved. For gram-scale explosive samples, the detonation wave typically sweeps though the entire sample in several microseconds. The subsequent afterburning of underoxidized detonation products can then produce a fireball that persists for several milliseconds. The fireball often releases more energy than the detonation itself, albeit more slowly.[1] Unfortunately, the time scales associated with these processes limit the measurements that can be made. The high temperatures and pressures involved in explosions also limit measurement options, since any sensors employed must be able to withstand the extreme environment.

To characterize the energy release associated with explosions, it is desirable to determine the temperature and pressure of the system and to date, a variety of techniques have been developed to measure pressure in detonations and fireballs.[2] On the other hand, temperature measurements have been less extensive, partly because sensors rugged enough to withstand the explosion have response times longer than the phenomena of interest. Atomic and molecular emission spectroscopies would seem to be attractive techniques for temperature measurement, particularly given that they have been used extensively to study the structure and dynamics of flames[3] and plasmas.[4] Additionally, such techniques can be used to measure very fast processes and an emission spectrum can be recorded at a distance from the explosion. The results from several studies utilizing emission spectroscopy in the visible[5–8] and IR[9,10] spectral regions to examine explosives have now been reported. We note that while pyrometry methods have also been used to measure temperatures during explosions, recent work suggests that quantitative interpretation of such data can be problematic without detailed phenomenological knowledge of the emissivity function.[11]

However, emission spectra obtained from explosions are often complex, with many emission bands, which are frequently overlapping.[5–10] Additionally, broad emission from incandescent particles can be observed, as well as signals from impurities with strong emission lines. These factors make it difficult to interpret the resulting spectra. An alternative approach is to dope an explosive with an impurity that will produce atomic emissions, which are simpler to interpret, thereby introducing an atomic "thermometer" into the sample. Flames have been studied analogously by seeding thermometric species into burners.[3,12] Interestingly, Wilkinson *et al.*[6] have recently observed Al atomic emission lines in the spectrum of aluminum-rich explosives and were able to use these signals to measure the temperature of the vaporized aluminum. However, in these studies the aluminum was present in substantial concentration in order to increase the energy released by the explosive sample. An ideal thermometric impurity would be present only in small concentrations to avoid perturbing the chemical dynamics of the system and minimize the effects of self-absorption. Additionally, candidate thermometric species must produce several strong emission lines in the spectrum that originate from different upper energy levels in order to allow the populations of the associated states to be determined.

Barium nitrate was chosen as a thermometric impurity for the current work since Ba atoms emit several strong well-characterized lines in the visible region that originate from different upper energy levels. Charges of either Hexahydro-1,3,5-trinitro-1,3,5-triazine (RDX) or RDX doped with a small amount (1 wt %) of barium nitrate were prepared. It is known from slot-burner flame studies that higher concentrations of thermionic impurities become problematic due to self-absorption effects.[12] To prepare the barium-doped explosive charges, barium nitrate was ball milled for several hours to produce a fine powder. The milled barium nitrate was then combined with RDX and a hydroxyl-terminated polybutadi-

[a]Author to whom correspondence should be addressed. Electronic mail: lewiswik@notes.udayton.edu.

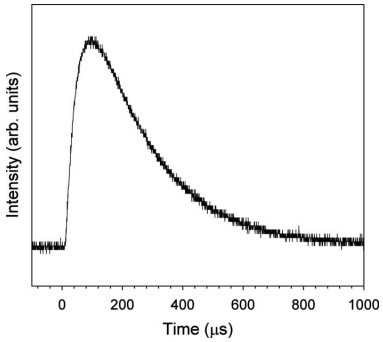

FIG. 1. Typical photodiode trace recording the relative radiance of the fireball generated following detonation of a 40 g charge of RDX.

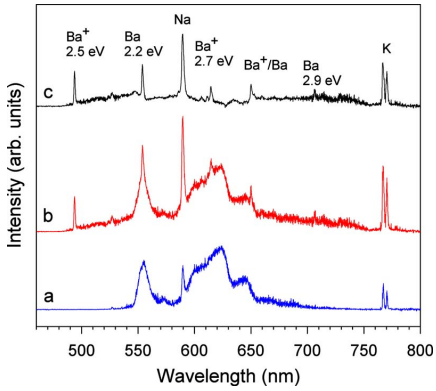

FIG. 2. (Color online) (a) Emission spectra collected following detonation of RDX and (b) RDX doped with 1% barium nitrate by weight. (c) The difference spectrum is also shown and exhibits strong signals from barium atom and barium ion emissions. The apparent temperature of both barium species can be calculated from the relative intensities of the respective emission lines in the difference spectrum.

ene (HTPB) binder and mixed thoroughly. Undoped RDX charges were prepared by mixing RDX with the HTPB binder without barium nitrate. The two mixtures were then pressed into 1 in diameter cylindrical charges of 40 g total mass. Both types of charges contained 6 wt % HTPB binder. The bare charges were then detonated using Reynolds RP-81 detonators.

Light from the explosions was collected using 5 mm diameter collection lenses mounted to the ends of 1000 μm core-diameter fiber optics (Ocean Optics). The collection optics were placed in an observation room located approximately 5 m away from the explosive charges and were aligned to view the center of each charge through a protective BK7 glass view port. The light collected by the fiber optics was sent to a photodiode with a nominal time resolution of 1 ns (Thorlabs Det10A) and a spectrometer with a resolution of ~1 nm and a usable spectral range of ~460–800 nm (Ocean Optics USB-4000). We note that in order to avoid saturating the photodiode signal, a neutral density filter was placed between the fiber optic output and the photodiode detector.

The relative radiance of the fireball as a function of time was measured by recording the photodiode signal using a digital oscilloscope (Tektronix). A typical photodiode trace is shown in Fig. 1, where $t=0$ corresponds to the detonator firing signal. Following detonation of the charge, emission from a fireball was observed for several hundred microseconds. Emission spectra during this time were collected by the spectrometer, which was configured to be triggered by the detonator signal. The integration interval of the spectrometer was 5 ms, which captured all of the light output of the fireball. The wavelength and intensity axes of the spectrometer were calibrated before the explosive shots using a mercury-argon lamp (Oriel) and a tungsten-halogen lamp with a known color temperature (Ocean Optics), respectively. Finally, each shot was repeated several times to confirm reproducibility.

In Fig. 2 we show typical spectra collected following detonation of RDX charges [Fig. 2(a)], RDX charges with 1% barium nitrate impurity [Fig. 2(b)], and the difference spectrum [Fig. 2(c)] generated from subtracting the former from the latter. We note that the spectra were subtracted as collected, without employing any scaling procedures. In the spectrum of pure RDX [Fig. 2(a)], we see several broad emissions as well as sharp lines at 589, 766, and 770 nm. The sharp lines most likely result from sodium and potassium impurities.[13] The broad emissions are more difficult to interpret and likely contain contributions from several vibronic bands, but a full assignment of these emission signals is beyond the scope of this initial investigation. Interestingly, the spectrum appears to be largely free from emissions from incandescent particles, which we would expect to produce a broad gray-body continuum signal. Examination of the spectrum of RDX doped with barium nitrate [Fig. 2(b)] reveals the same complex emission spectrum observed for undoped RDX, except now we also find several well-known emission lines from barium atoms and cations at 493, 554, 614, 650, and 706 nm. We note that the sodium and potassium emissions have also increased in intensity, suggesting that these may be present as impurities in our barium nitrate sample as well.

The difference spectrum [Fig. 2(c)] shows a nearly background-free spectrum in which the atomic emissions from barium atoms and cations are quite clear. We find strong peaks at 554 and 706 nm assigned to the $^1S_0 \leftarrow {}^1P_1^0$ and $^3D_3 \leftarrow {}^3F_4^0$ transitions in Ba atoms and peaks at 493 and 614 nm assigned to the $^2S_{1/2} \leftarrow {}^2P_{1/2}^0$ and $^2D_{5/2} \leftarrow {}^2P_{3/2}^0$ transitions in Ba^+ ions, respectively.[14] We note that the peak at 650 nm may have contributions from both $Ba(^3D_3 \leftarrow {}^3D_3^0)$ and Ba^+ $(^2D_{3/2} \leftarrow {}^2P_{1/2}^0)$ at the resolution of our spectrometer (~1 nm). Since the associated energy levels, degeneracies, and Einstein A coefficients for each of these transitions are well known,[14] we can calculate the apparent temperature from the Boltzmann populations of the energy levels using the two-line method.[3,6,15] Examining the Ba^+ ion signals at 493 and 614 nm, which originate from states 2.5 and 2.7 eV above the ground state, respectively,[14] we obtain an apparent

temperature of 2800 ± 400 K. Applying the same method to the Ba atom peaks at 554 and 706 nm, corresponding to levels 2.2 and 2.9 eV above the ground state,[14] we find an apparent temperature of 3600 ± 1000 K. The larger uncertainty of this value reflects the lower signal-to-noise ratio of the peak at 706 nm.

Although these values are in agreement within the uncertainty and agree well with the theoretical adiabatic flame temperature of 3150 K (calculated using the method outlined in Ref. 1), we must be cautious in our interpretation of these results since it has been shown that the apparent temperature of a flame may differ by several hundred Kelvin from the average temperature in nonisothermal flames.[16] This is not a serious limitation in the present case, since the spectra shown herein already represent time-averaged results. Additionally, the optical depth of the fireball is not currently known. Nevertheless, these results demonstrate the viability of the basic technique, and future experiments are planned to measure time-resolved temperatures inside detonations and fireballs using spectrometers with improved sensitivity and spectral range. Finally, we believe that this technique may also be useful to measure the temperature of fireballs resulting from complex explosive mixtures, for which calculation of the theoretical fireball temperature is not straightforward.

Funding and facilities for this work were provided by the Air Force Research Laboratory. We would like to thank Rick Beesley, Mark Johnson, and Rachel Nep of Eglin Air Force Base and Lara Harris from The United States Air Force Academy for their assistance in conducting these experiments.

[1] P. W. Cooper, *Explosives Engineering* (Wiley, New York, 1996).
[2] B. T. Federoff, H. A. Aaronson, E. F. Reese, O. E. Sheffield, and G. D. Clift, *Encyclopedia of Explosives and Related Items* (National Technical Information Service, Springfield, VA, 1999).
[3] A. G. Gaydon, *The Spectroscopy of Flames* (Wiley, New York, 1957).
[4] K. C. Lapworth, J. Phys. E **7**, 413 (1974).
[5] J. R. Carney, J. S. Miller, J. C. Gump, and G. I. Pangilinan, Rev. Sci. Instrum. **77**, 063103 (2006).
[6] J. Wilkinson, J. M. Lightstone, C. J. Boswell, and J. R. Carney, in *Shock Compression of Condensed Matter*, edited by M. Elert, M. D. Furnish, R. Chau, N. Homes, and J. Nguyen (American Institute of Physics, Melville, NY, 2007), p. 1271.
[7] V. Bouyer, G. Baudin, C. Le Gallic, and P. Hervé, in *Shock Compression of Condensed Matter*, edited by M. D. Furnish, N. N. Thadhani, and Y. Horie (American Institute of Physics, Melville, NY, 2001), p. 1223.
[8] V. Bouyer, I. Darbord, P. Hervé, G. Baudin, C. Le Gallic, F. Clément, and G. Chavent, Combust. Flame **144**, 139 (2006).
[9] J. A. Orson, W. F. Bagby, and G. P. Perram, Infrared Phys. Technol. **44**, 101 (2003).
[10] K. C. Gross, J. Wayman, and G. P. Perram, Proc. SPIE **6566**, 656613 (2007).
[11] P. T. Lynch, H. Krier, and N. Glumac (personal communication).
[12] I. Reif, V. A. Fassel, and R. N. Kniseley, Spectrochim. Acta, Part B **30**, 163 (1975).
[13] *CRC Handbook of Chemistry and Physics*, 80th edition, edited by D. R. Lide (CRC, Cleveland, 2000).
[14] J. J. Curry, J. Phys. Chem. Ref. Data **33**, 725 (2004).
[15] I. Reif, V. A. Fassel, and R. N. Kniseley, Spectrochim. Acta, Part B **28**, 105 (1973).
[16] I. Reif, V. A. Fassel, and R. N. Kniseley, Spectrochim. Acta, Part B **29**, 79 (1974).

JOURNAL OF APPLIED PHYSICS **111**, 014903 (2012)

Time-resolved spectroscopic studies of aluminized explosives: Chemical dynamics and apparent temperatures

W. K. Lewis,[1,a)] C. G. Rumchik,[2] P. B. Broughton,[2] and C. M. Lindsay[2]
[1]*University of Dayton Research Institute, Dayton, Ohio 45469, USA*
[2]*U.S. Air Force Research Laboratory, Eglin AFB, Florida 32542, USA*

(Received 27 September 2011; accepted 28 November 2011; published online 4 January 2012)

Time-resolved emission spectroscopy and high-speed photography were used to study the chemical dynamics and thermal history of aluminized hexahydro-1,3,5-trinitro-1,3,5-triazine (RDX) charges following detonation. The aluminized RDX charges contained 20 wt. % of either 30-70 nm or 16-26 μm Al particles. Non-aluminized RDX charges were also studied for comparison. Spectra collected from the aluminized charges exhibited Al and AlO emissions during the first ~60 μs, followed by a broadband emission that evolved over two time scales: one in the early time, 0-200 μsec, and another on late time, 0.5-10 ms. The apparent temperatures of the early-time fireballs were obtained using barium atom thermometry and were found to be ~2900 K for the RDX-only charges, ~3600 K for the RDX-micron Al charges, and ~4000 K for the RDX-nano Al charges. In both types of aluminized samples, once Al and AlO emissions ceased, the fireballs began to cool and approached the temperature obtained for the non-aluminized RDX charges. For aluminized charges, a late-time luminescence was also observed, with the intensity and duration dependent upon the size of the Al particles. Aluminum nanoparticles yielded a higher early-time temperature, but a less intense and shorter duration late-time emission, while micron-sized particles produced a lower early-time temperature, but a longer-lived and more intense late-time energy release. These results indicate that post-detonation Al combustion occurs in multiple stages during the evolution of the fireball. © *2012 American Institute of Physics*. [doi:10.1063/1.3673602]

INTRODUCTION

The incorporation of aluminum particles into explosive formulations has been a subject of ongoing interest, due to the potential of aluminum particles to increase the energy content of explosives and also to tailor the energy release rate via the choice of particle size. To date, a large number of aluminized explosive formulations have been studied, as summarized in several reviews.[1,2] In general, it has been found (at least for oxide-passivated particles) that, due to the high melting point[3] (2054 °C) and/or mechanical strength of the oxide shell, the Al particles react slowly relative to detonation processes and contribute primarily to "late-time effects", such as post-detonation fireballs and air blast.[1] Consequently, aluminum particles have found applications in air-blast and incendiary formulations. We note that the situation may be different for organically capped Al nanoparticles, given that their organic shell is lost at temperatures of 200-300 °C.[4,5]

The study of the energy release process in formulations that incorporate metal particles is complicated by several factors. First, there are generally two fuels available for combustion: organics/soot and the embedded metal particles. During energy release, it is not always clear which of these two available fuels is being oxidized. Secondly, although time-resolved pressure and temperature measurements are desirable to characterize energy release, measuring temperatures following the detonation of an explosive is especially challenging. A variety of methods[6] have been developed to measure pressure in detonations and fireballs, but temperature sensors durable enough to withstand the explosion have response times longer than the duration of the event. Pyrometry methods have been employed in order to measure temperatures, but interpretation of the results can be problematic without detailed knowledge of the emissivity function of the species contained in the flame.[7]

In a previous investigation,[8] we developed an atomic emission spectroscopy-based technique to measure the temperature in post-detonation fireballs by doping the explosive charge with an inorganic impurity. The temperature is then determined by monitoring the relative intensities of atomic emission lines corresponding to emission from different energy levels of a selected atom. The purpose of the current study is to combine this approach with that of earlier groundbreaking investigations,[9–15] which used time-resolved emission spectroscopy methods to characterize the complex chemical dynamics occurring following detonation of an explosive charge. Our goal is to monitor the combustion of Al particles within the overall chemical dynamics of the explosion and to correlate this with the energy release process.

EXPERIMENT

Pressed right-cylindrical charges were prepared from a mixture of hexahydro-1,3,5-trinitro-1,3,5-triazine (RDX) powder (74 wt. %), a hydroxyl-terminated polybutadiene (HTPB) binder (6 wt. %), and an aluminum powder (20 wt. %) chosen from either Toyal X-81 (16-26 μm particle size) or Nano Technologies nano-aluminum (30-70 nm particle size). The

[a)]Author to whom correspondence should be addressed. Electronic mail: lewiswik@notes.udayton.edu.

22-g pressed charges were 2.5 cm in diameter by 2.5 cm in height. In order to establish a baseline for comparison, charges were also prepared with no Al content (94 wt. % RDX, 6 wt. % HTPB binder). For thermometric spectroscopy measurements, charges were prepared as above, except that ball-milled barium nitrate was added (1 wt. %) to the mixture and mixed thoroughly before pressing. All charges were initiated using Reynolds RP-80 detonators placed on the end of each cylindrical charge.

Light from the explosions was collected from the end of the charge opposite the detonator using a 5-mm-diameter collection lens mounted to the end of a 1000-μm core-diameter fiber optic (Ocean Optics). The collection optics were placed in a shielded observation room located approximately six meters away from the explosive charges and were aligned to view the center of each charge through a protective BK7 glass viewport. The collected light was sent to a time-resolved emission spectrograph constructed from a 1/8 m spectrometer (Oriel) equipped with a 50-μm entrance slit and a 600 lines/mm rotatable grating interfaced to a 4096 pixel line-scan camera (Basler Sprint) with a data collection rate of 1-70 kHz. The resolution and usable spectral range of the spectrograph were 1.0 nm and 360-800 nm, respectively. The wavelength and intensity axes of the spectrograph were calibrated with a mercury-argon lamp (Ocean Optics) and a halogen lamp with a known color-temperature (Thorlabs). We note that, due to the low light intensity of the color-temperature lamp in the blue region of the spectrum and the short maximum integration time of the spectrograph (1 ms), the spectrum could not be corrected for instrument response below ~460 nm. The spectrograph was triggered by the fire control circuits used to detonate the explosive charges. Spectra were recorded at integration periods of either 15 or 50 μs per scan (depending upon the intensity of the collected light) for 3.0 ms following detonation, and every shot was repeated at least three times in order to ensure reproducibility.

As a supplement to the time-resolved spectroscopy, high-speed videos were also obtained using a Model V7.1 Phantom camera. The images obtained here were recorded at 4.7 kHz with a 19 μs exposure time, and the light was passed through a 10-nm narrow wavelength bandpass filter centered at 600 nm. We note that in the current investigation detonation should be complete within ~5 μs of detonator initiation, given the length of the charge (25 mm) and the detonation velocity of the formulation (~7.5 km/s), with subsequent emission assigned to the post-detonation fireball resulting from afterburning of under-oxidized detonation products.

RESULTS AND DISCUSSION

In Figs. 1(a) and 1(b) we show the emission spectra obtained following detonation of the non-aluminized RDX charges doped and undoped with $Ba(NO_3)_2$, respectively. The integration period for these shots was 50 μs. In the un-doped charges, a broadband emission is observed along with Na emission at 589 nm resulting from Na impurities[3] in the sample. Smaller signals are also observed at 766 and 770 nm due to K impurities,[3] and several weak vibronic bands are

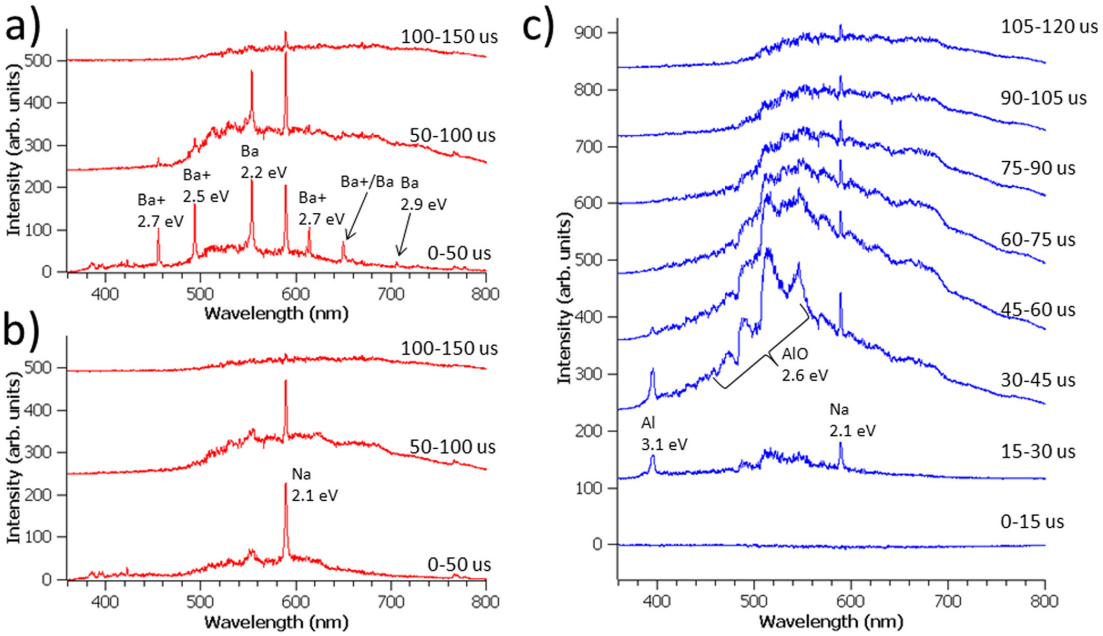

FIG. 1. (Color online) Time-resolved emission spectra obtained from detonation of 22 g charges of (a) barium nitrate–doped RDX recorded with an integration period of 50 μs, (b) un-doped RDX recorded with an integration period of 50 μs, and (c) RDX containing 20 wt. % Al particles (16-26 μm particle size) recorded with an integration period of 15 μs. Prominent peaks and bands are labeled with the identity of the emitting species and the energy of the upper electronic state involved in the transition.

present throughout the spectrum. The spectra obtained from the charges doped with $Ba(NO_3)_2$ are virtually identical to those from the un-doped charges, aside from the emission lines from Ba atoms and cations. In the first scan (0-50 μs), we find peaks at 554 nm and 706 nm assigned to the $^1S_0 \leftarrow {}^1P_1$ and $^3D_3 \leftarrow {}^3F_4$ transitions in Ba atoms and peaks at 455, 493, and 614 nm assigned to the $^2S_{1/2} \leftarrow {}^2P_{3/2}$, the $^2S_{1/2} \leftarrow {}^2P_{1/2}$, and the $^2D_{5/2} \leftarrow {}^2P_{3/2}$ transitions in Ba^+ ions, respectively.[16] The peak at 650 nm may have contributions[16] from both Ba ($^3D_3 \leftarrow {}^3D_3$) and Ba^+ ($^2D_{3/2} \leftarrow {}^2P_{1/2}$) at the ~1 nm resolution of the spectrograph. In subsequent scans (i.e., at later times), the intensity of these signals decrease, with the emissions originating from higher energy states losing intensity faster than those emitting from lower energy states. In the third scan (100-150 μs), only the Na line corresponding to emission from an energy level 2.1 eV above the ground state is observed. Also, the broadband emission has shifted to longer wavelength and lost intensity. Each of these observations indicates a cooling of the post-detonation fireball with time.

We now turn our attention to the aluminized charges. Figure 1(c) shows the time-resolved emission spectra obtained following detonation of an RDX-Al charge (20 wt. % Al, 16-26 μm particle size), with an integration period of 15 μs. Little emission is observed for 15 μs following the detonator trigger. In the next scan (15-30 μs), Al $^2P_{1/2} \leftarrow {}^2S_{1/2}$ and $^2P_{3/2} \leftarrow {}^2S_{1/2}$ atomic emissions appear at 394 and 396 nm, respectively,[17,18] along with the AlO $X \leftarrow B$ emission band.[19] These signals are also prominent in the third scan, but then weaken in successive spectra. Simultaneously, a large broadband emission grows in and mostly fades away after ~200 μs. Observation of Al atomic emission peaks, the AlO vibronic band, and a broadband emission is typical of aluminum combustion.[20–24] Spectra collected from the samples containing the nano-Al particles (not shown) are similar and exhibit the same features, namely atomic Al lines, the AlO band, and a prominent broadband emission. The spectra of the aluminized charges doped with $Ba(NO_3)_2$ were identical to those obtained from the un-doped charges aside from the Ba and Ba^+ emission lines.

Although the spectra collected from the RDX charges containing the nano- and micron-sized aluminum powders were similar, their time-dependence was significantly different. In Fig. 2, we show the time dependence of the broadband emission measured at 600 nm and the atomic Al emission line at 396 nm for each of the samples studied. The decay of each broadband emission is fit to a first-order exponential decay. In the spectra obtained from the RDX-only charges, the intensity of the broadband emission peaks at 50-100 μs and then decays with a time constant of 37 ± 8 μs. The behavior of the RDX-micron Al charges is not dramatically different; it peaks at 45-60 μs and falls with a time constant of 42 ± 5 μs. There are, however, significant differences between the micron- and nano-aluminum/RDX charges, with the latter having both a faster onset (30 μs versus 45 μs) and faster decay (28 μs versus 42 μs). But these differences are perhaps not as dramatic as might be expected, given that the Al nanoparticles are more than two orders of magnitude smaller than the micron-sized Al particles.

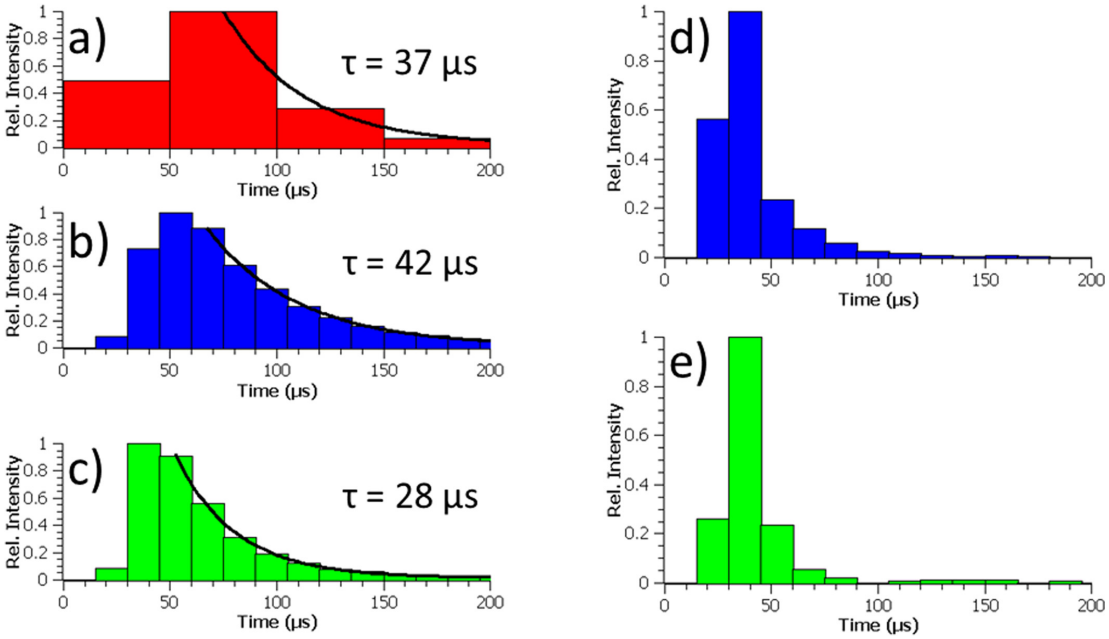

FIG. 2. (Color online) Time dependence of the broadband emission measured at 600 nm for charges of (a) RDX only, (b) RDX with 20 wt. % micron-sized aluminum particles, and (c) RDX with 20 wt. % aluminum nanoparticles. First-order exponential decay fits and the associated time constants are shown. Time dependence of the atomic Al emission at 396 nm for (d) RDX with 20 wt. % micron-sized aluminum particles and (e) RDX with 20 wt. % aluminum nanoparticles.

The atomic Al and the AlO band emissions provide further insight into the combustion process. Figures 2(d) and 2(e) show the time dependence of the Al line at 396 nm for the RDX charges containing the micron-sized and nanometer-sized Al particles, respectively. Unfortunately, the AlO band intensity could not be extracted because of the overlapping broadband emission. Nevertheless, qualitative inspection of the spectra in Fig. 1(c) confirms that the AlO band, like the atomic Al lines, is primarily observed for $t \leq 60$ μs. This time scale is significantly shorter than the duration of the broadband emission, suggesting that the latter is due to afterburning of soot or organics produced by the detonation. However, we cannot rule out a contribution at 60 $\mu s \leq t \leq 200$ μs from combustion of Al particles in air via processes that avoid production of gas-phase Al and AlO. Since the Al and AlO signals originate only from gas-phase species, oxidation processes that avoid them would not exhibit these emissions. For example, chemical reactions that either quickly consume Al and AlO or compete with their formation would be consistent with this possibility. Such processes have been previously suggested to explain low AlO emission levels during some Al nanoparticle reactions.[25]

Time-resolved temperature measurements obtained from the Ba-doped charges provide additional insight into these issues. The apparent temperature of the fireball was obtained by the two-line method, utilizing the 554 and 706 nm Ba emission lines, since they persist longest following the detonation. The results of this analysis are shown in Fig. 3 and indicate that the RDX-only charges produce a peak fireball temperature of ~2900 K and that the temperature decreases in time. These results are in good agreement with the theoretical adiabatic flame temperature of 3150 K (calculated using the method in Ref. 26) and with the qualitative inference above that the fireballs were cooling based upon the fact that the intensity of the various peaks decreased consistent with their relative energetics. For the RDX-micron Al charges, we observe a higher apparent temperature of ~3600 K that smoothly decreases, ultimately approaching the temperatures obtained for the RDX-only charges before Ba signals vanish. We find the highest apparent temperatures for the RDX-nano Al charges at ~4000 K and see that the temperature drops precipitously after ~60 μs, again approaching that of the RDX-only charges. We note that, while both types of aluminized charges initially exhibit higher apparent temperatures than the RDX-only samples, once the Al and AlO signals in the spectra cease, the temperatures approach those obtained for the RDX-only charges. This result suggests that free/gaseous aluminum combustion occurs early in the evolution of the fireball ($t \leq 60$ μs), increasing the temperature above that observed for RDX alone, and that subsequent emissions (60 $\mu s \leq t \leq 200$ μs) primarily correspond to other chemistry. This is supported by the fact that in the present study the Al and AlO emissions were always observed in coincidence, even though the upper energy levels corresponding to these emissions are somewhat different (3.1 eV for Al[17,18] versus 2.6 eV for AlO[27]). If these emissions were unrelated to ongoing Al combustion, we would expect them to vanish consistent with their relative energetics, i.e., we would expect the AlO band to persist longer than the Al lines.

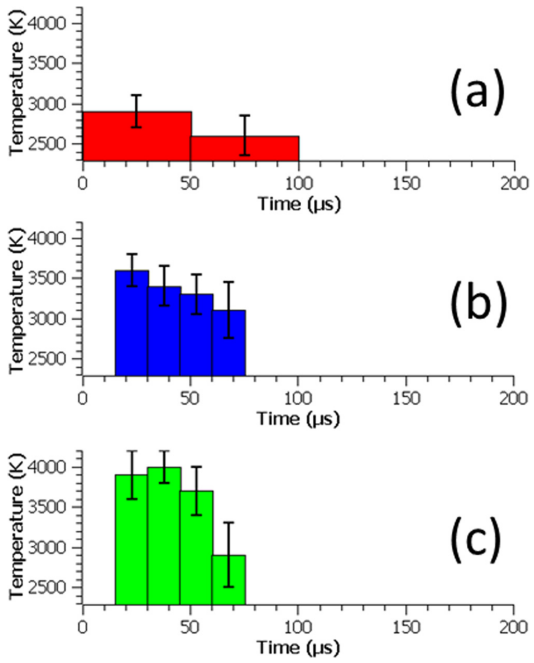

FIG. 3. (Color online) Apparent temperatures obtained from the atomic Ba emissions exhibited by the charges doped with 1 wt. % barium nitrate. The temperature was calculated by the two-line method using the intensities of the Ba peaks at 554 and 706 nm. Time-resolved temperature measurements are shown for (a) RDX only, (b) RDX with 20 wt. % micron-sized aluminum particles, and (c) RDX with 20 wt. % aluminum nanoparticles. The 95% confidence levels are shown.

The early-time chemistry is not, however, the only energy release process that involves the Al particles. For the aluminized charges, we observe another emission subsequent to both the early-time Al combustion ($t \leq 60$ μs) and the broadband emission ($t \leq 200$ μs), presumably arising from afterburning of soot and organics. Figure 4 shows the spatial distribution of the broadband emission at 600 nm obtained over the first few milliseconds for the RDX only, RDX-micron Al, and RDX-nano Al charges. Efforts to simultaneously observe the spatial distribution of Ba emissions using wavelength filters proved unsuccessful, most likely due to the weakness of the emissions at late-time as suggested in the spectrographic data. It is important to point out that the spectrograph, with its short focal length collection lens, has a wide field of view and samples the entire blast structure. Hence, those results correspond to an approximately spatially averaged measurement over the structure apparent in Fig. 4. The first frame of each sequence shows the early-time (camera-saturated) bright flash, corresponding to the data obtained from the spectrograph. Although the observed differences in spatial structure are not significant (they are due primarily to jitter in the camera trigger), the observation of a dark ring and variances in the radial intensity strongly suggest temperature gradients across the blast. Also clearly observable are significant differences in emission intensity and decay rates in the late time blast between the different

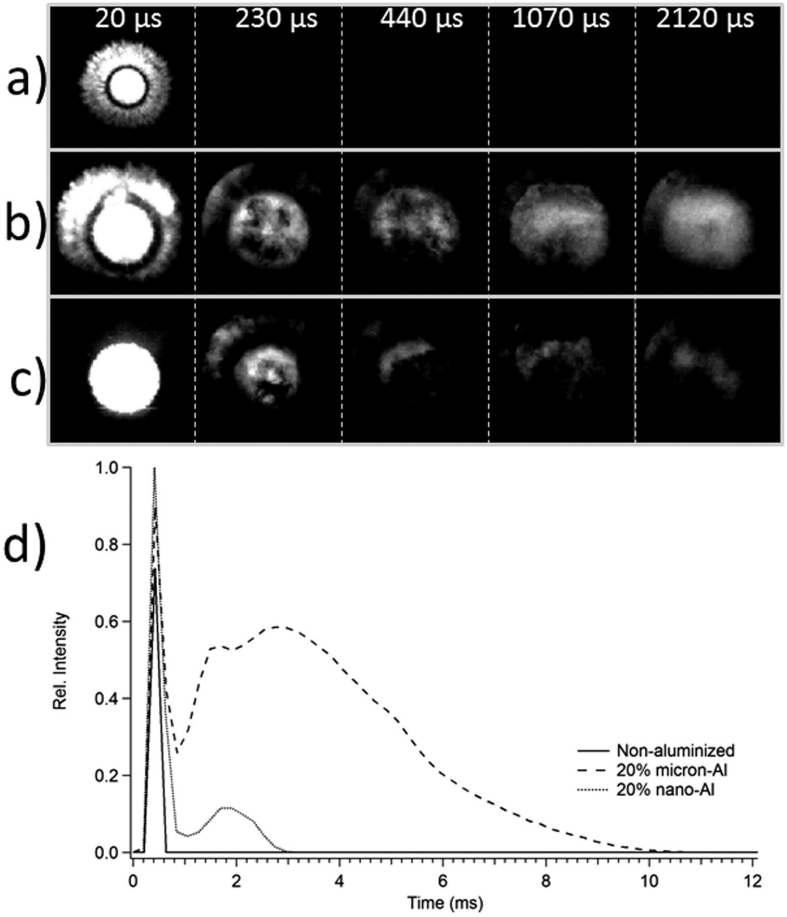

FIG. 4. Time dependence of the broadband emission at 600 nm obtained from a wavelength-filtered high-speed camera for various charges: (a) RDX only, (b) RDX with 20 wt. % micron-sized aluminum particles, and (c) RDX with 20 wt. % aluminum nanoparticles. Exposure time for each image was 19 μs.

charges, noting that the micron aluminum has the brightest, most persistent late-time blast, and that the non-aluminized charge shows none. The observed time-dependent differences in radial intensity are most likely related to differences in the speed of the aluminum particles in the complex gas-solid flow following detonation, as well as their combustion properties. This phenomenon has been the subject of detailed study for both inert[28,29] and reactive[30] metal particles.

Figure 4(d) shows the 600 nm broadband emission in the late time, highlighting the dramatically different behavior. The RDX-only charges show essentially no emission beyond the first ~200 μs, whereas both aluminized charges show a second emission wave. The total emission from the micron aluminum charges from 0.2-10 ms is over an order of magnitude higher than that from the nano-aluminum charges and decays much more slowly (4 ms time constant versus 0.6 ms). We note that the peak intensity of this second emission must be small relative to that for $t \leq 200$ μs, because the late-time luminescence, so clearly visible in Fig. 4, does not generate an observable signal on the spectrograph. Considering that the total mass of aluminum is the same in both cases, this data reinforces the idea that the nano-aluminum is burning and releasing heat to a greater extent in the early time of the blast. The late-time combustion would seem to be consistent with combustion on the surface of aluminum particles, presumably with oxygen in the air, slowly over time.

CONCLUSIONS

Taken together, our spectrographic results, combined with the high-speed imaging data, imply a multi-step energy release process, in which the Al particles react in two distinct stages following detonation of the RDX charge. During an "early time" phase (~60 μs in the current study) free/gaseous Al combustion occurs in the post-detonation fireball, increasing the temperature significantly. As this process ceases, the temperature then drops, approaching that obtained for non-aluminized charges. Broad-band light emission continues for several hundred microseconds more, presumably as soot and/or under-oxidized organics continue to burn. Finally, a "late time" energy release occurs for aluminized samples on the millisecond time scale, with the intensity and duration

dependent upon the size of the Al particles. Aluminum nanoparticles yield a higher early-time temperature, but yield a less intense and shorter duration late-time emission, while micron-sized aluminum produces a lower early-time temperature, but a longer-lived and more intense late-time energy release. These results highlight the ability to tailor energy release somewhat via the choice of Al particle size, but also reveal that post-detonation Al combustion occurs in multiple stages during the evolution of the fireball for both nano- and micron-sized Al particles.

ACKNOWLEDGMENTS

Funding and facilities for this work were provided by the Air Force Research Laboratory under the NanoEnergetics Program. We would like to thank Mr. Rick Beesley for his assistance in conducting these experiments.

[1]P. P. Vadhe, R. B. Pawar, R. K. Sinha, S. N. Asthana, and A. S. Rao, Combust., Explos. Shock Waves **44**, 461 (2008).
[2]E. Anderson, Prog. Astronaut. Aeronaut **155**, 2 (1993).
[3]*CRC Handbook of Chemistry and Physics*, 80th ed., edited by D. R. Lide (CRC, Boca Raton, 2000).
[4]R. J. Jouet, A. D. Warren, D. M. Rosenberg, V. J. Bellitto, K. Park, and M. R. Zachariah, Chem. Mater. **17**, 2987 (2005).
[5]K. A. S. Fernando, M. J. Smith, B. A. Harruff, W. K. Lewis, E. A. Guliants, and C. E. Bunker, J. Phys. Chem. C **113**, 500 (2009).
[6]B. T. Federoff, H. A. Aaronson, E. F. Reese, O. E. Sheffield, and G. D. Clift, *Encyclopedia of Explosives and Related Items* (National Technical Information Service, Springfield, VA, 1999).
[7]P. Lynch, H. Krier, and N. Glumac, J. Thermophys. Heat Transfer **24**, 301 (2010).
[8]W. K. Lewis and C. G. Rumchik, J. Appl. Phys. **105**, 056104 (2009).
[9]J. A. Orson, W. F. Bagby, and G. P. Perram, Infrared Phys. Technol. **44**, 101 (2003).
[10]J. R. Carney, J. S. Miller, J. C. Gump, and G. I. Pangilinan, Rev. Sci. Instrum. **77**, 063103 (2006).
[11]J. Wilkinson, J. M. Lightstone, C. J. Boswell, and J. R. Carney, in *Shock Compression of Condensed Matter*, edited by M. Elert, M. D. Furnish, R. Chau, N. Homes, and J. Nguyen (American Institute of Physics, Melville, NY, 2007), p. 1271.
[12]K. C. Gross, J. Wayman, and G. P. Perram, Proc. SPIE **6566**, 656613 (2007).
[13]J. D. Koch, S. Piecuch, J. M. Lightstone, J. R. Carney, and J. Hooper, J. Appl. Phys. **108**, 036101 (2010).
[14]V. Bouyer, G. Baudin, C. Le Gallic, and P. Hervé, in *Shock Compression of Condensed Matter*, edited by M. D. Furnish, N. N. Thadhani, and Y. Horie (American Institute of Physics, Melville, NY, 2001) p. 1223.
[15]V. Bouyer, I. Darbord, P. Hervé, G. Baudin, C. Le Gallic, F. Clément, and G. Chavent, Combust. Flame **144**, 139 (2006).
[16]J. J. Curry, J. Phys. Chem. Ref. Data **33**, 725 (2004).
[17]K. B. S. Eriksson and H. B. S. Isberg, Ark. Fys. **23**, 527 (1963).
[18]C. Mendoza, W. Eissner, M. Le Dourneuf, and C. J. Zeippen, J. Phys. B **28**, 3485 (1995).
[19]R. W. B. Pearse and A. G. Gaydon, *The Identification of Molecular Spectra* (Chapman and Hall, London, 1963).
[20]J. L. Gole and R. N. Zare, J. Chem. Phys. **57**, 5331 (1972).
[21]S. Rosenwaks, R. E. Steele, and H. P. Broida, J. Chem. Phys. **63**, 1963 (1975).
[22]S. Goroshin, J. Mamen, A. Higgins, T. Bazyn, N. Glumac, and H. Krier, Proc. Combust. Inst. **31**, 2011 (2007).
[23]M. Jackson, M. Pantoya, and W. Gill, Combust. Flame **153**, 58 (2008).
[24]P. Escot Bocanegra, D. Davidenko, V. Sarou-Kanian, C. Chauveau, and I. Gökalp, Exp. Therm. Fluid Sci. **34**, 299 (2010).
[25]R. A. Yetter, G. A. Risha, and S. F. Son, Proc. Combust. Inst. **32**, 1819 (2009).
[26]P. W. Cooper, *Explosives Engineering* (Wiley VCH, Berlin, 1996).
[27]H. H. Michels, J. Chem. Phys. **56**, 665 (1972).
[28]F. Zhang, D. L. Frost, P. A. Thibault, and S. B. Murray, Shock Waves **10**, 431 (2001).
[29]D. L. Frost, C. Ornthanalai, Z. Zarei, V. Tanguay, and F. Zhang, J. Appl. Phys. **101**, 113529 (2007).
[30]S. Goroshin, D. L. Frost, J. Levine, A. Yoshinaka, and F. Zhang, Propellants, Explos., Pyrotech. **31**, 169 (2006).

JOURNAL OF APPLIED PHYSICS **113**, 024903 (2013)

Emission spectroscopy of the interior of optically dense post-detonation fireballs

W. K. Lewis,[1,a)] C. G. Rumchik,[2] and M. J. Smith[3]
[1]*University of Dayton Research Institute, Dayton, Ohio 45469, USA*
[2]*U.S. Air Force Research Laboratory, Munitions Directorate, Eglin AFB, Florida 32542, USA*
[3]*U.S. Air Force Research Laboratory, Propulsion Directorate, Wright-Patterson AFB, Ohio 45433, USA*

(Received 1 November 2012; accepted 12 December 2012; published online 9 January 2013)

In recent years, emission spectroscopy has been applied to the study of post-detonation combustion in explosives, often yielding valuable information on temperatures and chemical dynamics. The post-detonation fireballs that form as under-oxidized detonation products burn in the surrounding air are optically dense and the corresponding emission spectra sample only the material at or near the surface of the fireball. In the present study, we exploit the large optical density in order to probe the dynamics occurring in the interior of the fireball. Emission spectra are collected following detonation of 20 g aluminized Hexahydro-1,3,5-trinitro-1,3,5-triazine (RDX) charges using fiber optics located behind the flame front and then compared with the corresponding spectra of the surface layer collected from outside the fireball. We find that in the early evolution of the fireball ($t \leq 60\,\mu s$ and $r \leq 10$ cm in the current study), combustion and light emission are predominantly confined to the surface, while the interior is dark. Later, after the fireball expands and mixes with the surrounding air ($t \geq 120\,\mu s$ or $r \geq 30$ cm), combustion and emission occur throughout, and we find no significant differences between the spectra collected from the interior of the fireball versus those from its surface. © *2013 American Institute of Physics*. [http://dx.doi.org/10.1063/1.4774029]

I. INTRODUCTION

Understanding energy release processes and their associated kinetics is of fundamental importance for the study of explosives. A comprehensive understanding of the energy release requires knowledge not only of the time-dependent pressure and temperature in the system but also of the chemical dynamics in the evolving system. Identifying important chemical species (including transients) and tracking their evolution through time can greatly expand our ability to model and perhaps even control energy release.

Measurements of the energy release process of explosives are made difficult by the fast timescales involved in the reaction. For gram-scale samples, detonation is typically completed within several microseconds. Subsequent afterburning of under-oxidized detonation products can then result in a post-detonation fireball that can persist for several milliseconds.[1] Measurement options are further limited by the high temperatures and pressures present during these events since most sensors rugged enough to survive the explosive cannot provide a response fast enough to follow its dynamics. Spectroscopy methods are considered to be a very attractive approach to the study of these systems. Spectroscopy techniques have been extensively employed to study flames[2] and plasmas,[3] yielding a large body of work with which to compare. Additionally, spectroscopy can be used to study very fast processes, and spectra can be collected at a distance from the explosion. A number of studies utilizing spectroscopy in the visible, near-IR, and IR to study explosions have now been reported in recent years.[4–12] Depending upon the technique employed, spectroscopy data can be used to obtain temperature measurements, chemical dynamics data, or both.

One important aspect of the spectroscopy of explosions has been that of the opacity of the fireball. The results of several investigations have suggested that fireballs are optically thick for at least some of their evolution.[13–17] More recently, the opacity has been quantified[18] as a function of space and time for aluminized explosives, with characteristic attenuation depths on the order of millimeters for its early evolution and centimeters for the remainder of its lifetime for which significant luminosity is observed. This work clearly establishes (at least for gram-scale and larger samples) that emission spectra collected from post-detonation combustion correspond to the conditions near the surface of the fireball but raises other important questions regarding what is occurring in the interior of the fireball and how it is different than the surface dynamics. The purpose of the current study is to exploit the large optical density in order to probe the dynamics occurring in the interior of the fireball. Time-resolved emission spectra are collected from fiber optics located behind the flame front and then compared with the corresponding spectra of the surface layer collected from fiber optics positioned outside the fireball.

II. EXPERIMENT

The experiment is depicted schematically in Figure 1. Pressed right-cylindrical charges of 20 g total mass were prepared from a mixture of RDX (73 wt. %), a hydroxyl-terminated polybutadiene (HTPB) binder (6 wt. %), and

a)Author to whom correspondence should be addressed. Electronic mail: wlewis2@udayton.edu.

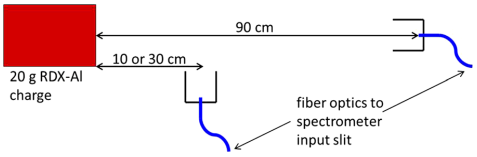

FIG. 1. Schematic representation of the experiment. The cylindrical explosive charges (20 g total mass) consisted of 20 wt. % aluminum nanoparticles in RDX. Light from the expanding fireball was collected by 600 μm core-diameter fiber optics placed relative to the charge as shown (diagram not to scale). The ends of the fibers were enclosed in black cylindrical cups (25 mm width, 25 mm height) in order to limit the field of view.

aluminum nanoparticles (20 wt. %). The aluminum nanoparticles were purchased from Nano Technologies (30–70 nm particle size). In order to obtain temperature measurements, 1 wt. % ball-milled barium nitrate was added to the mixture and mixed thoroughly before pressing. The resulting Ba atomic emission lines can be used to measure the apparent temperature of the flame as demonstrated previously.[11,12] The charges were detonated from the left side using Reynolds RP-80 detonators placed on the end of each cylindrical charge. Note that in the current investigation, detonation should be complete within 5 μs of detonator initiation given the length of the charge (25 mm) and the detonation velocity of the formulation (~7.5 km/s), with subsequent emission assigned to the post-detonation fireball resulting from afterburning of under-oxidized detonation products.

Light from the explosions was collected using 600 μm core-diameter fiber optics (Ocean Optics, 38 m total length) as shown in Figure 1. The bare end of the fiber optic was placed inside a black cylindrical cup (25 mm width × 25 mm height) in order to limit the field of view. The fiber optic was then placed 10, 30, or 90 cm from the right face of the charge. At 10 or 30 cm, the fiber was positioned vertically with no line-of-sight to the charge. At 90 cm, the fiber was placed horizontally to directly view the explosive sample. Light from the fiber optics was sent to spectrograph located in a shielded observation room several meters away from the explosive charge. The spectrograph was constructed from a 1/8 m spectrometer (Oriel) interfaced to a 4096 pixel line-scan camera (Basler Sprint) with a data collection rate of 1–70 kHz. The resolution and usable spectral range of the spectrograph were 1.2 nm and 380–760 nm, respectively. The wavelength and intensity of the spectrograph were calibrated with a mercury-argon lamp (Ocean Optics) and a halogen lamp with a known color-temperature (Thorlabs). We note that due to the low light intensity of the color-temperature lamp in the blue region of the spectrum and the short maximum integration time of the spectrograph (1 ms), the spectrum could not be corrected for instrument response below ~460 nm. The spectrograph was triggered by the fire control circuits used to detonate the explosive charges. Spectra were recorded at an integration period of 15 μs per scan. Each shot was repeated several times in order to confirm reproducibility, and the light transmission of the fiber optic was checked after each shot. Damaged fibers were replaced prior to firing the next shot as necessary.

III. RESULTS AND DISCUSSION

In Figure 2(a), we show a typical data set for the horizontal fiber located at 90 cm. This fiber optic collects light from the outermost surface layers of the fireball during its evolution. Consistent with our earlier measurement,[12] for the first 15 μs following the start of detonation, little light is observed. Subsequent scans (later delay times) contain Al $^2P_{1/2} \leftarrow {}^2S_{1/2}$ and $^2P_{3/2} \leftarrow {}^2S_{1/2}$ atomic emissions at 394 and 396 nm, respectively,[19,20] the AlO $X \leftarrow B$ emission band[21] from 435 to 545 nm, and a large broadband emission. Observation of Al atomic emission peaks, the AlO vibronic band, and a broadband emission is typical of aluminum combustion.[22–26] At later times, the Al and AlO emissions begin to fade away as the early-time free/gaseous Al combustion

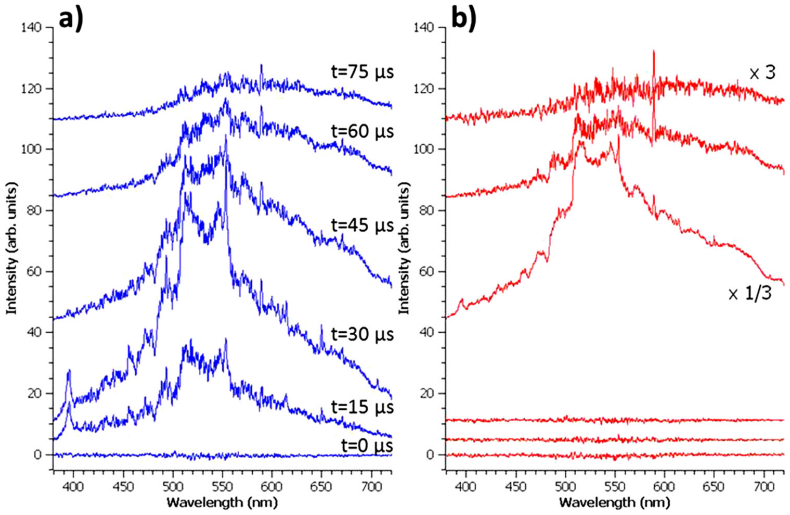

FIG. 2. Time-resolved emission spectra obtained from detonation of 20 g charges of RDX containing 20 wt. % aluminum nanoparticles. The charges were doped with 1 wt. % barium nitrate. Spectra in (a) were collected from the fiber optic located at 90 cm, facing the explosive charge. Delay times relative to the detonator signal are indicated. Spectra in (b) were obtained from the fiber optic at 10 cm, which faced upwards. Delays for each vertically shifted spectrum are the same as in (a). In both sets, a large broadband emission is evident. Superimposed upon the broadband are Al atomic emission lines found at 394 and 396 nm, an AlO vibronic band from 435 to 545 nm, and a Na atomic emission at 589 nm. Ba and Ba^+ lines are found at 455, 493, 554, 614, 650, and 706 nm. All spectra are plotted on the same intensity scale. Two of the spectra in (b) were rescaled as marked.

TABLE I. Apparent temperatures obtained from the Ba atomic emission lines. Estimated errors at the 95% confidence level are given in parentheses.

Time (μs)	Fiber at 10 cm	Fiber at 90 cm
0	…	…
15	…	4000 (500)
30	…	3900 (400)
45	4000 (200)	…

processes halt, leaving only a broadband emission from hot particulates.[12] In several of the scans, we also see a Na emission at 589 nm resulting from Na impurities[27] in the sample, as well as peaks at 554 nm and 706 nm due to the $^1S_0 \leftarrow {}^1P_1$ and $^3D_3 \leftarrow {}^3F_4$ transitions in Ba atoms, and peaks at 455, 493, and 614 nm from the $^2S_{1/2} \leftarrow {}^2P_{3/2}$, the $^2S_{1/2} \leftarrow {}^2P_{1/2}$, and the $^2D_{5/2} \leftarrow {}^2P_{3/2}$ transitions in Ba^+ ions, respectively.[28] The peak at 650 nm may have contributions[28] from both Ba ($^3D_3 \leftarrow {}^3D_3$) and Ba^+ ($^2D_{3/2} \leftarrow {}^2P_{1/2}$) at the resolution of the spectrograph.

In Figure 2(b), we see the signals recorded from the vertical fiber optic placed at 10 cm. In the first three scans, corresponding to times prior to arrival of the flame front at the fiber, no light is collected. In the scan beginning at 45 μs, the flame front has arrived at the fiber and a large signal is observed. Light is also collected during subsequent scans, corresponding to luminescence from material in the interior of the fireball. It is interesting to compare these spectra with those collected from outside the fireball, shown in Figure 2(a). We see that once the flame front has arrived and the swept over the fiber, the spectra collected are remarkably similar to those in Figure 2(a), although the absolute intensities differ. The peaks and bands observed in the spectra in Figure 2(a), the underlying broadband emissions, and the general contours of the spectra are all reproduced in the spectra in Figure 2(b), albeit with a different signal-to-noise ratio. The apparent temperatures of the flame (calculated from the Ba atomic emission lines[11,12]) are also similar and are shown in Table I. Regardless of which fiber optic is used to collect the spectrum, the apparent temperature of the spectrum is in the vicinity of 4000 K, in excellent agreement with earlier measurements.[12]

When the fiber is moved to 30 cm from the explosive charge, a similar behavior is observed. In Figure 3, we show the spectra collected from the vertical fiber at this position as well as the analogous spectra from the horizontal fiber at 90 cm. In Figure 3(a), we see the spectra from the fiber at 90 cm beginning at t = 105 μs. By this time, free/gaseous Al combustion has ceased and the fireball has begun to cool;[12] the broadband emission and a Na line at ~589 nm are the only spectral features remaining. In subsequent spectra, these too fade in intensity. Unfortunately, the fireball is not sufficiently hot at this point to efficiently populate the upper Ba energy levels and permit a temperature measurement. Turning our attention to Figure 3(b), we find an empty spectrum at t = 105 μs. Actually, a very small contribution may be present at ~550 nm, although it is difficult to be certain given the noise level in this region. All spectra collected from the fiber prior to this time are simply blank. In the spectra obtained at 120 μs and later, we observe a broadband emission and the Na line as the flame front arrives and passes over the fiber. A comparison of the spectra in Figure 3(a) with those in Figure 3(b) reveals that once again the two sets of spectra are quite similar.

At first glance, the fact that the normalized spectra collected from inside and outside the fireball are consistently comparable to one another would seem to imply that the dynamics inside the fireball are also comparable to those near its surface. Hence, any spectra collected from outside might be regarded as representative of the overall dynamics. This impression is misleading, however, since it fails to account for the differences in the absolute spectral intensities. In Figure 2, we find that the ratios of the absolute intensities of the spectra in Figure 2(a) to those in Figure 2(b) are not constant. The spectrum at t = 45 μs in Figure 2(b) is approximately a factor of 3 more intense than the corresponding spectrum in Figure 2(a). At t = 60 μs, however, the spectrum in Figure 2(b) is of comparable intensity to that in Figure 2(a). And at 75 μs, the spectrum in Figure 2(b) is now a factor of 3 weaker than that in Figure 2(a). Subsequent spectra become yet weaker. On the other hand, in Figure 3, we find that the absolute intensities of the spectra in Figure 3(a) and those in 3(b) (at least once the flame arrives at the fiber) are always

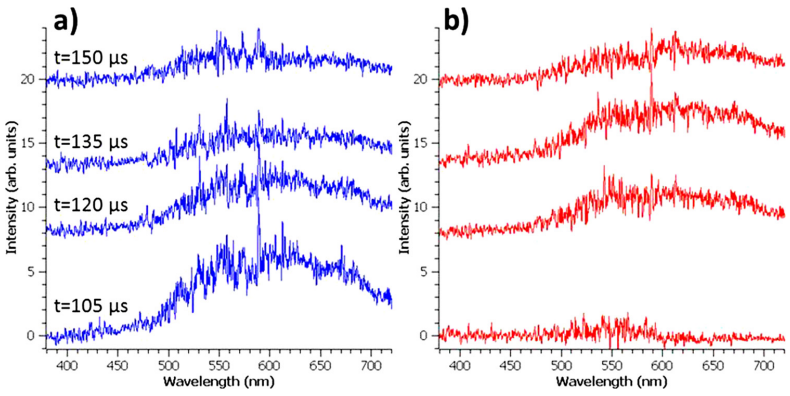

FIG. 3. Time-resolved emission spectra obtained from detonation of 20 g charges of RDX containing 20 wt. % aluminum nanoparticles and doped with 1 wt. % barium nitrate. Spectra in (a) were collected from the fiber optic located at 90 cm. Spectra in (b) were obtained from the fiber optic at 30 cm. Delay times are indicated relative to the detonator signal. All spectra are plotted on the same intensity scale.

comparable. This is in direct contrast to the trend we observed in Figure 2.

We know that following detonation, expansion of the fireball will change its composition as the detonation products mix with the surrounding air. At some point in its early evolution, the under-oxidized detonation products that constitute the fuel for the fireball will be primarily located behind the flame front. During such time, combustion would take place predominantly near the surface of the fireball as the hot fuel and air combine there, with little reaction possible in the interior due to lack of oxygen. If this is the case, we would expect the spectrum to be quite bright when the flame front arrives at the fiber and much less intense when the fiber is located behind the advancing flame front. This is precisely what we observe from the fiber located at 10 cm. At some point later in the evolution of the fireball, it will have expanded and mixed the hot fuels inside with surrounding air, and we would expect combustion to occur throughout. Hence, we would no longer expect the spectrum collected from a stationary point in the interior to rapidly weaken as the flame front advances. This is indeed what we observe from the fiber at 30 cm. Note that by the time the flame front reaches this fiber, the volume of the fireball has increased by a factor of $\sim$27 compared to when it passed the fiber at 10 cm.

The fact that the normalized emission spectrum (and apparent temperatures) obtained from the fiber optics placed inside is virtually identical to those obtained from outside the fireball is also consistent with this hypothesis. In the early time evolution, they agree simply because the surface of the fireball is the only region undergoing combustion and light emission. In the late time, the fireball is well-mixed, and there should be little difference between the chemistry occurring in the interior and that near the surface. Thus, the respective emission spectra should again be consistent with one another.

IV. CONCLUSIONS

Taken together, the results of the present investigation suggest that while emission spectra collected from the surface of the fireball may be regarded as representative of the ongoing combustion processes in the fireball, they should not be taken as representative of the environment throughout until several volume expansions have occurred. Our data suggest that early time combustion processes (and light emission) are predominantly confined to the material near the surface, while the interior is dark. For the 20 g RDX/Al charges studied, this seems to be the case for $t \leq 60\ \mu s$ and $r \leq 10$ cm. Once the fuel in the fireball is well-mixed with the surrounding air, combustion appears to occur throughout, and we find no significant differences between the spectra collected from the interior of the fireball versus those from its surface. In the present study, this corresponds to $t \geq 120\ \mu s$ or $r \geq 30$ cm. In future work, it may be possible to utilize absorption spectroscopy to sample the apparently non-combusting material behind the early-time flame front and to quantify the presumably cooler conditions there.

ACKNOWLEDGMENTS

The authors gratefully acknowledge funding and facilities provided for this work by the Air Force Research Laboratory under the NanoEnergetics Program. We would like to thank Mr. Rick Beesley and Mr. Mark Grimmonpre for their assistance in conducting these experiments.

[1]P. W. Cooper, *Explosives Engineering* (Wiley-VCH, 1996).
[2]A. G. Gaydon, *The Spectroscopy of Flames* (John Wiley & Sons, 1957).
[3]K. C. Lapworth, J. Phys. E: Sci. Instrum. **7**, 413 (1974).
[4]J. R. Carney, J. S. Miller, J. C. Gump, and G. I. Pangilinan, Rev. Sci. Instrum. **77**, 063103 (2006).
[5]J. Wilkinson, J. M. Lightstone, C. J. Boswell, and J. R. Carney, in *Shock Compression of Condensed Matter*, edited by M. Elert, M. D. Furnish, R. Chau, N. Homes, and J. Nguyen (American Institute of Physics, 2007), p. 1271.
[6]V. Bouyer, G. Baudin, C. Le Gallic, and P. Hervé, in *Shock Compression of Condensed Matter*, edited by M. D. Furnish, N. N. Thadhani, and Y. Horie (American Institute of Physics, 2001), p. 1223.
[7]V. Bouyer, I. Darbord, P. Hervé, G. Baudin, C. Le Gallic, F. Clément, and G. Chavent, Comb. Flame **144**, 139 (2006).
[8]J. A. Orson, W. F. Bagby, G. P. Perram, Infrared Phys. Technol. **44**, 101 (2003).
[9]K. C. Gross, J. Wayman, and G. P. Perram, Proc. SPIE **6566**, 656613 (2007).
[10]J. D. Koch, S. Piecuch, J. M. Lightstone, J. R. Carney, and J. Hooper, J. Appl. Phys. **108**, 036101 (2010).
[11]W. K. Lewis and C. G. Rumchik, J. Appl. Phys. **105**, 056104 (2009).
[12]W. K. Lewis, C. G. Rumchik, P. B. Broughton, and C. M. Lindsay, J. Appl. Phys. **111**, 014903 (2012).
[13]P. Persson, B. Andersson, and S. Stahl, "A technique for detailed time-resolved radiation measurements in the reaction zone of condensed explosives," in *4th International Symposium on Detonation, Silver Spring, MD* (U.S. Navy Office of Naval Research, 1965), p. 602.
[14]K. C. Gross, G. P. Perram, and R. F. Tuttle, Proc. SPIE **5811**, 100 (2005).
[15]J. R. Carney and J. Wilkinson, "Atmospheric effects on time-resolved emission measurements of detonation and combustion products," in *13th International Detonation Symposium, Norfolk, VA*, 2006.
[16]V. Bouyer, G. Baudin, C. Le Gallic, I. Darbord, and P. Hervé, "Temperature profile calculation from emission spectroscopy measurements in nitromethane submitted to plate impacts," in *12th International Detonation Symposium, San Diego, CA* (U.S. Navy Office of Naval Research, 2002), p.743.
[17]J. R. Carney, J. M. Lightstone, T. P. McGrath II, and R. J. Lee, Propellants, Explos., Pyrotech. **34**, 331 (2009).
[18]J. M. Peuker, P. Lynch, H. Krier, and N. Glumac, Opt. Lasers Eng. **47**, 1009 (2009).
[19]K. B. S. Eriksson and H. B. S. Isberg, Ark. Fys. **23**, 527 (1963).
[20]C. Mendoza, W. Eissner, M. Le Dourneuf, and C. J. Zeippen, J. Phys. B **28**, 3485 (1995).
[21]R. W. B. Pearse and A. G. Gaydon, *The Identification of Molecular Spectra* (Chapman and Hall, London, 1963).
[22]J. L. Gole and R. N. Zare, J. Chem. Phys. **57**, 5331 (1972).
[23]S. Rosenwaks, R. E. Steele, and H. P. Broida, J. Chem. Phys. **63**, 1963 (1975).
[24]S. Goroshin, J. Mamen, A. Higgins, T. Bazyn, N. Glumac, and H. Krier, Proc. Combust. Inst. **31**, 2011 (2007).
[25]M. Jackson, M. Pantoya, and W. Gill, Combust. Flame **153**, 58 (2008).
[26]P. Escot Bocanegra, D. Davidenko, V. Sarou-Kanian, C. Chauveau, and I. Gökalp, Exp. Therm. Fluid Sci. **34**, 299 (2010).
[27]*CRC Handbook of Chemistry and Physics*, 80th ed., edited by D. R. Lide (CRC, Boca Raton, 2000).
[28]J. J. Curry, J. Phys. Chem. Ref. Data **33**, 725 (2004).

JOURNAL OF APPLIED PHYSICS **113**, 044907 (2013)

Comparison of post-detonation combustion in explosives incorporating aluminum nanoparticles: Influence of the passivation layer

W. K. Lewis,[1,a)] C. G. Rumchik,[2] M. J. Smith,[3] K. A. S. Fernando,[1] C. A. Crouse,[4,5] J. E. Spowart,[4] E. A. Guliants,[1] and C. E. Bunker[3]
[1]*University of Dayton Research Institute, Dayton, Ohio 45469, USA*
[2]*U.S. Air Force Research Laboratory, Munitions Directorate, Eglin AFB, Florida 32542, USA*
[3]*U.S. Air Force Research Laboratory, Propulsion Directorate, Wright-Patterson AFB, Ohio 45433, USA*
[4]*U.S. Air Force Research Laboratory, Materials & Manufacturing Directorate, Wright-Patterson AFB, Ohio 45433, USA*
[5]*UES, Inc., Dayton, Ohio 45432, USA*

(Received 7 December 2012; accepted 17 January 2013; published online 31 January 2013)

Aluminum nanoparticles and explosive formulations that incorporate them have been a subject of ongoing interest due to the potential of aluminum particles to dramatically increase energy content relative to conventional organic explosives. We have used time-resolved atomic and molecular emission spectroscopy to monitor the combustion of aluminum nanoparticles within the overall chemical dynamics of post-detonation fireballs. We have studied the energy release dynamics of hexahydro-1,3,5-trinitro-1,3,5-triazine (RDX) charges incorporating three types of aluminum nanoparticles: commercial oxide-passivated nanoparticles, oleic acid-capped aluminum nanoparticles (AlOA), and nanoparticles in which the oxide shell of the particle has been functionalized with an acrylic monomer and copolymerized into a fluorinated acrylic matrix (AlFA). The results indicate that the commercial nanoparticles and the AlFA nanoparticles are oxidized at a similar rate, while the AlOA nanoparticles combust more quickly. This is most likely due to the fact that the commercial nano-Al and the AlFA particles are both oxide-passivated, while the AlOA particles are protected by an organic shell that is more easily compromised than an oxide layer. The peak fireball temperatures for RDX charges containing 20 wt. % of commercial nano-Al, AlFA, or AlOA were ~3900 K, ~3400 K, and ~4500 K, respectively. © *2013 American Institute of Physics*. [http://dx.doi.org/10.1063/1.4790159]

I. INTRODUCTION

Aluminum nanoparticles and explosive formulations that incorporate them have been a subject of significant interest in recent years due to the potential of aluminum particles to dramatically increase energy content relative to conventional organic explosives. To date, a large number of aluminized explosive formulations have been studied, as summarized in several reviews.[1,2] In general, it has been found that oxide-passivated aluminum nanoparticles particles react slowly relative to detonation processes and contribute primarily to "late-time effects" such as post-detonation fireball combustion and air blast[1] due to the high melting point[3] (2054 °C) and mechanical strength of the oxide shell that protects the aluminum metal core from oxidation. Since the properties of the passivation layer are thought to exert an important influence on the post-detonation chemistry, it seems reasonable to suspect that changing the nature of this layer might significantly influence the chemical dynamics.

In recent years, synthesis methods have been developed to produce aluminum nanoparticles which are passivated by an organic layer[4,5] rather the traditional oxide shell. Alternatively, synthesis routes to particles in which a pre-existing oxide layer is functionalized with various organic species have also been discovered.[6,7] We have previously synthesized[5] aluminum nanoparticles capped with oleic acid and characterized their reactivity.[8,9] In these particles, the organic shell is lost at temperatures of 200–300 °C, exposing the reactive core. These particles have also exhibited significantly enhanced reactivity with room temperature water,[8] as well as with ammonium nitrate and ammonium perchlorate matrices and their decomposition products after heating.[9]

The purpose of the current investigation is to study the post-detonation combustion dynamics of hexahydro-1,3,5-trinitro-1,3,5-triazine (RDX) charges incorporating three types of aluminum nanoparticles: commercial oxide-passivated nanoparticles, the oleic acid-capped aluminum nanoparticles (AlOA), and nanoparticles in which the pre-existing oxide shell of the aluminum particle has been functionalized[7] with an acrylic monomer and copolymerized in the presence of a fluorinated acrylate to yield an aluminum-fluorinated acrylic composite material (AlFA). The fluorocarbons in this material have been shown to vigorously react with the Al metal to produce AlF_3 and Al_4C_3 once ignited.[7] Reaction with O_2 in the surrounding air to produce Al_2O_3 also occurs (the material is fuel-rich), but the fluorination reaction is kinetically dominant, making this an intriguing candidate to also study in explosive formulations.

The progress of the post-detonation chemistry is tracked using atomic and molecular emission spectroscopy methods.

[a)]Author to whom correspondence should be addressed. Electronic mail: wlewis2@udayton.edu.

Temperatures are obtained using a previously developed atomic emission spectroscopy-based technique[10,11] which involves doping the explosive charge with an inorganic impurity. The temperature is then determined by monitoring the relative intensities of atomic emission lines corresponding to emission from different energy levels of a selected atom. Chemical dynamics are tracked via the time-dependent intensities of electronic emissions from species of interest, such as Al atomic lines and AlO vibronic bands. By combining temperature measurements with the time-resolved emission spectroscopy methods used by earlier groundbreaking investigations[12–18] to characterize the complex chemical dynamics occurring after the detonation of an explosive charge, we are able to monitor the combustion of aluminum particles within the overall chemical dynamics of the explosion and correlate this with the energy release process. We have successfully used this approach to study RDX charges incorporating nano- and micron-sized aluminum particles previously.[11]

II. EXPERIMENT

Pressed right-cylindrical charges (25 mm height × 25 mm diameter) of 20 g total mass were prepared from a mixture of RDX (73 wt. %), a hydroxyl-terminated polybutadiene (HTPB) binder (6 wt. %), and an aluminum powder (20 wt. %) chosen from commercial nano-Al, AlOA, or AlFA. In order to obtain temperature measurements during the post-detonation combustion via atomic emission spectroscopy, 1 wt. % ball-milled barium nitrate was added to the mixture and mixed thoroughly before pressing. Oxide-passivated nanoparticles (30–70 nm particle size) were obtained from Nano Technologies; the AlOA (20–70 nm particle sizes) and AlFA samples were synthesized as reported previously.[5,7] The AlFA material consisted of micron–sized particles containing oxide-passivated aluminum nanoparticles (30–130 nm size) polymerized into a fluorinated acrylic matrix. We note that the commercial nano-Al is ~80 wt. % active Al metal content. The AlOA particles are ~40 wt. % active Al; the AlFA particles are ~50 wt. % active Al. All charges were initiated using Reynolds RP-80 detonators placed on the end of each cylindrical charge.

Light from the explosions was collected from the end of the charge opposite the detonator using a 5 mm diameter collection lens mounted to the end of a 1000 μm core-diameter fiber optic (Ocean Optics). The collection optics were in a shielded observation room located several meters away from the explosive charge. The collection optic were aligned to view the center of each charge through a BK7 glass viewport. The collected light was sent to a time-resolved emission spectrograph constructed from a 1/8 m spectrometer (Oriel) interfaced to a 4096 pixel line-scan camera (Basler Sprint) with a data collection rate of 1–70 kHz. The resolution and usable spectral range of the spectrograph were 1.2 nm and 380–720 nm, respectively. The wavelength and intensity axes of the spectrograph were calibrated with a mercury-argon lamp (Ocean Optics) and a halogen lamp with a known color-temperature (Thorlabs), respectively. We note that due to the low light output of the color-temperature lamp in the blue region of the spectrum and the short maximum integration time of the detector (1 ms), the spectrum intensity could not be corrected for instrument response at wavelengths below ~460 nm. The spectrograph was triggered by the fire control circuits used to detonate the explosive charges. Spectra were recorded at an integration period of 15 μs per scan and each shot was repeated several times in order to confirm reproducibility.

We note that in the current investigation, detonation should be complete within ~5 μs of detonator initiation given the length of the charge and the detonation velocity of the formulation, with subsequent emission assigned to the post-detonation fireball resulting from afterburning of under-oxidized detonation products. Interestingly, spectroscopy methods similar to those used in the current study have observed very high temperatures (9700 K) associated with early ($t \leq 21$ μs) shock breakout into the surrounding air by monitoring atomic emission signals from N and O atoms.[16] We do not expect breakout effects to contribute significantly to the results of the current study on account of the longer delay times and the fact that our temperature measurements are obtained from an atom found in the explosive formulation but not in the surrounding air.

III. RESULTS AND DISCUSSION

In Figure 1, we show typical emission spectra collected from RDX charges incorporating the commercial nano-Al, AlOA, and AlFA. Each spectrum shown was collected at $t = 30$ μs, where $t = 0$ corresponds to explosion of the detonator. The spectra are remarkably similar; in each we find a broadband emission covering the entire visible spectrum, Al $^2P_{1/2} \leftarrow {}^2S_{1/2}$ and $^2P_{3/2} \leftarrow {}^2S_{1/2}$ atomic emissions at 394 and 396 nm, respectively,[19,20] and the AlO $X \leftarrow B$ vibronic band.[21] We also see a strong Na emission at 589 nm resulting from Na impurities[3] in the sample, as well as peaks at 554 nm and 706 nm due to the $^1S_0 \leftarrow {}^1P_1$ and $^3D_3 \leftarrow {}^3F_4$ transitions in Ba atoms, and peaks at 455, 493, and 614 nm from the $^2S_{1/2} \leftarrow {}^2P_{3/2}$, the $^2S_{1/2} \leftarrow {}^2P_{1/2}$, and the $^2D_{5/2} \leftarrow {}^2P_{3/2}$ transitions in Ba^+ ions, respectively.[22] The peak at 650 nm may have contributions[22] from both Ba ($^3D_3 \leftarrow {}^3D_3$) and Ba^+ ($^2D_{3/2} \leftarrow {}^2P_{1/2}$) at the resolution of the spectrograph. In the case of the charges incorporating AlOA, we also see intense Li lines at 610 nm and 671 nm, due to a Li impurity. A number of smaller unassigned peaks and bands are also found throughout the spectra. Unfortunately, no AlF vibronic bands were observed for the RDX-AlFA charges, possibly due to the weak emission character of the AlF bands found in this region of the spectrum.[21] We note that additional AlF bands have been reported[21] at wavelengths outside the spectral range of our spectrometer, and future experiments are planned to focus on any UV emissions.

Although the spectra share the same basic features, the time-dependence of the Al, AlO, and broadband emissions differs between the charges containing the various types of aluminum particles. In Figure 2, we show the intensity of the Al atomic emission and the broadband emission as measured at 600 nm as a function of time. Unfortunately, the AlO band intensities could not be readily extracted and plotted due to

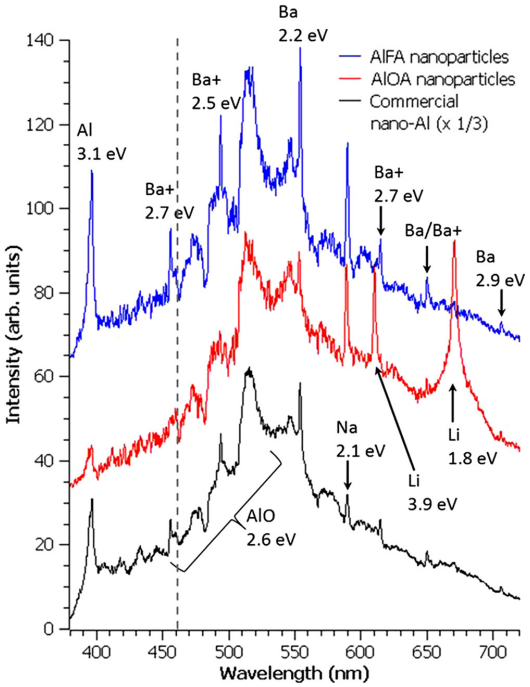

FIG. 1. Emission spectra obtained from detonation of barium-doped 20 g RDX charges containing 20 wt. % aluminum nanoparticles chosen from commercial nano-Al (bottom spectrum), AlOA (middle spectrum), or AlFA (top spectrum). All spectra were captured at $t = 30\,\mu s$ relative to the start of detonation. Prominent peaks and bands are labeled with the identity of the emitting species and the energy of the upper electronic state involved in the transition. The spectra are corrected for instrument response at wavelengths to the right of the vertical dashed line ($\lambda \geq 460$ nm).

the overlapping broadband emission in this region of the spectrum. Nevertheless, visual inspection of the spectra for the various charges as a function of time confirmed that the Al and AlO signals occurred in coincidence, as is typical during Al combustion.[23–27] In Figure 2(a), we see that for the RDX-AlOA charges, the Al atomic emission lines are strongest in the scan obtained at $t = 15\,\mu s$ and then decrease in each subsequent scan. In contrast, the RDX charges containing commercial nano-Al or AlFA exhibit little Al or AlO emission until $t = 30\,\mu s$. The time-dependence of the Al lines in these two types of charges is virtually identical. The intensity of the broadband emissions shows a similar trend. Strong broadband emissions are typically observed during Al combustion,[23–27] but we must be cautious in the interpretation of this signal since it can also be produced by particulates such as soot. In Figure 2(b), we see that the charges incorporating commercial nano-Al or AlFA again behave similarly to one another, while the evolution of the signals from the RDX-AlOA charges is shifted to somewhat earlier times. Taken at face value, the data in Figure 2 seem to indicate that combustion of the AlOA particles within the post-detonation fireball occurs on a faster timescale than either the commercial nano-Al or AlFA, and that the timescale for oxidation of the latter two particles is quite similar. If indeed this is the case, we might expect to see some evidence of this in the fireball temperatures. Temperature measurements are particularly relevant for the AlFA material, since it may be possible for the aluminum nanoparticles to react exothermically with the fluorinated acrylic matrix before competing oxidation processes can occur,[7] increasing the temperature, but producing only weak AlF vibronic signals, for example.

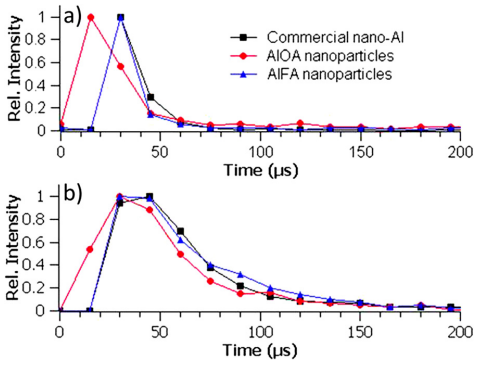

FIG. 2. Time dependence of (a) the Al atomic emission peak at 396 nm and (b) the broadband emission at 600 nm for each of the types of explosives charges studied following detonation.

In Table I, we list the apparent temperatures of the fireballs obtained from the Ba atomic emissions. The temperatures were obtained by the two-line method, utilizing the 554 and 706 nm Ba emission lines since they persisted longest following the detonations. Unfortunately, Ba emission lines were not reliably prominent in the first 1–2 scans (0, 15 μs). The error in the temperatures obtained in subsequent scans was determined by the available signal-to-noise ratio of the Ba peaks in the spectra, with higher Ba signals corresponding to lower error bars. The error bars listed in Table I correspond to either the 95% confidence level calculated from the signal-to-noise ratio of the scan or the inherent accuracy limit of the method,[28] whichever is larger. As mentioned above, each shot was repeated several times to confirm reproducibility. The temperature of the fireball resulting from the RDX charges containing the commercial nano-Al are in the range of 3600–3900 K, in good agreement with earlier measurements.[11] The temperature obtained for the RDX-AlOA charges is initially in the 4000–4500 K range, but then quickly drops to less than 2600 K for $t \geq 45\,\mu s$. We

TABLE I. Apparent fireball temperatures for the various types of explosives charges used in the current study, obtained from Ba atomic emission lines evident in the time-resolved spectra. The temperature was calculated by the two-line method using the Ba emission peaks at 554 and 706 nm. The 95% confidence levels are given in parentheses.

Time (μs)	20 wt. % commercial Al in RDX	20 wt. % AlOA in RDX	20 wt. % AlFA in RDX
0	…	…	…
15	…	4000 (400)	…
30	3900 (200)	4500 (500)	3200 (300)
45	3600 (300)	<2600	3400 (500)

can estimate only an upper bound for this temperature based upon the presence of the Ba line at 554 nm and the absence of any other Ba or Ba^+ lines in the corresponding spectrum. The temperatures obtained for the RDX-AlFA charges are in the range of 3200–3400 K. It is interesting to note that this is near the expected temperature for aluminum fluorination reactions,[29] although this may be coincidental since these particles are fuel-rich and we know from the emission spectra that oxidation is also occurring. For reference, the apparent temperatures of RDX charges that contain no Al content (obtained previously[10,11] using the same methodology) are in the range of 2600–2900 K.

We note that two Li lines from different energy levels are observed in the RDX-AlOA spectra, resulting from a Li impurity in AlOA. Unfortunately, we cannot use these to obtain an additional temperature measurement since the peak at 671 nm oversaturated the detector in the as-collected spectra (before correction for detector response was applied). The prominent pedestal at the base of this peak is most likely due to charge "bleeding" from the oversaturated pixels into neighboring ones. Additionally, the Li concentration in the sample is currently unknown, thus, we cannot be certain that the Li emissions are not subject to self-absorption effects.

The fact that the temperatures obtained for the RDX-AlOA charges is similar to (or perhaps even a bit higher than) those of the charges with commercial nano-Al, while the RDX-AlFA charges yielded lower temperatures, is consistent with the observed oxidation kinetics discussed above, i.e., that the oxidation timescales are similar for the commercial nano-Al and AlFA but that the AlOA particles burn more quickly. The AlOA and AlFA particles contain ~40 wt. % and ~50 wt. % Al metal, respectively,[5,7] only about half of the Al metal content of the commercial particles. The lower percentage of Al metal content correspondingly lowers the energy content of the explosive charge. Consequently, if the AlFA particles burn at a similar rate to the commercial nano-Al, then we would expect the temperature to be intermediate between that of RDX alone and RDX with the commercial nanoparticles. This is precisely what we observe. On the other hand, the observation that the RDX-AlOA charges are able to achieve a peak temperature at least equal to that of RDX with the commercial nanoparticles, despite the substantially lower Al content, lends additional support to the idea that the combustion kinetics for the AlOA particles are faster than those for the other particles studied. Of course, the fact that the temperature drops so quickly for the charges incorporating the AlOA particles also supports this idea.

IV. CONCLUSIONS

The results of the current investigation seem to indicate that the AlOA nanoparticles react more quickly in the fireball than either the commercial nano-Al or the AlFA nanoparticles even though the nanoparticle sizes in the samples are comparable. It also indicates that the oxidation rates of the commercial nano-Al and the AlFA particles (or at least the Al content in the AlFA material) are similar. Clearly, additional experimental investigations and possibly also input from theory will be required to establish a detailed mechanistic understanding. Nevertheless, the most straightforward interpretation of these results would seem to be that changing the passivation layer of aluminum nanoparticles from an oxide shell to organic passivation can significantly enhance the post-detonation combustion kinetics.

ACKNOWLEDGMENTS

The authors gratefully acknowledge funding and facilities provided for this work by the Air Force Research Laboratory under the NanoEnergetics Program, funding from the Air Force Office of Scientific Research (AFOSR) through the support of Dr. Michael Berman, and the financial support of the Defense Threat Reduction Agency (DTRA, Grant No. HDTRA-07-1-0026) for development of the AlOA particles. We would also like to thank Mr. Rick Beesley and Mr. Mark Grimmonpre for their assistance in conducting these experiments.

[1]P. P. Vadhe, R. B. Pawar, R. K. Sinha, S. N. Asthana, and A. S. Rao, Combust., Explos. Shock Waves **44**, 461 (2008).
[2]E. Anderson, *Tactical Missile Warheads*, Progress in Astronautics and Aeronautics Vol. 155, edited by J. Carleone (American Institute of Aeronautics and Astronautics, Washington, 1993), Chap. 2.
[3]*CRC Handbook of Chemistry and Physics*, 80th ed., edited by D. R. Lide (CRC, 2000).
[4]R. J. Jouet, A. D. Warren, D. M. Rosenberg, V. J. Bellitto, K. Park, and M. R. Zachariah, Chem. Mater. **17**, 2987 (2005).
[5]K. A. S. Fernando, M. J. Smith, B. A. Harruff, W. K. Lewis, E. A. Guliants, and C. E. Bunker, J. Phys. Chem. C **113**, 500 (2009).
[6]C. A. Crouse, C. J. Pierce, and J. E. Spowart, ACS Appl. Mater. Interfaces **2**, 2560 (2010).
[7]C. A. Crouse, C. J. Pierce, and J. E. Spowart, Combust. Flame **159**, 3199 (2012).
[8]C. E. Bunker, M. J. Smith, K. A. S. Fernando, B. A. Harruff, W. K. Lewis, J. R. Gord, E. A. Guliants, and D. K. Phelps, ACS Appl. Mater. Interfaces **2**, 11 (2010).
[9]W. K. Lewis, B. A. Harruff, J. R. Gord, A. T. Rosenberger, T. M. Sexton, E. A. Guliants, and C. E. Bunker, J. Phys. Chem. C **115**, 70 (2011).
[10]W. K. Lewis and C. G. Rumchik, J. Appl. Phys. **105**, 056104 (2009).
[11]W. K. Lewis, C. G. Rumchik, P. B. Broughton, and C. M. Lindsay, J. Appl. Phys. **111**, 014903 (2012).
[12]J. A. Orson, W. F. Bagby, and G. P. Perram, Infrared Phys. Technol. **44**, 101 (2003).
[13]J. R. Carney, J. S. Miller, J. C. Gump, and G. I. Pangilinan, Rev. Sci. Instrum. **77**, 063103 (2006).
[14]J. Wilkinson, J. M. Lightstone, C. J. Boswell, and J. R. Carney, in *Shock Compression of Condensed Matter*, edited by M. Elert, M. D. Furnish, R. Chau, N. Homes, and J. Nguyen (American Institute of Physics, 2007), p. 1271.
[15]K. C. Gross, J. Wayman, and G. P. Perram, Proc. SPIE **6566**, 656613 (2007).
[16]J. D. Koch, S. Piecuch, J. M. Lightstone, J. R. Carney, and J. Hooper, J. Appl. Phys. **108**, 036101 (2010).
[17]V. Bouyer, G. Baudin, C. Le Gallic, and P. Hervé, in *Shock Compression of Condensed Matter*, edited by M. D. Furnish, N. N. Thadhani, and Y. Horie (American Institute of Physics, 2001), p. 1223.
[18]V. Bouyer, I. Darbord, P. Hervé, G. Baudin, C. Le Gallic, F. Clément, and G. Chavent, Combust. Flame **144**, 139 (2006).
[19]K. B. S. Eriksson and H. B. S. Isberg, Ark. Fys. **23**, 527 (1963).
[20]C. Mendoza, W. Eissner, M. Le Dourneuf, and C. J. Zeippen, J. Phys. B **28**, 3485 (1995).
[21]R. W. B. Pearse and A. G. Gaydon, *The Identification of Molecular Spectra* (Chapman & Hall, 1963).
[22]J. J. Curry, J. Phys. Chem. Ref. Data **33**, 725 (2004).
[23]J. L. Gole and R. N. Zare, J. Chem. Phys. **57**, 5331–5335 (1972).

[24]S. Rosenwaks, R. E. Steele, and H. P. Broida, J. Chem. Phys. **63**, 1963–1965 (1975).
[25]S. Goroshin, J. Mamen, A. Higgins, T. Bazyn, N. Glumac, and H. Krier, Proc. Combust. Inst. **31**, 2011–2019 (2007).
[26]M. Jackson, M. Pantoya, and W. Gill, Combust. Flame **153**, 58–70 (2008).
[27]P. E. Bocanegra, D. Davidenko, V. Sarou-Kanian, C. Chauveau, and I. Gökalp, Exp. Therm. Fluid Sci. **34**, 299–307 (2010).
[28]I. Reif, V. A. Fassel, and R. N. Kniseley, Spectrochim. Acta, Part B **29**, 79 (1974).
[29]C. D. Yarrington, S. F. Son, and T. J. Foley, J. Propul. Power **26**, 734 (2010).